DETECTION OF LOW-VELOCITY IMPACT DAMAGE IN CARBON FIBER SANDWICH PANELS USING INFRARED THERMOGRAPHY

DETECTION DE DOMMAGE DU A I'MPACTE A BASSE VITESSE DANS DES PANNEAUX SANDWICHES FIBRES DE CARBONE UTILISANT LA THERMOGRAPHIE INFRAROUGE

A Thesis Submitted to the Division of Graduate Studies

of the Royal Military College of Canada

By

Tanner Rellinger, BSc, The University of Western Ontario

In Partial Fulfillment of the Requirements for the Degree of

Master of Applied Science in Aeronautical Engineering.

January 2019

ACKNOWLEDGEMENTS

I would like to thank my supervisors Dr. Diane Wowk, Dr. Catharine Marsden and Dr. Thomas Krause for their guidance at the Royal Military College of Canada. I would also like to thank Brendan Freeman, Charles Sadiq and Cory Sharpe for their help in manufacturing the many components needed for my test apparatus.

Finally, I would like to thank my parents, who have always pushed me to be creative, imaginative, and curious about everything surrounding me in the universe. Without your unfailing support and continuous encouragement throughout my many years of studying, this journey would not have been possible.

ABSTRACT

An aircraft is subjected to a variety of different types of damage while in flight or undergoing maintenance on the ground, the need to quickly and efficiently detect the induced damage is necessary before it can evolve into a safety concern. Most modern day aircraft take advantage of composite materials to reduce the overall mass of a component, while adding strength and durability. Due to the nature of composite face sheet honeycomb panels, accidental impacts from tool drops, runway debris, hail and bird strikes can cause internal damage to the honeycomb core, while leaving no evidence of an impact on the surface.

Innovative inspection methods are required to investigate damage and provide general checkups of these newer composite materials and structures. Infrared thermography has emerged as a promising non-destructive inspection method in many industries due to its relatively fast and inexpensive ability to detect subsurface anomalies and damage.

This research looks at composite face sheet honeycomb panels and infrared thermography's capabilities in detecting low velocity impact damage such as delaminations, disbonds, core crushing, water ingress and microcracking of the face sheet. Composite face sheet honeycomb test panels were manufactured using pre-impregnated carbon fiber plies with an aluminum honeycomb core material. Using a drop-weight impact tower, the test panels were subjected to a range of impact energies to simulate different types of damage due to low velocity impact. The impact locations were non-destructively inspected using 3D laser scanning, Eddy current testing and infrared thermography, and then destructively sectioned and observed using microscopy.

Seven studies were conducted that focused on testing active infrared thermography's capabilities in detecting different types of induced damage such as core crush, disbonds, ply delaminations and core separation. Passive infrared thermography was also investigated for its ability to detect water ingress within individual honeycomb cells.

It was shown that IR thermography is capable of detecting small voids that exist within the face sheet or honeycomb core. These can range from a delamination occurring in-between plies, to a slice occurring in the honeycomb cell wall. It also performed exceptionally well at detecting trapped water or ice within the honeycomb cells using passive IR thermography.

RESUME

Un aéronef subit divers types de dommages en vol ou en cours de maintenance au sol. Il est donc nécessaire de détecter rapidement et efficacement les dommages induits avant que ceux-ci ne deviennent un problème de sécurité. La plupart des aéronefs modernes tirent parti des matériaux composites pour réduire la masse totale d'un composant, tout en lui apportant la résistance et la durabilité. En raison de la nature des matériaux composites sandwiches à nid d'abeilles, les impacts accidentels dus aux chutes d'outils, aux débris de piste, à la grêle et aux impacts d'oiseaux peuvent endommager l'âme du panneau à nid d'abeilles tout en ne laissant aucune trace d'impact en surface.

Des méthodes d'inspection novatrices sont nécessaires pour étudier les dommages et effectuer des contrôles généraux de ces nouveaux matériaux et structures composites. La thermographie infrarouge est apparue comme une méthode d'inspection non destructive prometteuse dans de nombreux secteurs en raison de sa capacité relativement rapide et peu coûteuse à détecter les anomalies et les dommages sous la surface.

Cette recherche examine les panneaux composites à nid d'abeilles et les capacités de thermographie infrarouge pour détecter les dommages par impact à basse vitesse tels que les délaminages, les décollements (décohésion), l'écrasement de l'âme, les infiltrations d'eau et la microfissuration des peaux. Des panneaux composites à nid d'abeilles de test ont été fabriqués à l'aide des peaux en couches de fibres de carbone pré-imprégnées avec l'âme en nid d'abeilles dont le matériau de base l'aluminium. À l'aide d'une tour de chute libre d'impact à faible poids, les panneaux d'essai ont été soumis à une gamme d'énergies d'impact afin de simuler différents types de dommages d'impact à basse vitesse. Les emplacements d'impact ont été inspectés de manière non destructive à l'aide d'un balayage laser 3D, de tests par courants de Foucault et de thermographie infrarouge, puis ont été sectionnés et observés de manière destructive à l'aide d'une microscopie.

Sept études ont été menées sur les capacités de la thermographie infrarouge active à détecter différents types de dommages induits, tels que l'écrasement de l'âme, le décollement, le délaminage des plis et la séparation de l'âme. La thermographie infrarouge passive a également été étudiée pour sa capacité à détecter la pénétration d'eau dans des cellules individuelles du nid d'abeilles.

Il a été démontré que la thermographie infrarouge est capable de détecter les petits défauts existant dans la peau ou l’âme à nid d'abeilles. Ceux-ci peuvent aller d'un délaminage se produisant entre les couches à une coupure se produisant dans la paroi de la cellule du nid d'abeille. La thermographie infrarouge passive a également permis de détecter exceptionnellement l'eau ou la glace piégée dans les cellules du nid d'abeilles.

CONTENTS

LIST OF TABLES

LIST OF FIGURES

LIST OF ACRONYMS

BVID	Barely Visible Impact Damage
CCD	Charge-coupled device
CFRP	Carbon Fiber Reinforced Plastic
FEA	Finite Element Analysis
FPA	Focal Plane Array
NDE	Non-Destructive Evaluation
NDI	Non-Destructive Inspection
NDT	Non-Destructive Testing
QETE	Quality Engineering Test Establishment
TSR	Thermographic Signal reconstruction
TTU	Through transmission ultrasonic scanning

1 INTRODUCTION

Aircraft are traditionally built using different combinations of metal components to construct an overall section of the aircraft. Two of the main problems with metal components are their relatively heavy mass and susceptibility to fatigue over their lifetime. Metallic face sheet sandwich panels have gradually replaced traditional solid outer skins, as a honeycomb core combined with a face sheet offers increased bending stiffness and reduces the overall mass when compared to a thicker solid outer skin. As composite materials become more and more prevalent in the aerospace industry, composite face sheet sandwich panels have replaced metallic face sheet panels, which further reduce the mass of a component, but bring forth new problems that have become evident. Composite face sheets are prone to impact damage, which may not be visible after the damage has been induced and new methods are needed to inspect composite components for this hidden damage. Composite aircraft parts are usually made up of many sub-components, which are then combined together to achieve the required strength and flexural properties; these are usually bonded together using high strength adhesives. After combining separate components to construct an overall part, they can be quite challenging to inspect, versus a more traditional aluminum component assembled with rivets or bolts, which can be removed for inspections and repairs. As carbon fiber reinforced plastic (CFRP) structural components are composed of many individual fibers contained within plies and layered together, problems can arise in-between these individual layers that will remain invisible to an outside visual inspection. Micro cracks, delamination's in-between individual plies, as well as small air bubbles are all new problems that arise from using composite materials versus metallic materials.

Non-destructive testing and evaluation (NDT/E) has become an increasingly common process in the aerospace industry for detecting damage that is not initially visible to the human eye. There are many sophisticated NDE techniques that may be used to make inspection faster and more efficient than simply visually inspecting components and unnecessarily replacing components based on a set service life period.

There are many different types of non-destructive inspection (NDI) techniques used to analyze different sizes and kinds of components. These range from ultrasonic testing, eddy current testing and magnetic particle testing in engine compressor blades [1] to tap testing, shearography and thermography used for composite face sheet honeycomb panels used in most modern aircraft control surfaces [2]. Depending on the nature and structural makeup of

the target component, one might use through-transmission ultrasonic testing, which requires two-sided access to a component versus using infrared thermography, which only requires one-sided access.

Most outer surfaces and control surfaces on modern composite aircraft are made from honeycomb panels with a composite face sheet and are prone to damage from airborne debris or damage caused by human error. Impacts from a low velocity object might visually appear to have not caused any damage, but studies have shown that even an object such as a screw driver dropped from waist height can result in enough internal damage to change the strength of a component [3]. If the face sheet becomes disbonded from the honeycomb core, the disbonded location has a severely reduced bending stiffness, which can lead to shearing or buckling of the honeycomb core [3]. Detecting this type of damage before it evolves into a potentially fatal problem is quite important and infrared thermography has emerged as a very promising technique to inspect components that are fresh off of the production line, currently in operation, or removed from service.

This document will take a closer look at infrared thermography and its potential application for inspecting composite face sheet honeycomb panels. Flash thermography uses a burst of thermal energy applied to the surface of an object and monitor how the energy is able to dissipate through the body. As composite face sheets readily allow thermal energy to pass through, any delaminations in the face sheet or disbond occurring in-between the face sheet and honeycomb core become visible when the thermal energy is not able to pass through.

Chapter 2 will start with the basic structure of composite face sheet honeycomb panels and which types of damage they are prone to from low velocity impact events. The inspection methods used to detect these types of damage are briefly discussed, while the basics of infrared radiation (IR), how IR thermal cameras work and how to process the acquired data from an infrared thermography scan are looked at in greater detail.

Chapter 3 goes over the manufacturing techniques used to make composite face sheet honeycomb panels and how to introduce different types of damage.

The results Section in Chapter 4 includes a number of sub-studies experimentally testing IR thermography’s capabilities in identifying different types of damage.

2 LITERATURE REVIEW

Nondestructive testing and evaluation (NDT/E) exists in many different fields and industries. It is a critical step for inspecting, testing and certifying new or operational components without changing the characteristics, chemical makeup or altering the component in anyway.

Air and spacecraft are assembled using hundreds of thousands and sometimes even millions of different components. When NASA build the Saturn V rocket, it was assembled with over 3 million separate parts [4] and produced over 7.6 million pounds of thrust at takeoff; this could power the entire city of New York for over 75 minutes [5]. The complexity and assembly processes that went into making such a technologically advanced and successful operating spacecraft were thought to be years ahead of its time. Application of nondestructive testing was a critical stage in the building process to ensure each component could operate at its maximum capacity without failure. Methods included radiographic inspection, which was used to inspect welds and castings, liquid penetrant inspection for detection of leaks, and the most widely used method of Ultrasonic testing to detect flaws in metallic plates, rods and tubes [6].

Over the years since the building of the famous Saturn V rocket, new materials, building methods and technology have exponentially progressed, which has allowed for even more complex and sophisticated air and spacecraft. A modern day Boeing 747-8 aircraft contains over double the number of parts that were in a Saturn V rocket, and is assembled out of over 6 million different parts with an incredible 250 kilometers of wiring in each aircraft [7]. An aircraft containing that many components requires regular inspections and tests to ensure it stays flight ready and does not suffer any catastrophic failures throughout its lifetime. Inspecting this many components using only visual and hands-on methods would be impossible and therefore requires the use of modern day nondestructive testing and evaluation technologies.

2.1 Composite Honeycomb Panels

Honeycomb sandwich panels usually consist of: a light weight core material, which is sandwiched between two stiff face sheets and adhered using a film adhesive. The core material can be made out of many different materials including foam, fiberglass, Nomex as well as aluminum honeycomb. This thesis will focus on composite face sheet sandwich panels with an aluminum honeycomb core.

2.1.1 Core Material

Aluminum honeycomb is a commonly used core material, which is manufactured using long thin strips of aluminum creased into a half hexagon shape. The strips are then merged together using resistance or laser welding to form hexagonal cells. Due to the manufacturing process, each cell will have two walls that are double the thickness of the remaining four walls. The direction that the double wall runs is called the ribbon direction, while the perpendicular direction is the transverse direction as shown in Figure 1.

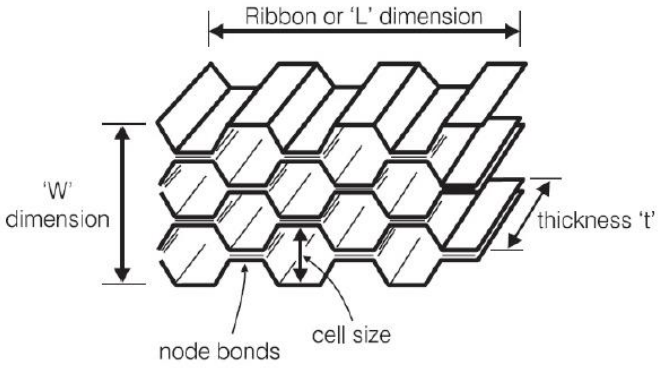

Figure 1: Honeycomb core material showing the ribbon and transverse directions as well as the cell size, bonding locations and thickness [8].

2.1.2 Face Sheet Material

The aluminum honeycomb core material is sandwiched between two composite face sheets, which can be made from unidirectional carbon fiber plies, meaning there are millions of fibers running parallel to each other as opposed to the widely seen woven cloth version, which contains fibers running parallel and perpendicular to one another. Using unidirectional carbon fiber has many benefits over woven cloth, one being that the layers are actually slightly tighter together due to the fibers being straight as opposed to a wave shape caused by weaving the fibers together; this minimizes the voids contained in-between fibers in which excess resin can pool, causing increased weight with no added strength properties. When manufacturing composite components for aircraft, the direction in which the panel will experience loading is already known, this allows strategic orienting of the fiber direction to absorb and resist the applied forces without adding additional and unnecessary plies. Both types of carbon fiber cloth are shown below in Figure 2.

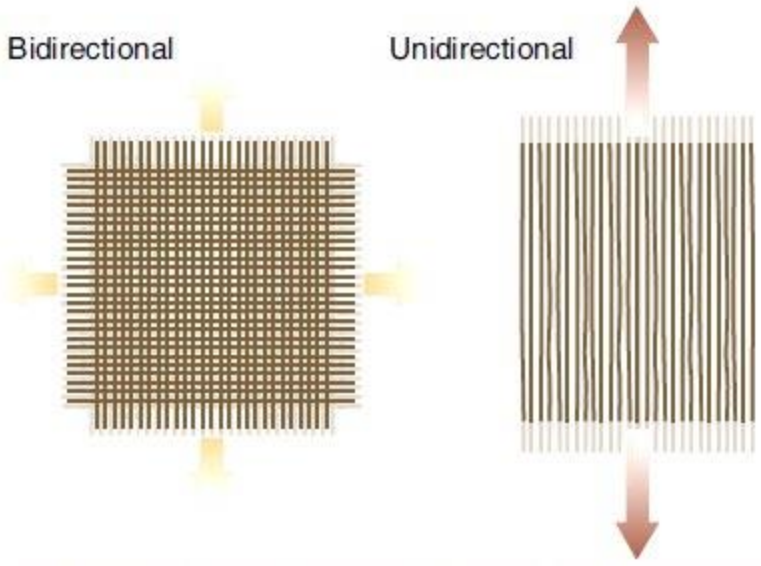

Figure 2: Properties of unidirectional and bidirectional (woven) carbon fiber cloth [8].

The fibers in unidirectional plies all run in the same direction and only offer strength and stiffness in this direction, to manufacture a face sheet with strength properties in many directions, various layers of unidirectional plies are stacked together to achieve a quasi-isotropic material [9]. The most common angles for a unidirectional fiber layup are shown in Figure 3 and consist of 0, 90 and 45 degree orientations.

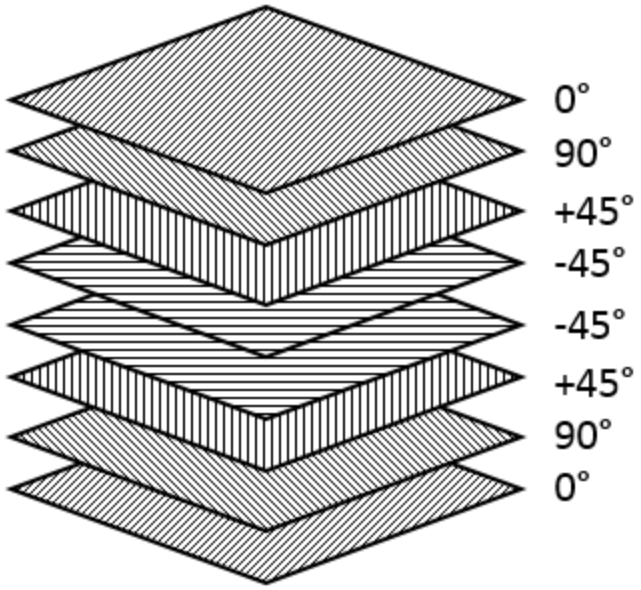

Figure 3: Common carbon fiber ply orientations used in composite aerospace components.

Composite face sheets are usually manufactured symmetrically, meaning that the ply orientations in the top half of the face sheet are mirrored about the mid plane of the layup; this is to balance the internal stresses produced when curing the pre-impregnated (prepreg) resin.

2.1.3 Complete Panel

Once the face sheets have been manufactured, they are adhered to the honeycomb core using an uncured film adhesive. This comes as a thin roll of adhesive, which is supported by a release paper. This is a temperature cured adhesive and needs to be stored in a freezer until it is ready for curing. The face sheets need to be adhered to the honeycomb core with an applied pressure specific to the film adhesive, if too much pressure is applied, the honeycomb cells may become damaged, while too little pressure may result in small adhesive fillets within the honeycomb cells; this is discussed in further detail in Section 3.1.

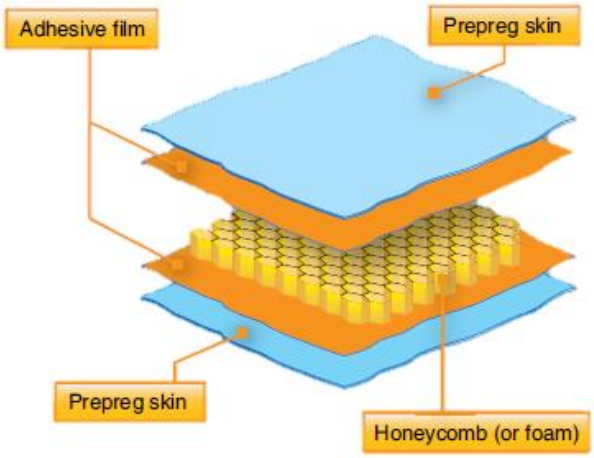

Figure 4: Typical layup sequence of a composite honeycomb sandwich panel [8].

When a honeycomb panel is assembled as shown in Figure 4, the honeycomb panel has a very high bending stiffness-to-weight ratio and increasing the core thickness further increases the overall stiffness of the panel. For example, if two solid face sheets are placed on top of each other, having an overall thickness of 1.0 (0.5 each), combined they will have a flexural strength of 1.0 with a mass of 1.0. If a honeycomb core is added in-between these two face sheets with a core thickness of 1.0, the overall thickness of the panel increases to 2.0, while the flexural strength increases by 250% with a mass increase of only 3%. If a core thickness of 3.0 is used instead, the flexural strength increases by 820% with an overall mass increase of only 6% [8]. This demonstrates that adding honeycomb core in-between two face sheets provides a large stiffness increase with a very minimal increase in weight.

2.2 Low Velocity Impacts

Impacts occurring to aluminum face sheet honeycomb panels tend to be more detectible with a simple visual inspection than those occurring to composite skin honeycomb panels. *Wowk* and *Marsden* [10] found that due to the ductile nature of aluminum face sheets, after an impact occurs, the face sheet does not tend to elastically spring back more than 50%, leaving barely visible impact damage (BVID). If an impact occurs to a composite face sheet however, the contained fibers and epoxy, which make up the individual plies of carbon fiber, tend to flex or break together. It was found that the stresses contained in the unbroken fibers can pull the face sheet back to its original position, leaving no trace of an impact event with a visual inspection. *Minakuchi, Uezono, Siivola* and *Takeda* [11] have studied composite face sheet relaxation and concluded that the period of relaxation is highly dependent on the stress relaxation of the core material when the face sheet remains adhered. Boeing [12] defines a typical BVID between 0.254-0.508 mm accounting for face sheet relaxation; this makes it difficult to detect BVID impacts with a visual inspection. There is a major difference when it comes to classifying different types of impacts and the resulting damage modes that arise due to the velocity of the impact. Impacts are usually broken up into two separate categories, low velocity and high velocity [3]. High velocity impacts are dominated by stress wave propagation through the material, this is where the face sheet does not have enough time to respond to the impact, which in most cases causes obvious and very localized damage. In a low velocity impact, the contact duration of the impactor is long enough that the face sheet and honeycomb core have enough time to respond and more energy is absorbed by the rest of the face sheet and core material as opposed to a very localized area. The velocity difference between these two types of impacts is unclear. *Adbrate* [3] defines a high velocity impact as one that occurs over 100 m/s, while others like *Cantwell* and *Morton* [3] define this limit as over 10 m/s. Others like *Lui*, *Malvern*, *Joshi* and *Sun* [3] define this limit based on what type of damage results from the impact, stating that a high velocity impact is one where penetration of the face sheet occurs resulting in fibers breaking, while a low velocity impact only induces a disbond in-between the face sheet and core material, a delamination in-between individual plies, or matrix cracks running parallel to the fiber direction. As the detection of barely visible impact damage is of interest in this paper, impact velocities were kept below 5 m/s, while no penetration of the face sheet occurred throughout testing.

2.3 Composite Honeycomb Panel Defects

Composite honeycomb panels can undergo many different types of defects and damage. The main concerns with an aluminum face sheet panel are corrosion and tearing of the aluminum face sheet and aluminum honeycomb core. Denting of an aluminum honeycomb panel is usually quite obvious from a visual inspection once the aluminum face sheet is depressed. It is not very likely in this case that the face sheet will elastically spring-back to its original undamaged position. The face sheet may relax close to its original position but according to *Wowk* and *Marsden* [10], it will not return 100% of the way back.

In a composite panel however, there is a higher amount of residual stress in the face sheet that pulls it back to its original un-damaged position. This can make sub-surface damage virtually invisible, while causing major structural damage just below the face sheet's surface. As composite face sheets are manufactured from many individual layers of pre-impregnated carbon fiber plies stacked together, vacuum bagged and then cured, there is a higher chance for manufacturing defects to arise than a traditional aluminum face sheet honeycomb panel. Table 1 provides examples of manufacturing defects as well as in-service defects and damage occurring to composite face sheet honeycomb panels.

Manufacturing defect	In-Service Defects
Delaminations	Impact damage
Voids between fibers	Delaminations
Resin rich or starved locations	Disbonding
Porosity from air bubbles	Microcracking and fiber breaking
Pre-stressing fibers	Fatigue
	Core crushing or shearing
	Water ingress

Table 1: Manufacturing and in-service defects and damage occurring to composite face sheet honeycomb panels [8].

Defects and damage to the face sheet and honeycomb core can arise from faulty manufacturing methods or while the component is in-service. Each type mentioned in Table 1 is briefly discussed below. This thesis focuses on detecting in-service damage from low velocity impacts, but also provides examples in Section 4.5 on how to differentiate these from manufacturing errors. The type of damage is broken up into two categories: damage occurring to the face sheet and damage occurring to the honeycomb core. As the face sheet is made up of several layers of unidirectional prepreg carbon fiber plies, damage can arise on the outer surface, in-between individual plies, across multiple plies, or on the bottom face.

2.3.1 Face Sheet Defects

2.3.2 Residual Indentation

Residual indentations of the face sheet are the easiest to detect as they can usually be spotted with a simple visual inspection. These are caused by the face sheet suffering impact damage caused by tool drops, runway debris, air field equipment or hail. These leave the face sheet depressed, while remaining adhered to the core material as shown in Figure 5.

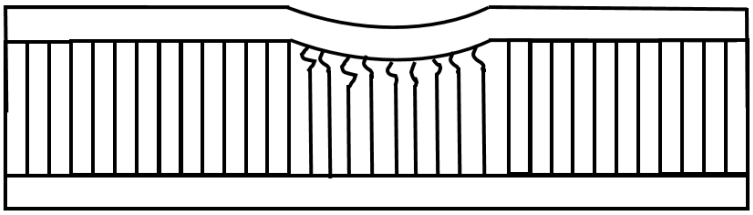

Figure 5: A residual indentation of the face sheet, leaving the face sheet, film adhesive and honeycomb core depressed.

2.3.3 Delamination

Delaminations in between individual layers of carbon fiber are a problem that cannot be observed by a simple visual inspection of the face sheet's surface. The force from an impact event to the surface is able to propagate further into the panel, through multiple layers and can cause delaminations in-between the individual plies of carbon fiber. A delamination may initiate from a microcrack or pore within the ply and does not always require an impact event to cause one. If a component with a delamination is put into compression, the delamination may grow in size from the two plies being forced apart from one another as shown in Figure 6. This can happen naturally during a components service life and may go unnoticed until the part has a catastrophic failure.

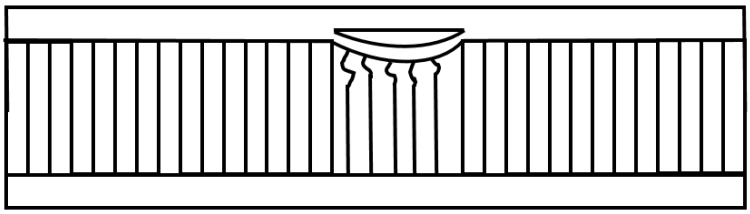

Figure 6: A delamination occurring in-between plies of carbon fiber caused by an impact event.

2.3.4 Matrix Cracking

As mentioned, cracking may occur in between the separate plies or across multiple plies. These cracks may run parallel to the fibers' direction, perpendicular to them or across multiple plies. Cracks running perpendicular to the fibers means that the fibers have actually broken; these are usually caused by fatigue to the fibers or extreme thermal fluctuations. Impact events are usually the cause of microcracking as the fibers undergo a large amount of stress in a very localized area, causing the fibers to break rather than flex. Cracks from an impact may initiate starting from the top ply and work their way down through the plies, which results in a pine tree shape. If the panel is flexed, the lower side of the face sheet is put under tension, which can lead to cracks forming from the bottom side of the face sheet and working their way up, forming a reverse pine tree shape as shown in Figure 7.

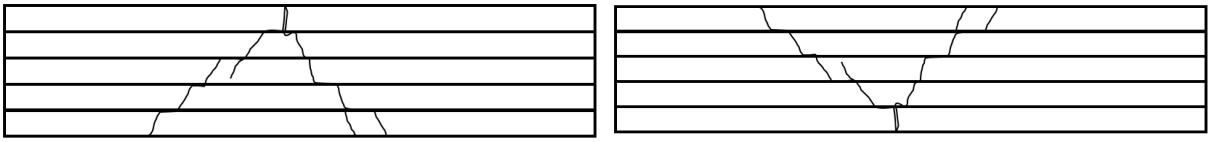

Figure 7: Matrix cracking in the face sheet propagating down from the surface. Pine tree (Left) and reverse pine tree (Right).

2.3.5 Porosity

Composite panels can experience porosity in-between fibers of the same ply or in-between individual plies. These can arise from having trapped air pockets or foreign material in between the laminate layers or from mishandling of the delicate unidirectional prepreg before the curing process. Trapped gasses in the film adhesive may bubble during the curing process causing cavernous locations; this can cause problems down the road as locations like these are more prone for interlaminate splitting or cracking to initiate from. Porosity may also arise from the material being mishandled during the layup. If sterile rubber gloves are not used, oil from skin can cause bonding issues in-between the plies, again leaving that location prone to delaminating once the panel undergoes compression. Examples of porosity are shown in Figure 8.

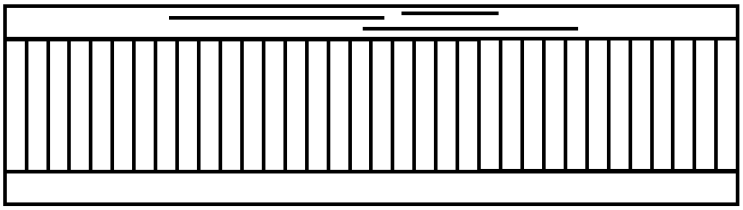

Figure 8: Porosity inbetween individual plies of carbon fiber from poor bonding pressure, trapped air, or contaminated resin.

2.3.6 Excess adhesive

Excess adhesive results from a manufacturing error when the face sheet or sandwich panels are made; this type of defect is not caused by an airborne debris impact or human caused impact damage. Having excess adhesive in the face sheet can cause a localized area to have different strength properties than its surroundings; this is usually caused by the adhesive running, while the curing process is taking place. When using a vacuum bagging technique to cure face sheets, adhesive can be squeezed out of one area and deposited in another. This not only results in excess adhesive in one area, but also removes adhesive from another, leaving the adhesive deprived area with lower strength properties and the potential to fail prematurely. Excess adhesive may also occur due to the film adhesive running during its curing process. This again can leave areas with too much or too little adhesive to form a proper bond to the face sheet, causing deviations in the localized stiffness, which compromises the strength of the entire structure. An area with excess adhesive can be seen in Figure 9, where it has pooled just under the face sheet.

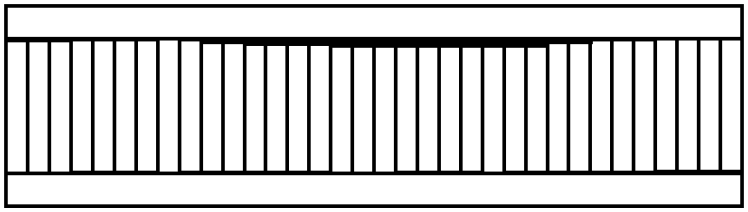

Figure 9: Excess adhesive inbetween the face sheet and honeycomb core.

2.3.7 Core Defects

2.3.8 Disbond

The carbon fiber face sheets are bonded to the core material using a thin film adhesive. If the bond is broken between them, a disbond may occur between the film adhesive and the face sheet or between the honeycomb core and film adhesive. These are caused by an impact event to the face sheet and can go unnoticed if the face sheet relaxes back to its original position as shown in Figure 10.

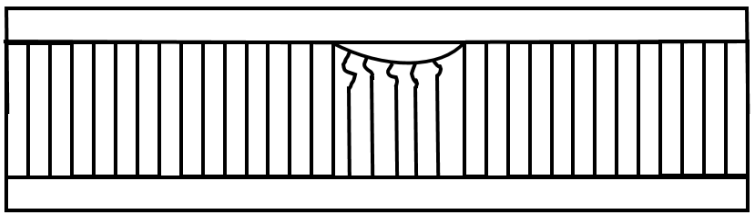

Figure 10: Disbond occuring between the face sheet and film adhesive.

2.3.9 Core Cracking, Tearing or Shearing

Cracking or tearing of the honeycomb core may initiate from an impact event crushing the honeycomb cell walls. When the thin cell walls are compressed down they form a Z shape and can tear at the sharp corners formed. If the panel is put into tension, these small tears can grow leading to cracking and reduced strength in the core. Figure 11 shows the tearing and cracking of the honeycomb core cell walls.

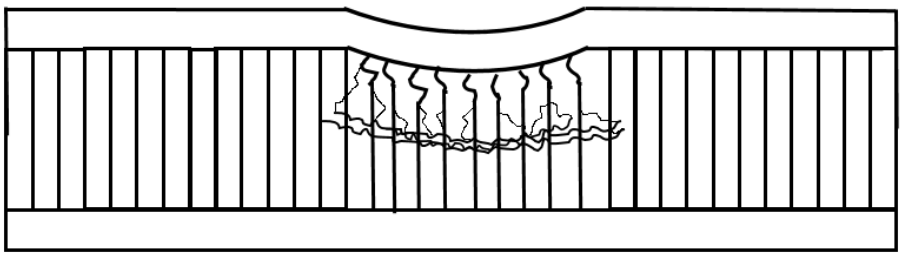

Figure 11: Tearing and cracking of the honeycomb core cell walls.

2.3.10 Water Ingress

During the panel's service life, the aircraft will experience many different forces, temperatures and pressures. If the face sheet becomes disbonded from the honeycomb core, moisture and water is able to seep into honeycomb cells and become trapped. The water is thought to enter the structure along the leading edge, through grounding strap attachment points or hinge locations. If the water remains in the cells, it can cause corrosion and deterioration of the face sheet, honeycomb core or fasteners. If the water freezes and expands, it could lead to a larger disbond and potentially fatal reduction in the panel's strength. The film adhesive can also be affected by the increase in moisture content. The FM300 epoxy tends to absorb up to 10% moisture by weight [14], which can lead to degradation of the adhesive's strength and an increase in volume, leading to buckling and disbonding. *Edwards* [14] performed a comprehensive examination of water ingress occurring in F/A-18 rudders, and compares a variety of NDT methods such as ultrasonic testing, neutron radiography and IR thermography and their ability to detect subsurface water or ice. Figure 12 shows an example of water ingress in a honeycomb sandwich panel.

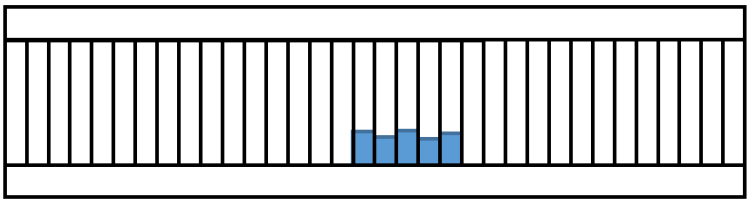

Figure 12: Water ingress present in multiple honeycomb cells.

2.4 Inspection Methods

Many methods currently exist for inspecting composite aircraft components, but as new technologies are introduced and the cost of inspection equipment drops, older technologies like tap testing and the use of calipers and dial gauges are being phased out. A visual inspection of an aircraft's outer surface is usually the first step followed by a more comprehensive scan to determine the amount of internal damage. Eddy current and ultrasonic testing have been reliable NDT methods for honeycomb sandwich panels but require certified inspectors with advanced training and covers a relatively small area of the aircraft with each scan. 3D Laser scanning covers a larger surface area but only provide surface deformation information about the face sheet and no information about the damage below the face sheet. IR thermography is able to look at a large surface area with relatively inexpensive inspection equipment, while also requiring less training than eddy current or ultrasonic testing. IR thermography works as a first stage inspection and is able to detect damage to the face sheet as well as the underlying honeycomb core as will be demonstrated in this thesis.

2.4.1 Visual Inspection

Visually inspecting an aircraft is usually the fastest and most inexpensive method when looking for damage. Before an aircraft is allowed to take off, a walk around the craft is performed and vital components listed on a pre-flight check list are visually inspected. Obvious damage and defective areas can be quickly found and flagged for further inspection using a more advanced inspection method. Flash lights may be used on external body panels to quickly locate dented or bulging areas based on how the light is reflected from the edge-of-light method [15]. Canadian Helicopter operators use an LED flashlight, which is held at an angle almost parallel to the surface being examined; if a dent is present, the light rays converge towards the principle axis of the flashlight. If a bulge is present, the light rays diverge away from the principle axis of the flashlight [15].

2.4.2 Hand Measuring devices

Hand measuring devices such as calipers and micrometers may be utilized to quickly compare a component to its original size and shape. These can provide a rough estimate of depth and area of the damage present on the surface of a panel, but do not provide any information about damage occurring underneath it. Damage occurring to the core material or any delaminations or disbonding occurring within the face sheet will go unnoticed.

2.4.3 Tap testing

If a visual inspection reveals that an external body panel contains a dent or bulged area, the next fastest and simplest method of testing may be implemented. Tap testing requires repeatedly tapping the component around the area of interest and listening for a change in the emitted sound. This is the same technique used when attempting to locate a stud on the other side of drywall, tapping the area in-between studs will sound like an empty void exists there, but when tapping on the drywall in front of a stud, the frequency will rise and you could assume that there is a solid structure behind this section of wall. When applying this method to aircraft panels, small tap hammers are utilized, which have a solenoid located in the head of the hammer. This solenoid is able to determine the duration in which the head of the hammer is in contact with the surface. The contact duration is related to how stiff the surface is in that location and the underlying structural support can be assumed. *Prior* [13] has successfully implemented using a tap hammer on composite face sheet honeycomb panels for locating disbonds or structural repairs, but this method is not a very accurate technique for locating small damage like microcracking within the face sheet as it has a low resolution and only gives an approximate area where the defect is located. This offers an inexpensive and quick method of confirming a visual inspection, but higher resolution NDT methods should be used in conjunction with tap testing to confirm and pinpoint the damage.

2.4.4 Ultrasonic Testing

A common NDT method used by manufactures is ultrasonic testing. Through-transmission ultrasonic scanning (TTU) uses two transducers, one is the transmitter, while the second is the receiving transducer located on the opposite side of the component. A beam is emitted from the transmitting transducer into the component, it travels through the part and is picked up by a receiving transducer on the other side. A coupling material such as water is used to transmit the beam to the surface of the component. The time it takes for the signal to pass through the component being inspected as well as how the received wave is distorted is then reassembled to reveal the internal structure [16]. Another type of ultrasonic testing is the pulse echo method, which has the transmitting and receiving transducers on the same side of the component. As a beam is emitted from the transmitting transducer and into the component, any discontinuity or defect within the component will disrupt the emitted wave and echo back to the receiving transducer [17]. Again the signal is reassembled to reveal the internal structure of the component [17]. The pulse echo technique is widely used when components are in-service, as having a receiving transducer on the opposite side of a component is not always practical. This method of ultrasonic testing has successfully located delaminations in-between plies of carbon fiber as well as disbonds in-between the face sheet and film adhesive as repeated by *Thwaites* and *Clark* [18].

2.4.5 3D Laser Scanning

Scanning and importing real-life dimensions and shapes into computer based programs for analysis and testing is a rapidly growing technique in many industries. Three dimensional scanners can be broken up into two separate categories, when it comes to collecting the spatial information of an object. The first type of scanner utilizes a touch probe, which physically needs to touch the object at multiple locations to collect a cloud of spatial points. As the probe touches different locations, the scanner collects spatial information based on its position and plots a series of points to make a final 3D cloud of points. The downside to this method is leaving gaps in-between the locations where the probe has touched and relies on software to estimate the surface geometry in-between the probed locations. A more accurate and thorough method is to use a light source emitted from the probe such as a laser beam, which is then bounced off of the object and received by a sensor also located on the probe head.

Non-contact scanners may use different technologies to rebuild the surface geometry of the scanned object, one of which is called time-of-flight, which calculates how long it takes the laser beam to be reflected off of the surface and received again. From this information the distance from the probe head and geometry of the surface may be determined. Another method is triangulation, which uses a camera to determine the location of the emitted laser dot on the surface. Depending on where the laser dot is located in the camera's field of view, the sides of the triangle formed by the emitter, laser dot and camera may be calculated, leading to the distance and shape of the scanned surface.

Depending on the size of the object being scanned, the laser scanner may take millions of data points which are then projected into a 3D space and a surface may be fit to the cloud of points. The more data points that are taken, the more precise and accurate the fitted surface will be. The final surfaced point cloud may then be exported into many common 3D file types and used in modeling programs such as SolidWorks and finite element analysis (FEA) programs like ANSYS or ABAQUS. Laser based 3D scanning has successfully been able to measure the amount of residual indentation to aluminum face sheet honeycomb panels, which proved to be within 0.04 mm from measurements taken with a depth dial gauge [19]. Creaform is a leader in 3D measuring devices and has recently branched out into providing NDT methods specifically for measuring dents present on an aircraft's outer skin. This uses a handheld 3D laser scanner and provides an automated surface deviation analysis of the ripples and dents arising on the outer surface. Air France Industries and KLM Engineering and Maintenance have successfully been implementing Creaform's 3D scanner for detecting hail damage to their aircraft, which has reduced their inspection time by over 80% [20].

2.4.6 Infrared Thermography

Infrared thermography (IRT or IR Thermography) has emerged as a quick and accurate technique for inspecting and testing composite aerospace components. There are many different methods for using IR thermography for detection of flaws or defects within honeycomb panels. Passive IR thermography relies on the component undergoing temperature changes that naturally occur, while the component is in its operational phase. For example, while monitoring a rotary engine, an unusually hot spot may be due to a high amount of friction in that area, leading to the assumption that there might be a lack of oil being supplied there, requiring

further investigation. An aircraft will undergo a dramatic temperature change as it descends from a higher, colder altitude to a lower, warmer elevation, if water has become trapped in the individual cells of a honeycomb core panel, the water/ice will warm up at a different rate than the surrounding aluminum honeycomb core or carbon fiber face sheet. A thermal camera is able to pick up the small temperature difference between the water/ice and the surrounding area and display it as an abnormally cold area. The Canadian Forces have successfully used passive IR thermography as a method to detect water ingress in the tail rudder of an F/A-18 aircraft. *Edwards*, *Savage*, *Hungler* and *Krause* [21] compared neutron radiography, ultrasonic scanning as well as thermography for detection of water within the honeycomb cells contained in an F/A-18 vertical stabilizer rudder. Thermography was able to quickly and cheaply locate the trapped water compared to a lengthy and expensive neutron radiography scan. *Edwards* [14] also compared passive thermography results to those acquired with ultrasonic testing and noted that thermography does not provide the greatest resolution, but offers the quickest and most inexpensive inspection.

Active thermography is becoming a more common technique and has also been successfully used on composite aircraft components for detecting different kinds of defects and damage [22]. *Foreman* [22] has used active thermography to successfully locate disbonds and delaminations within composite face sheet honeycomb panels.

Active thermography relies on thermally exciting the component instead of using atmospheric influences to create a temperature gradient within the component. There are many different techniques used to induce a thermal gradient, ranging from lasers, light bulbs, eddy currents or ultrasound. Each method of thermally exciting the component has its pros and cons, and depending on what type of defect is of interest. For example, Halogen bulbs may be used for detecting a disbond versus ultrasound for detecting cracks. Pulsed IR thermography relies on using Xenon or Halogen bulbs to send a short thermal wave into the component, while monitoring the surface to see how the wave propagates through the sample. While other methods of heating may require a large testing setup, extensive training or are expensive to implement, pulsed IR thermography is chosen for its ability to detect a wide range of defects, ease of use and overall more economical testing cost.

2.4.6.1 Infrared Radiation

Infrared radiation is classified as having a wavelength between ~780 nanometers and ~1 mm, which includes terahertz radiation having a wavelength between 0.1 mm and 1.0 mm. Infrared radiation has a longer wavelength than visible light and the human eye is unfortunately not able to detect it, since it can only detect a small portion of the electromagnetic spectrum between 380 nm to 780 nm. Some animals like snakes have developed the ability to sense infrared radiation, which essentially allows them to see in the dark; this helps them greatly when hunting, as being able to see a prey's infrared radiation signature as well as their visible signature greatly increases its chance for a successful hunt. An overview of the electromagnetic spectrum is provided in Figure 13.

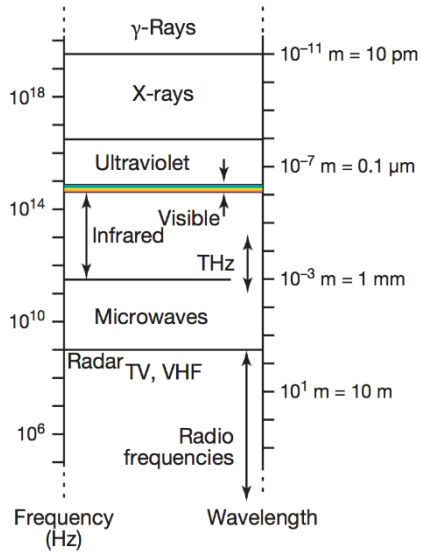

Figure 13: Overview of the Electromagnetic spectrum [23].

Both visible and infrared radiation are considered electromagnetic radiation. To have a better understanding of how electromagnetic radiation travels, it is easier to imagine the electromagnetic radiation taking on a waveform. The wavelengths described above are related to the wave's frequency and propagation speed as expressed in Equation 1 below. Where the speed of propagation c is directly related to the wave's frequency ν and the wavelength λ.

$$c = \nu \cdot \lambda \tag{1}$$

The speed at which a wave travels depends on the type of wave as well as the medium it is traveling through. Sound waves traveling through a medium like air or water will travel at a much slower velocity than an electromagnetic wave travelling through a vacuum or similar medium. An example of a sinusoidal wave propagating from left to right is shown below in Figure 14, with the red section representing its wavelength λ and T representing its period.

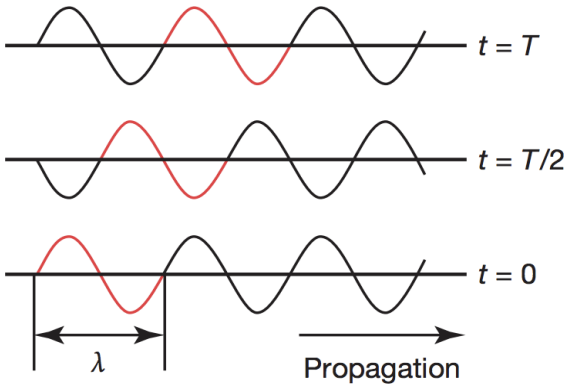

Figure 14: Propagation of a wave traveling from left to right in a sinusoidal wave shape [23].

There are two ways in which a wave travels or propagates, with the first being the transverse method and the second being the longitudinal method. In longitudinal waves, the disturbance is parallel to the propagation direction like a wave traveling in water. Electromagnetic waves are considered transverse waves and the disturbance is perpendicular to the propagation direction as shown in Figure 15 (b).

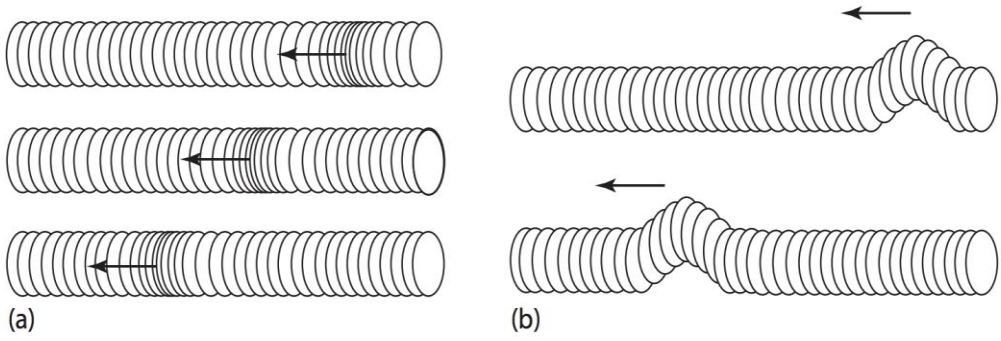

Figure 15: longitudinal (a) and transverse (b) wave travel [23].

Thermal infrared radiation between 0.75 and 14 μm is further broken down into three subsections. Short wave infrared radiation is closest to visible light and is classified as having a wavelength from 0.9 μm to 1.7 μm, mid-wave infrared radiation from 3.0 μm to 5.0 μm, while long-wave infrared radiation ranges from 8 μm to 14 μm as shown in Figure 16 [23].

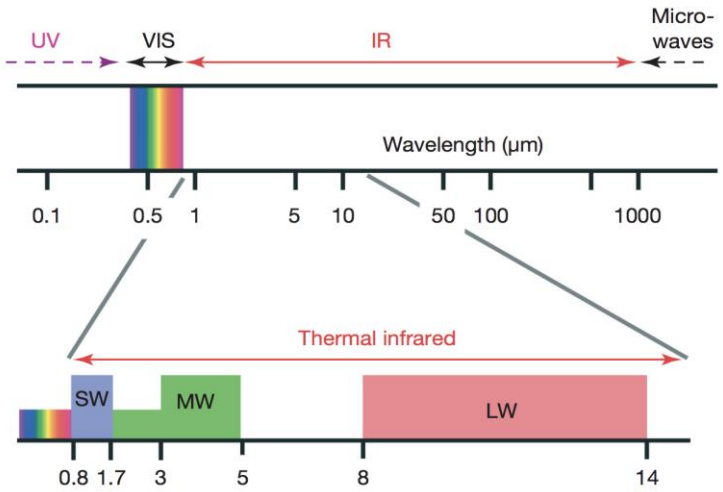

Figure 16: Infrared radiation divided into short, mid and long wave sections [23].

Transverse waves described by (b) in Figure 15 have two components, An electric field E as well as a magnetic field B and propagate perpendicular to one another as shown in Figure 17.

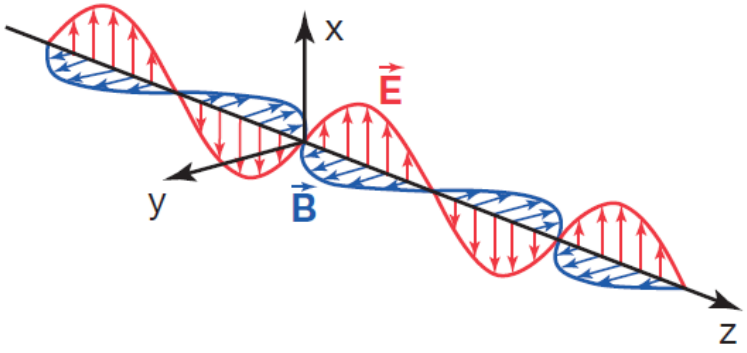

Figure 17: Electromagnetic waves containing an electric field (E) and magnetic field (B) [23].

Any object that has a temperature above 0 Kelvin or absolute zero emits IR radiation proportional to its temperature, which is shown below in Equation 2 by the Stefan-Boltzmann law.

$$Q_{Out} = e\sigma T^4 \tag{2}$$

Where Q is the amount of energy, e is the thermal effusivity and σ is the Stefan-Boltzmann constant.

Objects can emit and absorb electromagnetic radiation and the ratio between the amount of radiation emitted and absorbed is dependent on the object's material properties. The law of reflection shown in Figure 18 describes how light rays either reflect or refract when hitting an object's surface and is important to keep in mind when attempting to use IR thermography as a NDT tool.

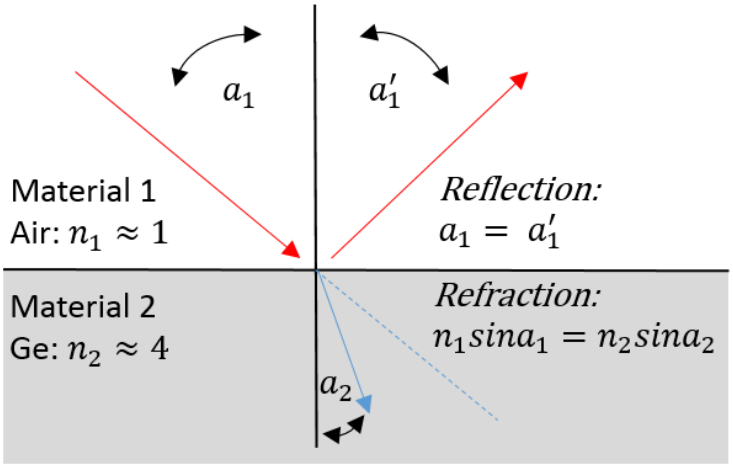

Figure 18: Law of reflection showing how radiation is absorbed and reflected from a surface.

The angle between the incident radiation and the normal of the surface is called the angle of incidence a_1, and is equal to the reflected angle given by a_1'. The radiation that gets absorbed by the body follows the angle of refraction and is dependent on air and each body's index of refraction given by n_1 and n_2, respectively. Snell's law given below by Equation 3 combines the reflected angle and refracted angle with both the body's index of refraction as well as the index of refraction where the radiation initiates from. In most IR thermography cases the medium would be air, which has an index of refraction of ≈ 1.

$$n_1 sin\alpha_1 = n_2 sin\alpha_2 \tag{3}$$

There are several factors that determine how radiation is reflected or absorbed by a body, including which material it is made out of, its surface finish as well as its emissivity. An object's

emissivity is the ratio of how much radiation is actually emitted by a body to that emitted by a perfect black body at the same temperature. A black body is a theoretical object, which absorbs all radiation that it is subject to, it is also able to emit 100% of the radiation contained within it. The closest thing to a real black body is a black hole, which absorbs all radiation that passes through its event horizon and emits radiation in the form of Hawking radiation. From this definition, no object on earth can perfectly absorb or emit radiation. Therefore, emissivity is used to describe how effective a surface is at emitting radiation. The emissivity given by ε can have a value between 0 and 1, with a poor emitter being close to 0 and a theoretically perfect emitter being a 1. The reflectiveness and surface roughness of an object dramatically change its emissivity value and some surfaces like glass and polished metals require sanding or coating with matt paint to achieve an accurate temperature measurement.

Figure 19 is an example of how infrared radiation is able to reflect off of an object even if the surface finish does not visually appear reflective.

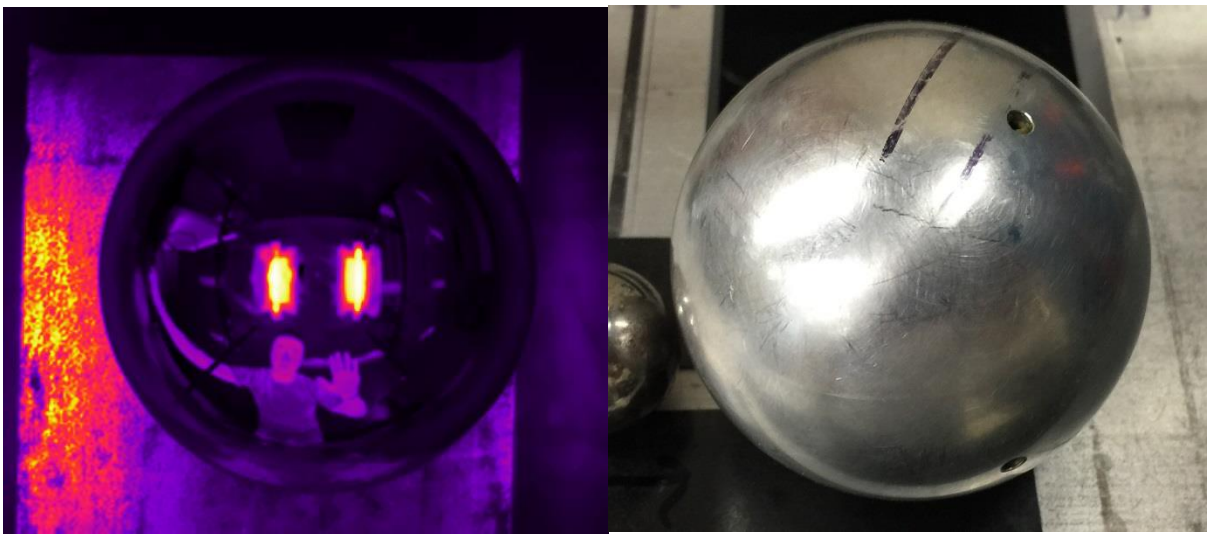

Figure 19: The steel ball is scratched and appears to have a matt finish, but the IR radiation from the surrounding environment is reflected off of the balls surface, resulting in an inaccurate temperature reading of the ball.

Most IR thermal cameras are able to correct for small emissivity values but require calibrating the camera with a material of a known emissivity. Black electrical tape has an emissivity of 0.96 and can be placed on an object, ensuring there is good thermal contact between the two surfaces. The camera then adjusts the emissivity of the object until the electrical tape and object have the same temperature reading.

2.4.6.2 Infrared Cameras

An infrared camera functions in a similar way to that of a regular visible light camera, but looks at a different section of the electromagnetic spectrum. An IR thermal camera contains a focal plane array (FPA) microbolometer in place of a CCD as in a visual light camera. The microbolometer sensor is a matrix of detector plates, which can be visualized as little tables all arranged beside one another to form the entire sensor chip. The “tables” are made out of electrically conductive vanadium oxide or amorphous silicon and each only stand on two legs. When radiation enters the front optics of the camera and makes its way to the sensor, the radiation strikes the table top and the electrical resistance of the “table” changes. The more radiation that strikes the table top, the more the electrical resistance of the table will change. The change in electrical resistance is then monitored by sending a current up through one of the table legs, across the table top and down the other leg. The acquired electrical signal is then converted to a temperature value or radiance value based on the table top’s change in electrical resistance. As these sensors are very expensive and complex to manufacture, the resolution of commercial IR thermal cameras is nowhere near the resolution of a commercial visual light camera and an IR thermal camera with a resolution of 640 x 480 pixels can cost around $35,000 compared to around $40 for a visual light camera with the same sensor size [24].

2.4.6.3 Defect detection using IR Thermography

The use of an IR thermal camera and the knowledge of how infrared radiation is absorbed and emitted from a sample offers the ability to essentially see the inner workings of the object. When heat is applied to the surface of the face sheet, it travels through the individual plies, into the film adhesive and continues into the honeycomb core. If any voids or foreign materials exist, the thermal energy will be blocked or travel at a different rate through these locations. If a location contains an air pocket or void, the thermal energy is not able to pass through this location and the thermal energy will build up above it, causing that location to appear hotter than its surroundings. This is the case when an impact event causes a disbond or delamination creating a small void. In locations where the face sheet is still in thermal contact with the film adhesive and honeycomb core, the thermal energy is able to pass through and the surface temperature of the face sheet decays at a known rate. The imaging setup used is shown in Figure 20, where

the thermal energy is applied to the top of the face sheet using two Halogen bulbs and monitored using an IR thermal camera pointing in the same direction.

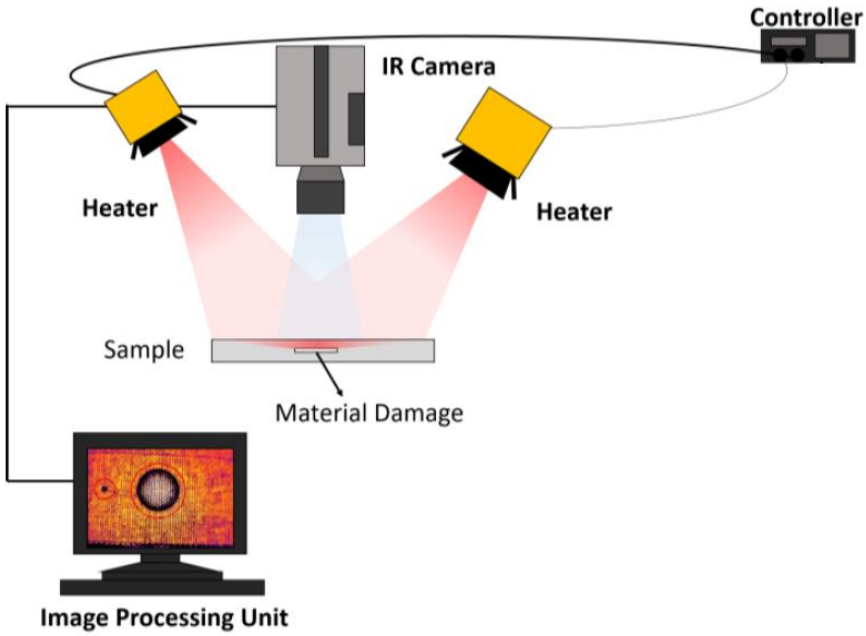

Figure 20: Reflection thermal imaging setup, with the thermal energy and IR thermal camera both located on the same side of the test panel [25].

If the material properties of the face sheet are known when the thermal energy is applied to the face sheet, the temperature will decay at a known rate following the solution of the 1D heat diffusion equation given below by Equation 4 [26].

$$\frac{\partial^2 T(z,t)}{\partial z^2} - \frac{1}{\alpha}\frac{\partial T(z,t)}{\partial t} = 0 \tag{4}$$

Where the temperature at the surface of the face sheet is given by T and the thermal diffusivity of the carbon fiber is given by $\alpha = \kappa/\rho c_p \ (m^2/s)$. The thermal diffusivity is dependent on the face sheet's thermal conductivity $\kappa \ (W/mK)$, the density $\rho \ (kg/m^3)$ and the specific heat $c_p \ (J/kgK)$. The heat source is located at $z_0 = 0$ with an excitation time beginning at $t_0 = 0$.

After applying boundary conditions to the above equation, the temperature at the surface of the face sheet may be expressed by Equation 5 [26].

$$T = \frac{Q}{e\sqrt{\pi t}} \tag{5}$$

where Q is the amount of energy in the thermal pulse and e is the thermal effusivity of the face sheet given below by Equation 6. As mentioned in Section 2.5, an object's thermal effusivity is a measure of its ability to exchange thermal energy with its surroundings [26].

$$e = \sqrt{\kappa \rho c_p} \tag{6}$$

The thermal effusivity $(Ws^{1/2}m^{-2}K^{-1})$ is the product of the thermal conductivity κ, the density ρ, and the specific heat capacity c_p.

The rate at which thermal energy moves through a material is a function of the material's thermal diffusivity given below by Equation 7 [26]; this contains the same inputs as Equation 6 above for its thermal effusivity.

$$\alpha = \frac{\kappa}{\rho c_p} \tag{7}$$

A material's thermal diffusivity (m^2/s) is taken as the material's thermal conductivity κ, divided by the product of the density ρ, and the specific heat capacity c_p.

It is not always possible to distinguish a defective location from non-defective location from a single thermogram, if the contrast difference between the two locations is too small, the two locations appear the same and a defect may go un-noticed until it grows in size.

2.4.6.4 Thermographic Signal reconstruction technique (TSR)

The Thermographic Signal Reconstruction technique (TSR) is a post-processing technique used to reduce the noise of a thermal image, while increasing the temporal and spatial resolution. After taking a sequence of images throughout the heating and cooling phases, the temperature of both a defective and non-defective region can be monitored and recorded. As mentioned above, the temperature of a non-defective region will follow a known decay path, while regions that contain an obstruction will deviate from the known decay curve. Figure 21 demonstrates this property, with the red dot representing an obstruction that causes a buildup of thermal energy above it.

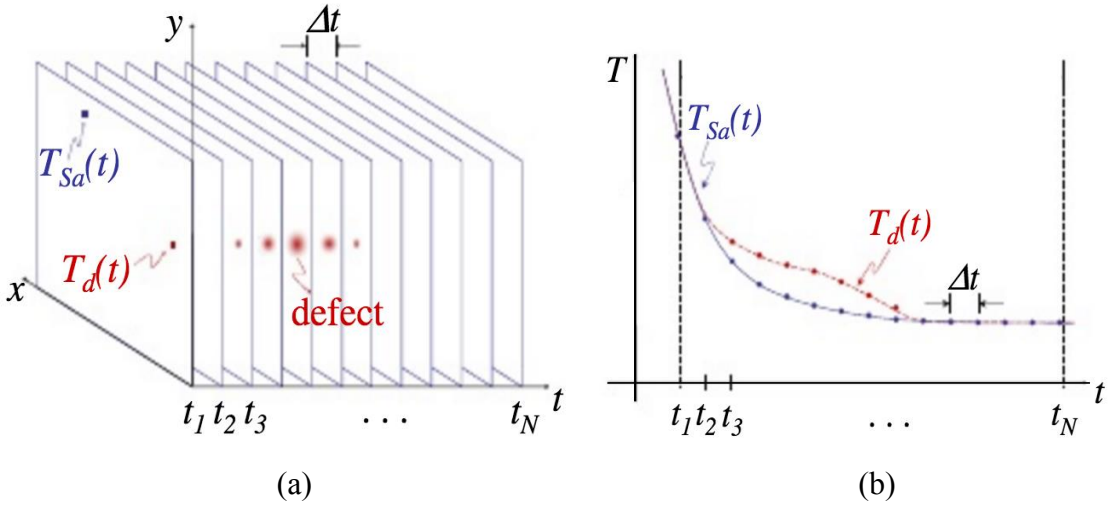

(a) (b)

Figure 21: (a) The x and y dimensions correspond to locations on the microbolometer sensor, while t represents the time dimension. $T_{Sa}(t)$ is the temperature of a non defective region, while $T_d(t)$ is the temperature of a suspected defective region. The time between each frame is given by Δt and is dependent on the camera's frame rate [27].

Figure 21: (b) Shows a typical temperature decay paths for two different locations on the matrix. The T_{Sa} curve is for a non-defective region, while the T_d curve is for a known defective region. The temperature above the defective area follows the same decay as a non-defective area until it starts to deviate from its predicted path around t_2. This deviation is due to something under the surface blocking the energy from passing through, causing a hot spot in the resulting image [27].

Transforming both the temperature and time from Equation 5 into the logarithmic domain with Equation 8 allows for a different perspective on the data. A plot of $\ln(T)\ vs\ \ln(t)$ of a non-defective region, results in a linear plot with a slope of $-1/2$. Knowing that a non-defective region will always produce a straight line with a negative slope, anything that deviates from this curve is due to the thermal energy diffusing at a different rate [28].

$$\ln(T) = \ln\left(\frac{Q}{e}\right) - \frac{1}{2}\ln(\pi t) \tag{8}$$

In post-processing, a low order polynomial is usually fit to the data, which acts as a low-pass filter to keep genuine thermal data, while removing noise and outliers, this works well when the surface of the object is not evenly heated or has contaminates, which can cause hot spots. The order of this polynomial is important, as an algorithm cannot differentiate between noise and actual data of interest, and may lead to clipping of information.

$$ln[T(t)] = \sum_{n=0}^{N} a_n[\ln(t)]^n \tag{9}$$

Equation 10 [28] is then used to reassemble the data back into its original form given by Equation 9 [28].

$$T(t) = exp\left(\sum_{n=0}^{N} a_n[\ln(t)]^n\right) \tag{10}$$

The data is now in the correct form to be differentiated with respect to time. This is quite helpful when a defective area has low contrast compared to its surroundings. The first derivative image given below by Equation 11 [28] gives the rate of cooling, while the second derivative image given below by Equation 12 [28] gives the rate of change in the rate of cooling. Both of these

methods may be used to reveal defects earlier in the decay period, as they show the rate of change vs a single RAW image, which represents the temperature at a single point in time.

$$\frac{dln(T)}{dln(t)} = \sum_{n=0}^{N} n a_n \ln(t)^{n-1} \tag{11}$$

$$\frac{d^2 \ln(T)}{d^2 \ln(t)} = \sum_{n=2}^{N} n(n-1) a_n \ln(t)^{n-2} \tag{12}$$

2.4.7 Infrared Thermography Image Processing

There are many different methods to acquire and interpret thermal images or, as they are more commonly called, thermograms. The first method is to take a single image of your sample and see what information is available at this single point in time. These are taken during the heating or cooling period; this type of thermogram is limited in the fact that time dependent calculations are not possible.

2.4.7.1 Pre-Processing

2.4.7.1.1 Fixed Pattern Noise:

It is quite difficult to apply a perfectly symmetric amount of heat to a sample, and by nature, the sample will contain areas, which receive a larger amount of radiation than others do. This is an undesired effect and leads to false positives when searching for defective areas. The camera's sensor array will also respond differently across its entire surface. A thermal camera's focal plane array works in a similar fashion to that of a CCD array, in which they both contain rows of detectors (pixels), which will all have a slightly different gain between the amount of radiation detected versus the electrical signal it outputs from the sensor. By taking an image of a black body and later subtracting it from the acquired image, the irregularities across each pixel may be adjusted to provide a final image with minimal noise.

2.4.7.1.2 Bad Pixels:

Every type of sensor is prone to having bad pixels, where an individual detector gives values that are either way hotter or colder than its surrounding detectors. These types of pixels are classified into two different categories: 1) Hot pixel or 2) Dead pixel. Dead pixels remain unlit in the acquired image and are usually caused by having a contaminated sensor or a defective detector. A hot pixel gives values that are much higher than its surrounding neighbors and can also be caused by a contaminated sensor or a defective detector outputting an electrical signal much higher than it should. Both of these types of pixels will cause issues in the acquired thermogram if any sort of post processing technique is used. There are ways to correct both types of pixels. The most common is to identify which pixels are bad and replacing that detector's output values with an average of its neighboring pixels. If the sensor is large enough, replacing a single detector's values with its neighbors should not affect the ability to detect a defect in the final thermogram.

2.4.7.1.3 Vignetting:

Vignetting is a type of optical aberration, which causes the pixels around the edges of an image to appear darker than those in the center do. This effect can be caused by either the barrel of the camera physically blocking the light from entering the sensor, which is usually only an issue in poorly made lenses. Or, a more common cause, is due to the elements in the lens body not functioning correctly and the aperture used to acquire the image. If possible, increasing the F-number of the lens reduces the amount of vignetting in the final image.

2.4.7.1.4 Noise Filtering:

As discussed with Fixed Pattern Noise, each detector will receive and output slightly different values, whether that is caused by non-uniform heating of the sample or by an individual detectors gain. Noise can be a byproduct of the sensor, the camera's components or the environment it is operating in. It is common practice to apply a Gaussian or Median filter to the entire image in an attempt to minimize the amount of noise in it. A median filter is a non-linear filter and tends to preserve edges in the image as it replaces the pixel of interest with a median

intensity value of its neighboring pixels. A Gaussian filter is a linear filter and doesn't do a great job at preserving edges; this is due to the fact that the sigma value of the curve governs the amount of smoothing and how much detail is removed from edges. Both filters have their positives and negatives and may be used in conjunction to eliminate unwanted noise.

2.4.7.2 Post-Processing

2.4.7.2.1 Contrast Techniques:

Adjusting the contrast of a thermogram is by far the easiest method to further amplify a defective area with respect to the surrounding non-defective regions. There are many different types of contrast enhancement, from simply identifying a defective area and comparing it to a non-defective region, to taking a sequence of images throughout the heating and cooling periods and looking at the time evolution of individual pixels.

2.4.7.2.2 Absolute Contrast:

This is the easiest and most basic type of contrast enhancement and involves identifying a defective region and subtracting the temperature of a non-defective region shown by Equation 13 [28].

$$C_{Abs}(t) \; or \; \delta T(t) = T_{Def}(t) - T_{SA}(t) \tag{13}$$

Where $T_{Def}(t)$ is the temperature of a selected defective area and $T_{SA}(t)$ is the temperature of a sound or non-defective area. No defect is detected if the contrast is equal to 0.

2.4.7.2.3 Standard Contrast:

Standard thermal contrast is a great technique for reducing the effects of reflections from the sample's surface. It works by subtracting the temperature of the defective and non-defective regions before the heating period has begun shown by Equation 14 [28].

$$C_{Std}(t) = \frac{T_{Def}(t) - T_{Def}(t_0)}{T_{SA}(t) - T_{SA}(t_0)} \tag{14}$$

2.4.7.2.4 Normalized Contrast:

Normalized contrast takes into account the maximum temperature reached and adjusts the image's dynamic range to increase its contrast shown by Equation 15 [28].

$$C_{Norm}(t) = \frac{T_{Def}(t)}{T_{Def}(t_{max})} - \frac{T_{SA}(t)}{T_{SA}(t_{max})} \tag{15}$$

2.4.7.2.5 Plateau Equalization and Advanced Plateau Equalization

FLIR's ResearchIR software offers many algorithms that may be applied to an acquired thermogram to improve image detail and contrast. The algorithms do not operate on or affect the radiation information collected by the camera's sensor, but rather change how the information is visually displayed in an image. Both of these algorithms are non-linear histogram based, which enhances the image's contrast and detail. While the Plateau Equalization algorithm is publicly available, the Advanced Plateau Equalization algorithm is a FLIR proprietary product [29]. Both of these algorithms work by computing an upper and lower limit of an images intensity values. The upper limit is used to constrain the noise, while the lower limit works to clip the background pixel values. Once the limits have been set, the intensity values between the two limits are stretched, providing an image with an enhanced contrast.

3 EXPERIMENTAL METHOD

In order to evaluate IR thermography as a competitive method of detecting flaws and defects in composite face sheet honeycomb panels, test coupons with known types of defects and locations were needed. Composite face sheet honeycomb panels, which closely resemble an F/A-18 aircrafts control surfaces [21] were manufactured and subjected to impact testing and non-destructive testing using IR thermography. The methods used for manufacturing the honeycomb panels, creating known flaws and damage states in the panel as well as techniques for scanning and processing the acquired data are presented in this section. Seven studies were conducted, each requiring different types of flaws or damage; as listed below.

1. Detecting core crush: Different diameters of core crush regions were created using impact testing.
2. Detecting disbonds between the face sheet and core: Different diameters of disbonded regions were created using impact testing. Core crush was also present in these panels.
3. Detecting flaws at different depths: A test panel containing flat bottom holes at known depths representing air pockets or voids was used.
4. Detecting core separation: The honeycomb core was pre-sliced and pre-crushed before the face sheet was adhered.
5. Distinguishing the type of flaw: IR images of each type of flaw were compared and discussed to help identify and distinguish between them from an IR scan.
6. Detecting water ingress: IR images of water ingress present inside of individual honeycomb core cells were imaged.
7. Time dependent calculations: The Thermographic Signal Reconstruction method was applied to detect delaminations and disbonds at an earlier time period than a single thermogram and calculate its corresponding depth.

3.1 Manufacturing of Composite Face sheet Sandwich Panels

This section will discuss the steps necessary to manufacture each of the test panels used for this thesis. The face sheets and sandwich panels were manufactured at the Royal Military College using pre-impregnated carbon fiber (prepreg), aluminum honeycomb core and film adhesive.

3.1.1 Face Sheet Manufacturing

The first step in manufacturing the test panels was to make the composite face sheets. The pre-impregnated carbon fiber (prepreg) was purchased as a large roll of unidirectional fibers all running parallel to each other which had been presoaked in an un-cured epoxy and required curing at a specific temperature and pressure. The test coupon face sheets were all manufactured using Rock West Composites 14002-D standard modulus prepreg. The prepreg contains T700S SC-12k carbon fiber strands with Newport 301 resin. The prepreg carbon fiber selected for testing was chosen to closely resemble the type of carbon fiber used for the external body panels and control surfaces of the F/A-18 on fighter aircraft [13,21]. Once cured, each ply had a thickness of 0.152 mm (0.006 inches), which contains a 65% fiber volume with a 35% resin volume. Table 2 provides the typical mechanical properties of a single ply of cured prepreg in the 0 degree orientation at a room temperature of 23°C.

Tensile Strength	2250 MPa	ASTM D 3039
Tensile Modulus	127 GPa	
Compressive Strength	1247 MPa	ASTM D 3410
Compressive Modulus	123 GPa	
Flexural Strength	1500 MPa	ASTM D 790
Flexural Modulus	98 GPa	

Table 2: Typical mechanical properties of a single ply of carbon fiber in the 0 degrees orientation at a room temperature of 23°C [30]. The full data sheet is provided in Appendix B.

The number of plies used, orientation of the individual plies and surface preparation for adhering the face sheet to the honeycomb core are provided for each of the manufactured test panels in Table 3.

Test Panel ID	Number of Plies	Layup Orientation	Surface Preparation
Test Panel 1**	4	[0/90/0/90]	Acetone
Test Panel 1	5	[0/90/0/90/0]	Acetone
Test Panel 2	5	[0/90/0/90/0]	120 Grit Sand
Test Panel 3	6	[0/90/0/90/0/90]	120 Grit Sand
Test Panel 4	7	[0/90/0/90/0/90/0]	120 Grit Sand
Test Panel 5	8	[0/90/0/90/0/90/0/90]	120 Grit Sand
Test Panel 7	5	[0/90/0/90/0]	Acetone
Test Panel 9	6	[0/90/-45/+45/90/0]	Acetone
Test Panel 10	4	[0/90/0/90]	Acetone
Test Panel 11	5	[0/-45/90/+45/0]	Acetone

Table 3: Number of plies, layup orientation and surface preparation for each test panel. 1** is a preliminary test panel used for a proof of concept.

The first step in manufacturing the face sheets was to cut the prepreg carbon fiber to the required size and orientation for each ply in the layup, these rectangles varied between 152-305 mm depending on the test panel. Each individual ply was stacked on top of the previous ply and compressed together using a rolling pin, making sure no air pockets existed in between them. The stack of plies was then placed in-between 2 layers of release film and sealed around the edges in preparation for vacuum pressing them together. This is shown in Figure 22 where two face sheets, each containing five plies were sealed and ready for curing. The prepreg carbon fiber sheets required delicate handling when assembling the face sheet layup, since forcefully handling the fibers may cause small separations in-between individual fibers, which leads to small air gaps or areas where excess resin may pool. Small gaps like these can lead to initiation sites for microcracking or delaminations between plies.

Figure 22: Two face sheets (5 ply, [0/90/0/90/0] vacuum pressed together and ready for curing.

The face sheets were then cured in a custom built oven, which was also used for curing the film adhesive to the core. The oven consisted of heating coils adhered to the underside of a half inch thick aluminum plate, which evenly distributed the heat to the face sheets. A top cover made from a heat resistant silicone membrane was placed over top of the face sheets to create a seal as shown in Figure 23. A pump was used to apply a 29 inchHg (14 psi) vacuum throughout the curing process to apply pressure to the face sheets, while simultaneously evacuating any trapped air out from in between the individual plies. The face sheets were cured at 135°C for 2 hours, while holding a 29 inchHg (14 psi) vacuum. A ramp up and ramp down rate of 2.5°C per minute was used.

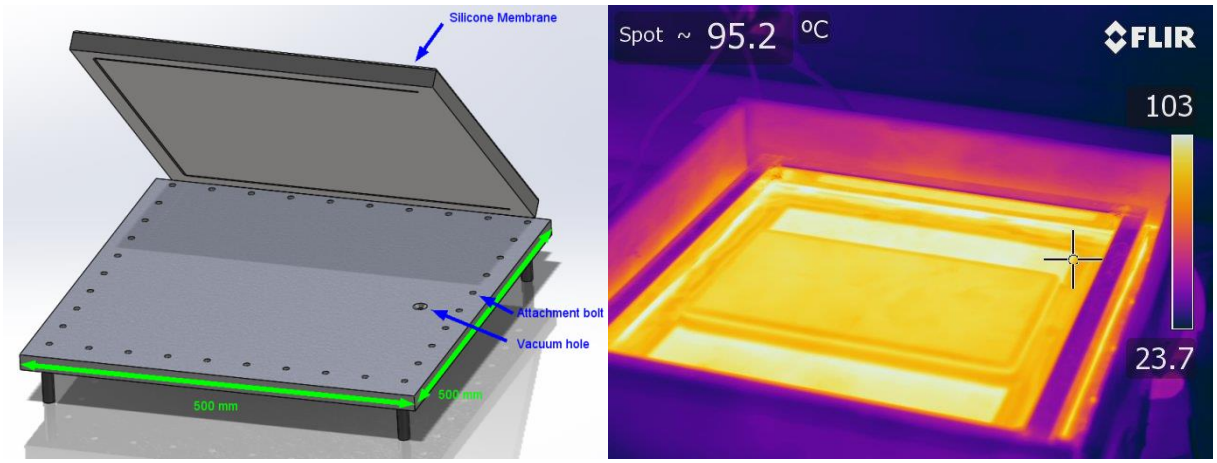

(a) (b)

Figure 23: Aluminum curing surface (500 x 500 x 20 mm) with the silicone membrane frame sitting at a 45˚ angle prior to air evacuation (a). Silicone membrane stretched over curing surface with one face sheet in its curing cycle (b).

After the face sheets had been cured, the temperature was ramped down, while maintaining the same vacuum pressure. Holding the pressure for the cooling cycle prevents warping and residual stresses in the face sheets as they cool to room temperature. Figure 24 provides an example of two cured and cooled face sheets.

Figure 24: Two 152 mm x 305 mm (6.0 inch x 12 inch) (5 ply, [0/90/0/90/0]) post-cured face sheets.

The surface of the face sheets were wet sanded using a 120 grit sandpaper; which followed the film adhesive manufacturers recommended preparation guidelines [31,32]. This process removed some of the cured resin in between the individual strands of carbon fiber and provided more surface area for the film adhesive to adhere to, resulting in a stronger bond. A comparison of a non-sanded face sheet to a face sheet wet sanded with 120 grit sandpaper is provided in Figure 25.

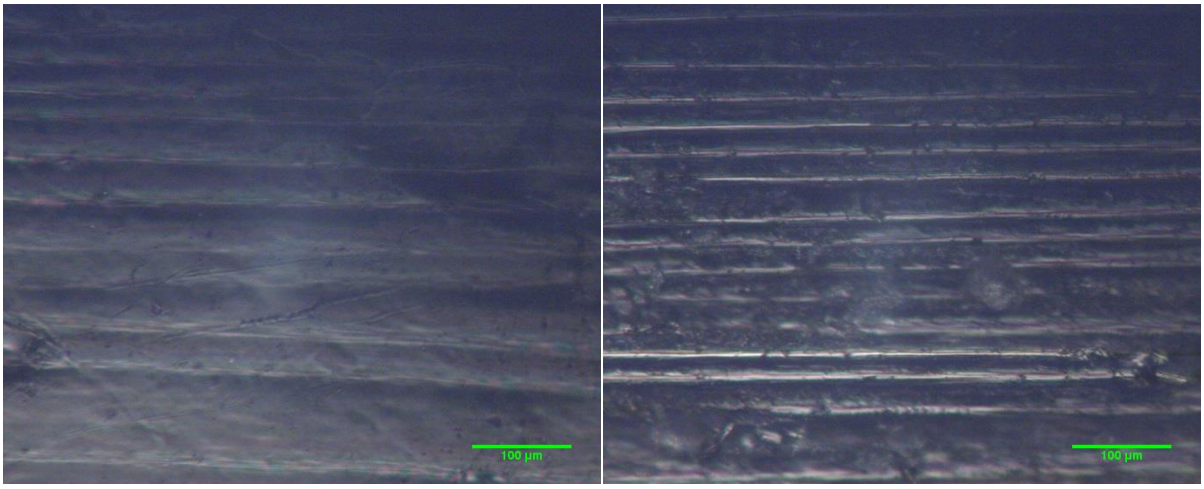

(a) (b)

Figure 25: A non-sanded face sheet (a) verses a face sheet wet sanded with 120 grit sandpaper (b). For context, each fiber is approximately 7 µm in diameter.

3.1.2 Panel Assembly

After the face sheets had been sanded and thoroughly cleaned with acetone, they were adhered to the aluminum honeycomb core which was selected to represent the honeycomb core typically used for the F/A-18 fighter aircraft [13]. The core material was 5052-H34 aluminum, with a cell size of 0.125 inches (3.175 mm), a wall thickness of 0.007 inches (0.178 mm) and a thickness of 0.5 inches (12.7 mm). The ribbon direction of the core was consistently oriented in the long direction of the panel. The honeycomb core was cut to size using an X-Acto knife and Cytec FM film adhesive was used to bond the face sheets to the core. Two different types were used, FM 73M and FM 300K, which were selected based off of literature describing manufacturing and repair methods for an F/A-18 rear horizontal stabilizer [13]; these were both

readily available for testing. Select properties for each adhesive are provided in Table 4, while a comprehensive description is provided in the data sheets in Appendix B.

Adhesive	Weight (gsm)	Thickness (mm)	Tensile Shear (MPa)	Honeycomb peel (Nm/m)	Flatwise Tensile (MPa)
FM 300K	390	0.32	29.8	66.0	3.0
FM 73M	420	0.38	47.2	140	8.9

Table 4: Mechanical properties of Cytec FM 300K and FM 73M film adhesive [31,32].

One property of the honeycomb panels that is critical to its performance is the presence of an adhesive fillet radius where the cell walls meet the face sheet. The process of creating these fillets followed the methods presented by *Rion, et al.* [32]. The same process and custom built oven that was used to cure the face sheets was also used to cure the adhesive joining the face sheet to the core. The face sheets were adhered to the core one side at a time, with one face sheet placed on the aluminum surface of the oven, followed by the film adhesive and then the honeycomb core. An aluminum plate was then placed on top of the honeycomb core to prevent the silicone membrane from crushing the cells and corners of the honeycomb once 14 psi of down force was applied from the 29 inchHg vacuum. The oven was ramped up to the required 120˚C at a rate of 2.5˚C per minute to begin the film adhesive's curing process. The fillets are formed during the curing process when small bubbles were created within the film adhesive from degassing, this helped push the film adhesive up the cell walls to form a fillet. This method produced consistent fillets throughout all of the test panels, and only one impact event out of all the tests performed in this thesis caused the film adhesive to become disbonded from the honeycomb core. An example of an adhesive fillet produced using this method is shown in Figure 26.

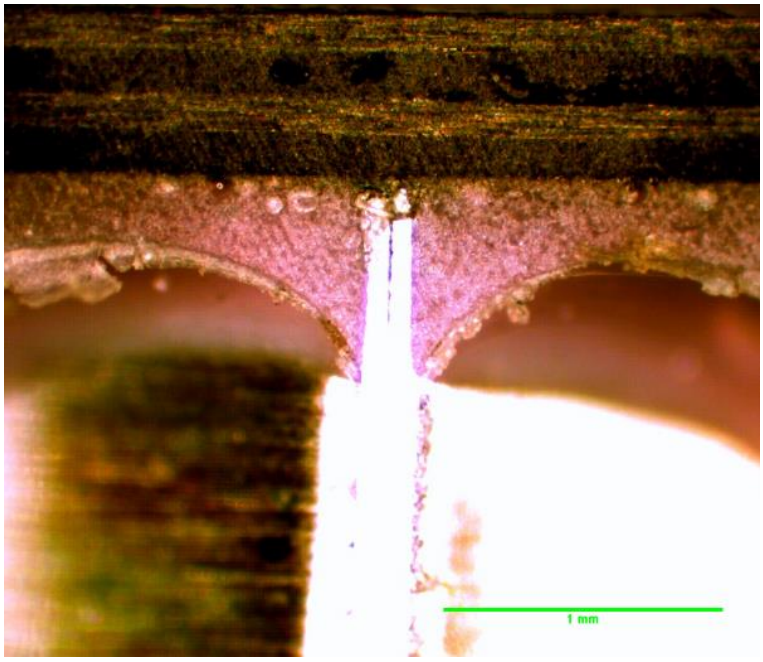

Figure 26: Capillary action and small bubbles formed during the curing process help the adhesive climb the honeycomb cell wall. (Scale Bar = 1.0 mm)

This process was then repeated to adhere the second face sheet to the opposing side of the aluminum core to achieve a complete sandwich panel. Figure 27 shows the composition of a typical test panel as well as the layup orientation for the unidirectional carbon fiber for a 5 ply face sheet.

PROPreg 14002-D CFRP [0/90/0/90/0]
FM-300 Film Adhesive
5052-H34 Aluminum Honeycomb Core
FM-300 Film Adhesive
PROPreg 14002-D CFRP [0/90/0/90/0]

Figure 27: A typical 5 ply honeycomb sandwich panel used for testing.

3.2 Creating Composite Honeycomb Panel Damage.

As mentioned in Section 2.1 there are many different types of damage that occur in composite honeycomb panels following an impact event. Different types of damage were created using various techniques as outlined below:

1. Core crush: The honeycomb panels were impacted using a drop tower apparatus.
2. Face sheet to adhesive disbond: The honeycomb panels were impacted, but the face sheet was not sanded prior to adhesive curing.
3. Core separation: The honeycomb core was pre-sliced and pre-crushed prior to assembly, leaving the damaged cells with no impact damage to the face sheet.
4. Film adhesive to core disbond: The honeycomb core was manually pried away from the face sheet, leaving the face sheet and film adhesive adhered to one another, while the core became disbonded from the film adhesive.
5. Delaminations in-between laminate plies: The face sheet was impacted using various diameters and masses. A small diameter, small mass impactor traveling at a high velocity and a large diameter, large mass impactor traveling at a low velocity were used.
6. Microcracking in the face sheet: Test results from number 6 showed that delaminations created using both combinations of impactors also created micro and matrix cracking. The same impactors and energies were repeated for this study.

Manufacturing defects were also considered, including excess adhesive and porosity caused from improperly curing of the honeycomb panels. While water ingress within the honeycomb cells was manually added, representing an environmental effect to the test panel. Both methods for recreating these types of defects are shown below.

1. Excess adhesive: Two layers of adhesive were stacked on top of one another in a defined area, with the rest of the face sheet being adhered with one layer.
2. Creating water ingress: Small holes were drilled to the back side of the panel and filled with water using a syringe. The holes were then sealed using silicone and the test panel was placed in the freezer until testing.

3.2 1 Impact Tower

To recreate impact damage that may occur during a honeycomb panel's service life provided by the first six bullet points above, an impact tower was designed and built. Building the impact tower allowed different parameters to be altered such as the mass of the impactor (0.067, 0.150 and 1.010 kg), the diameter of the impactors (25.4, 52.6 and 63.1 mm), and the drop height (0.2-2.14 m). The specifications for each are given in Table 5 and examples are shown in Figure 28.

Impactor ID	Mass (kg)	Diameter (mm)
1	0.150	52.6
2	0.067	25.4
3	1.030	63.1

Table 5: Physical properties for each Impactor used.

(a) (b)

Figure 28: (a) Impactor 1 with a mass of 0.150 kg, and a diameter of 52.6 mm. (b) Impactor 2 with a mass of 0.067 kg and a diameter of 25.4 mm and impactor 3 with a mass of 1.030 kg and a diameter of 63.1 mm.

The panels were placed at the bottom of the drop chute and were secured to the baseplate by four rubber tipped clamps as shown below in Figure 30. Having rubber on the tips of the clamps prevented the clamp tip from scratching and damaging the face sheet. Deep scratches and gauges can potentially decrease the panel's strength and made IR thermal imaging difficult with a non-uniform surface finish. Once the release pin was pulled, the impactor traveled down the chute and impacted the test panel; the top face sheet was pushed downwards towards the –Z-axis and the rubber tips provided the test panel a degree of freedom in the X-axis and Y-axis allowing it to flex slightly through the 76 mm by 127 mm (3.0" x 5.0") rectangular hole in the base plate. This follows the ASTM D7136 guidelines for measuring the damage resistance of fiber reinforced matrix composites from an impact event [33]. Figures 29 and 30 show the impactor setup and coordinate system used.

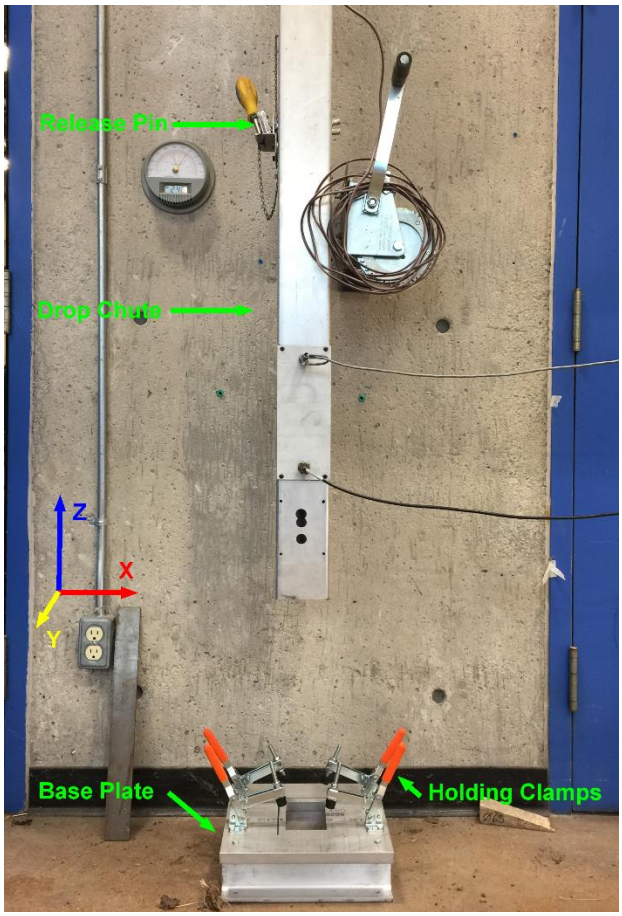

Figure 29: Drop tower used for impact testing. The impactors are held at the required height in the square aluminum chute with a pin, which is pulled to release the impactor.

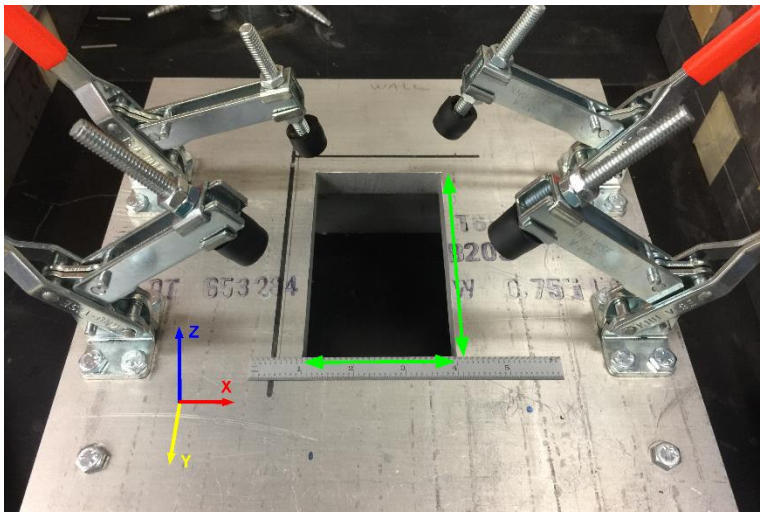

Figure 30: Drop tower base plate used for impact testing. The test panel is held in place via the four rubber tipped clamps. The rectangular hole opening is 76 mm by 127 mm used to set the boundary conditions.

3.2 2 Delamination of plies

The impact tower was used in combination with Impactor 2, which has a mass of 0.067 kg and was dropped from 2.1 m traveling at 6.4 m/s at impact to create a delamination in-between individual plies in the face sheet. This combination of velocity and impactor diameter was able to create a disbond in-between the face sheet and film adhesive as well as delaminations in the bottom 3 plies while leaving the surface of the face sheet intact. Figure 31 shows a section of the bottom ply whose fibers run normal to the page delaminated and remaining adhered to the film adhesive, while the rest had relaxed back.

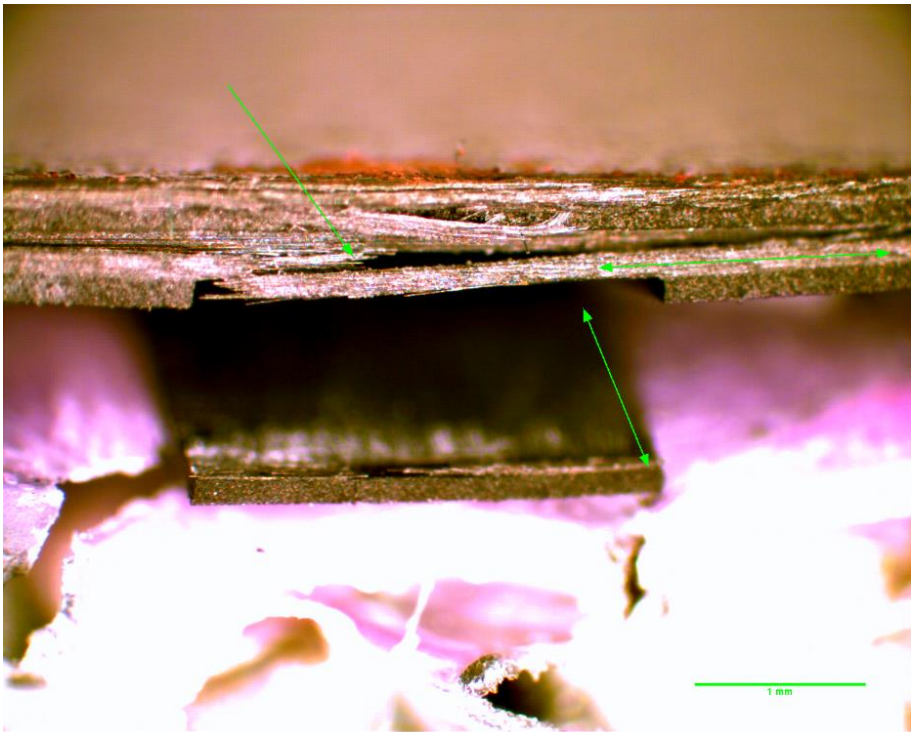

Figure 31: Impactor 2 (Mass: 0.067 kg, Diameter: 25.4 mm, Height: 2.1 m, Velocity: 6.4 m/s): Delaminations occurring within the bottom three plies. This impact event also caused micro cracking down through the bottom three plies which initiated at a delamination just below the top ply. (Scale Bar = 1.0 mm)

3.2.3 Matrix cracking across multiple plies

The impact tower was again used to recreate matrix and micro cracking. Impactors 1, 2 as well as Impactor 3 were all successful in producing matrix cracking given a high enough velocity. Impactor 1, which having a mass of 0.15 kg was dropped from 1.0 m and traveling at 4.4 m/s at the time of impact, was able to produce the damage shown in Figure 32. It was found that a much higher impact velocity produced matrix cracking in the face sheet as the fibers did not have enough time to flex during the impact, but broke instead.

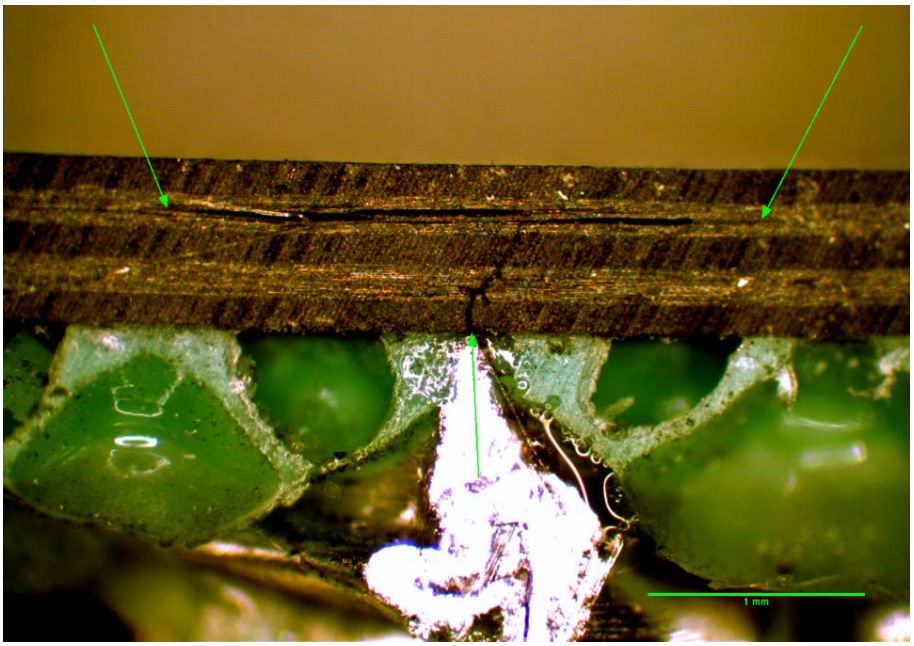

Figure 32: Impactor 1 (Mass: 0.150 kg, Diameter: 52.6 mm, Height: 1.0 m, Velocity: 4.4 m/s): Microcracking, which initiated at a delamination just below the top ply. The cracking initiates within the second ply and propagates down through the remaining three plies until it hits the bottom side of the face sheet. (Scale Bar = 1.0 mm)

3.2.4 Porosity

Increased porosity in between the individual plies of carbon fiber was achieved by decreasing the pressure applied by the silicone membrane during the face sheet curing process to 7 psi, which is half of the original 14 psi. The vacuum system was not able to properly compress the plies and evacuate all of the trapped air bubbles, which resulted in small voids being formed as shown in Figure 33. This results in a poor bond in-between plies and an overall reduced strength in the face sheet.

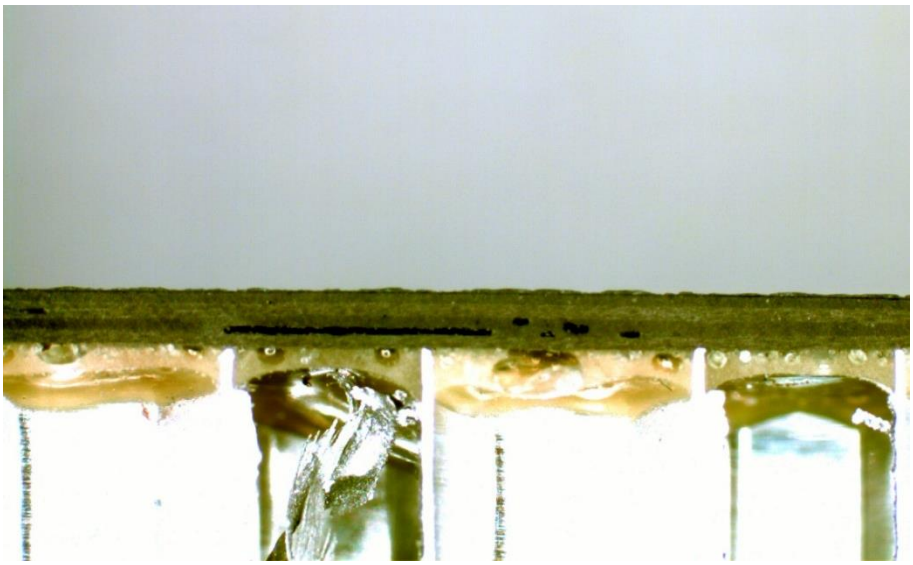

Figure 33: Porosity occurring within the third ply. This is due to air being trapped during the curing process.

3.2.5 Excess adhesive

This type of damage was created by adding an extra layer of film adhesive to a small section of the test coupon before the adhesive curing process, this is shown below in Figure 34 with a layer of green and yellow film adhesive. Excess adhesive in sections of a panel can also occur during the manufacturing stage of the face sheets due to the resin flowing during the curing process.

Figure 34: Excess adhesive created by adding an extra layer (Green) of film adhesive before the curing process.

3.2.6 Face sheet to adhesive disbond

To recreate a face sheet to film adhesive disbond, the face sheet was left smooth prior to bonding it to the honeycomb core. The wet sanding with 120 grit sandpaper was omitted to create this type of damage, which did not provide the film adhesive as much surface area to bond to. Once the test panel was impacted, the face sheet was depressed down and became disbonded from the film adhesive, which allowed the face sheet to relax back to its original position due to the residual stress in the fibers. Disbonds were successfully created using Impactor 1, which was dropped from 0.2–1.0 m with impact velocities between 2.0-4.4 m/s. Figure 35 shows a disbond resulting from Impactor 1 dropped from 0.7 m that had an impact velocity of 3.7 m/s. The disbond region is indicated by two green arrows which is where the face sheet and film adhesive visually start to separate.

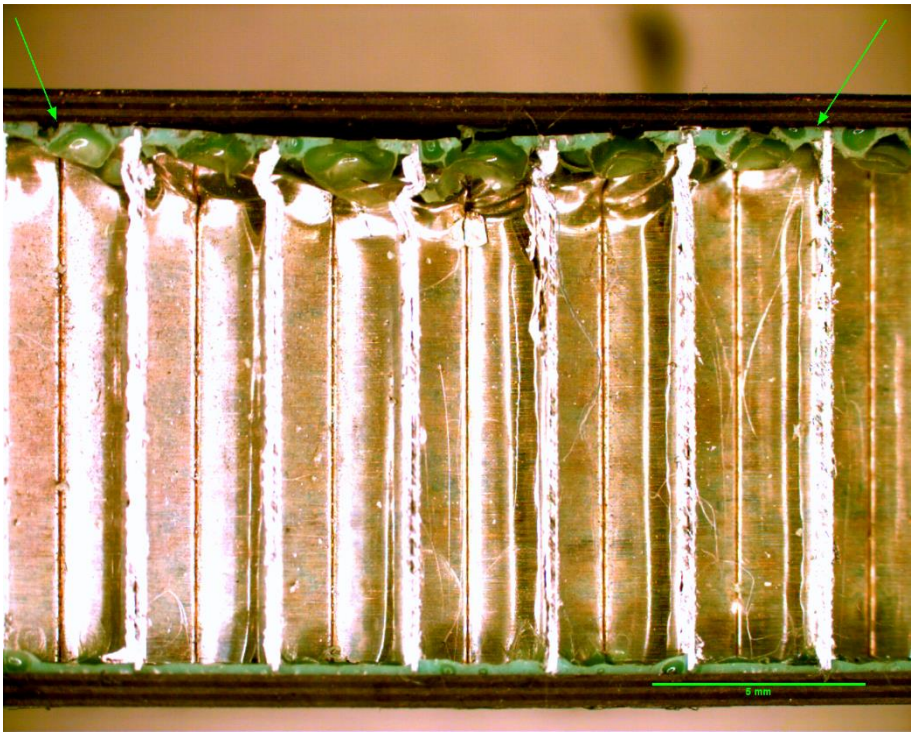

Figure 35: Impactor 1 (Mass: 0.150 kg, Diameter: 52.6 mm, Height: 0.7 m, Velocity: 3.7 m/s): A disbond occurring in between the face sheet and film adhesive. (Scale Bar = 5.0 mm)

3.2.7 Core Cracking

Cracking or ripping of the core can initiate from crushed honeycomb cell walls when subjected to fatigue loading. If the panel is impacted, causing core crush, the small sharp corners can be an initiation site for cracks. To recreate core cracking, an X-Acto knife was used in conjunction with Impactor 1 to pre-damage the honeycomb core before the face sheet was adhered to it. Two vertical slices (a, b) were made to the top surface of the honeycomb core while two dents (c, d) were created by statically pushing down an impactor to crush the cell walls. Both sets of damage were created without impacting the panel. This helped isolate the damage mode occurring to the cell walls while removing damage modes occurring to the face sheet. An overhead view of the created damage is shown below in Figure 36.

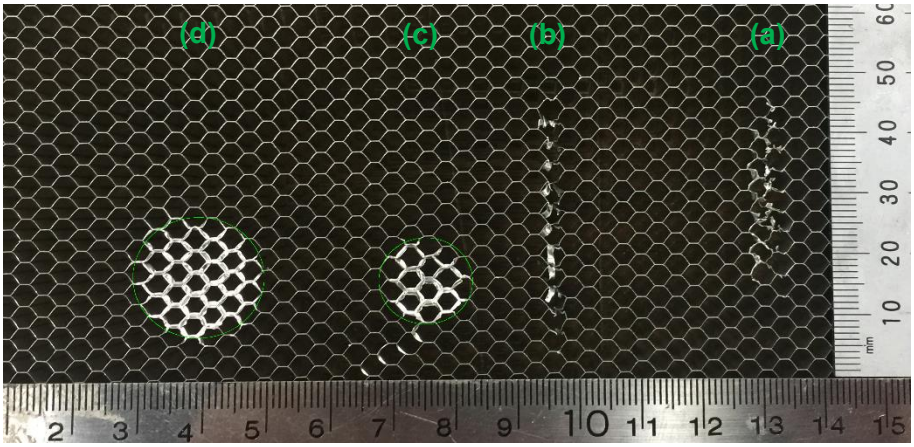

Figure 36: Crushed honeycomb core before the face sheet is adhered. Large crush (d) (D=19.8 mm, A =290 mm^2) Small crush (c) (D=14.4 mm, A =150 mm^2). Large slice (b) (L=28.5 mm) Medium slice + crush (a) (L=23 mm).

To create the second set of damage representing a discontinuity of the cell walls, an X-Acto knife was pushed into the side walls of the honeycomb cells, which left a triangular slice approximately 2.5 cm deep at depths of 2.5, 3.5, 6.5 and 8.5 mm from the surface. A side view of the created damage is shown below in Figure 37.

Figure 37: Horizontally sliced honeycomb core. This was created by pushing an X-Acto knife blade into the side walls of the cells.

3.3 IR Thermography Apparatus

The IR thermography camera mount and heating system was designed and manufactured at the Royal Military College of Canada by myself, including all Matlab and Arduino code used. Image processing algorithms were provided by FLIR Systems and were applied using their FLIR ResearchIR software [29].

3.3.1 Camera and Mount

As mentioned in Section 2.4.6.1, the camera and the heat source should be positioned as close as possible to the normal of the test coupon's surface. This not only minimizes the amount of radiation reflected off of the surface, but also maximizes the amount absorbed by it. Having the camera and the heating source both perpendicular to the test coupon is not possible however, but both should be placed as close as possible together. A camera test stand was designed to try and achieve this, with the thermal camera looking directly down at the test coupon through a hole in the aluminum mounting plate with two 500 Watt halogen bulbs underneath the mounting plate on either side of the lens. The mounting plate contains an electronics box, which houses the relay control board and Arduino used to control the camera and lighting system. The mounting plate is attached to adjustable carbon fiber legs, which allows the whole system to operate on a desktop or be held against an aircraft for insitu scanning. The test stand is pictured in Figure 38 without the camera, which mounts to the T bracket and looks directly through the hole in the mounting plate.

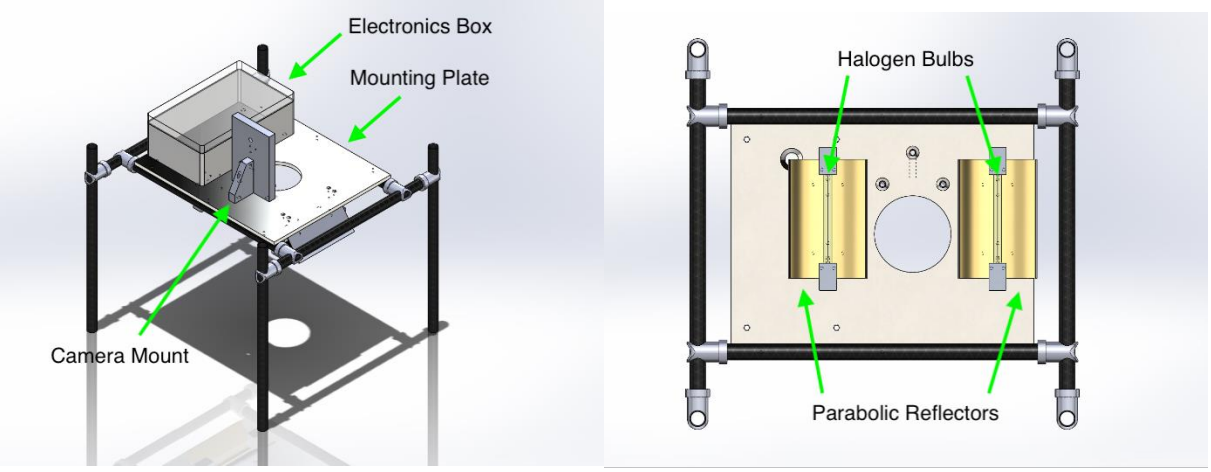

(a) (b)

Figure 38: (a) Camera and halogen bulb test stand. The camera looks directly down through the hole, perpendicular to the test panel surface. (b) The two halogen bulbs are contained in the parabolic reflectors, which are covered with a reflective thermal tape.

3.3.2 Heating

Many sub-studies were performed in order to find the best method to acquire consistent and useful thermograms. As a thermal camera is very sensitive to fluctuations in temperature, heating the test coupons uniformly can be an issue and may lead to detecting false positives, while searching for defective areas. Therefore, it is important to heat the surface as uniformly as possible and for the shortest amount of time possible. Heating the surface for an extended period of time will cause the acquired thermograms to be very saturated, making it difficult to extract useful information. Having a powerful energy source to provide thermal energy in a short period of time is desirable. A heat gun can provide an adequate amount of thermal energy to the face sheet of the test coupon, but does not provide a very uniform spread as shown in Figure 39. The center of the heat gun tends to be hotter than the outer radius, similar to a Gaussian distribution, and makes finding defective areas difficult.

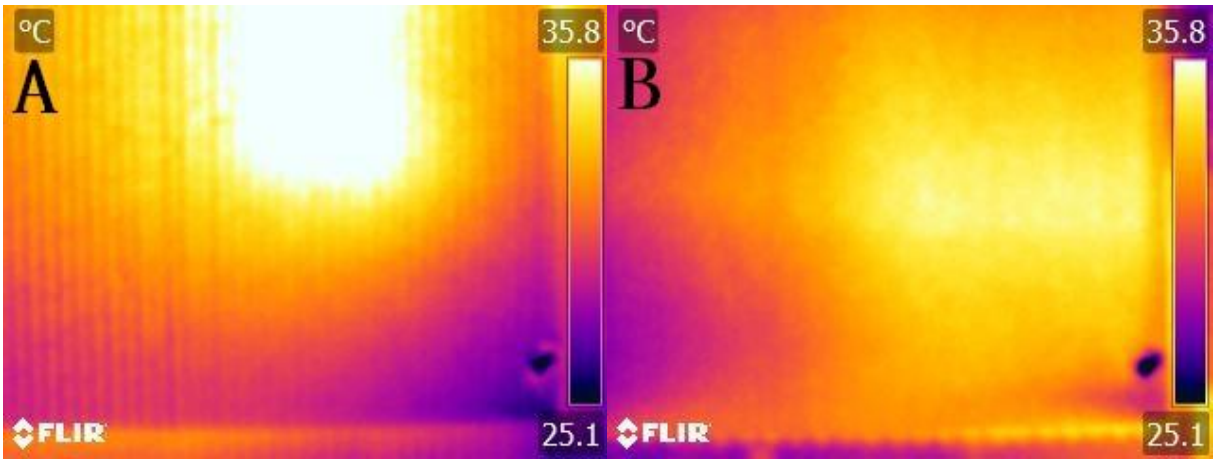

(a) (b)

Figure 39: (a) Thermal energy distribution of a heat gun verses a single halogen bulb (b).

Tubular bulbs can provide a lot of energy in a short period of time, and do not require the same amount of time for a heating coil to heat up as required for a heat gun. This is an important factor, as sending a single pulse of energy through the sample provides the best thermograms. Xenon bulbs are able to output a lot of energy in a short period of time and are used in most commercial thermography systems. However, these types of bulbs tend to be quite expensive and require high voltage capacitors to provide a quick discharge of energy to ionize the Xenon gas in the tube. Halogen bulbs may be used without the need of any capacitors or transformers and provide an adequate amount of thermal energy to the surface. Uniformly heating the surface still proves to be difficult when using tubular bulbs since it depends on their orientation with respect to one another. It was found that if the area that one bulb is heating over laps with the area that another bulb is heating, this small overlap is enough to raise the temperature in that location by a few degrees, causing an unwanted hot spot. To combat the problem of overlapping heating areas and to direct as much radiation as possible, parabolic reflectors were designed to direct the thermal radiation from the halogen bulbs evenly onto the test panel. The parabolic nature of the reflectors gather the randomly emitted photons and redirect them into a parallel beam towards the test coupon. This provides a more uniformly heated surface and uses more of the emitted radiation as opposed to a non-collimated source. As the bulbs are located at a small angle away from the principle axis of the camera lens, the parabolic reflectors were designed with a hinged base to angle the reflector and uniformly direct the radiation to the sample's surface.

Precise timing control of the halogen bulbs is required to keep each test consistent as well as provides a time stamp when the radiation was applied, compared to when a defect is detected. This is discussed in detail later on how to derive the depth of a defect based on its detection time. To control the halogen bulbs, an Arduino computer was paired with an electronic relay board. The electronic relay board either opens or closes its circuit to provide power to the halogen bulbs when a command is sent. The Arduino controls the relays opening and closing by receiving commands from a PC. Various codes were written to control and synchronize all of these subsystems together including the connected thermal camera. By using MATLAB to synchronize and control the camera and the halogen bulbs, variables can be changed depending on which test trial is being performed. The period of time that the bulbs stay on for, the time in which the camera starts to acquire frames, as well as what frequency and number frames are required, can all be controlled using this code.

3.3.3 Image Processing

A FLIR T620 thermal camera was used to acquire all of the thermograms taken. This camera model has a sensor resolution of 640 x 480 pixels and a spectral range of 7.5 μm to 14 μm. It is able to measure temperatures between -40 to 650 $^{\circ}$C with a sensitivity of 0.04 degrees Celsius [24]. This model of camera is actually designed to be hand held and portable so it may be utilized in the field, but for the studies presented here, it was fixed to the camera test stand throughout testing. The camera test stand was designed to achieve consistent results across each of the trials, where the sample was kept at a constant distance from the halogen bulbs as well as the camera lens. Another reason the camera test stand was designed was for the ability to take a sequence of images, while the sample was going through its heating and cooling phases. Taking a sequence of images as opposed to a single static image, allows for time dependent calculations to be applied to the acquired images throughout the heating and cooling phase.

The FLIR T620 IR thermal camera is able to take a sequence of images at a set frequency or video at a set frame rate. Video formats such as .wmv and .mp4 are file extensions, which put all the acquired frames into a container and add audio, codecs and other non-required information to the final file. As time dependent calculations of the acquired frames was of interest, breaking down a video into separate frames and removing unwanted information

contained in each frame is not recommended. Saving the sequence of images as separate uncompressed files such as a .tiff format is better for manipulating and handling the acquired data.

To organize the acquired frames, MATLAB code was written to take a sequence of images and organize them into a 4-D matrix data cube with the dimensions [height, width, intensity, frame]. The color channel in an image contains three values corresponding to the intensity of each the red, green and blue (RGB) channels, which when combined in different intensities can produce any color. The color red for example is [255, 0, 0] with 8 bits used per channel and an intensity value in the range of (0-255). In order to process the sequence of images, individual frames, which are technically a 3-D matrix, need to be reformatted into a 2-D array with the structure [height, width, intensity], removing the third dimension currently occupied by the [255, 0, 0] RGB values. To convert a RGB image to a gray scale image, intensity values of each color channel at each pixel are combined into a weighted sum to get a final pixel intensity in the range of (0-1). To save a step in post processing, it is best to initially take the thermograms in grayscale if the camera has this capability. MATLAB code was written to perform the restructuring with the use of MATLAB's *squeeze* function. As the color channel is the only array using the fourth dimension, using the *squeeze* function returns an array with the same elements but removes all singleton dimensions. The result is a 2-D image with an intensity value corresponding to the temperature at each pixel [height, width, intensity]. The images are now in the correct format and can be reassembled into a 4-D matrix data cube with the dimensions [height, width, intensity, frame]. Contrast techniques may be applied to each individual frame and the thermographic signal reconstruction method can be utilized to track an individual pixels temperature throughout the testing phase, frame by frame.

4 RESULTS AND DISCUSSION

Seven studies were performed to investigate IR thermography's ability to detect and identify different flaws and damage types caused by low velocity impacts on composite face sheet honeycomb panels. The resulting thermograms are compared and discussed, providing visual comparisons on how to distinguish each type.

1. Detecting core crush: IR images of different diameters of core crush regions were compared. No additional damage modes were present.
2. Detecting disbonds between the face sheet and core: IR images of different diameters of disbonded regions were compared. Core crush was also present in these panels.
3. Detecting damage at different depths: IR images of a test panel containing air pockets at different depths were compared to evaluate IR thermography's ability to identify relative damage depths.
4. Detecting core separation: IR images of pre-sliced and pre-crushed damage to the core before the face sheet was adhered were imaged to identify the size and depth of the flaw.
5. Distinguishing flaw types: IR images of each of the different flaw types were compared and discussed.
6. Detecting water ingress: IR images of water ingress, present inside of individual honeycomb core cells, were examined.
7. Thermographic Signal Reconstruction method: IR images of a test panel containing air pockets at different depths were imaged and the Thermographic Signal Reconstruction method was applied to decrease the inspection time and calculate the defects depth.

4.1 Detection of Core Crush

This study focused on IR thermography's ability to detect core crush. Four different test panels were manufactured, with face sheet thicknesses between 0.76 -1.22 mm (0.03-0.048 inch) composed of between 5 and 8 laminate plies. Using impactor 1 (52.6mm diameter), they were subjected to 6 separate impacts each with a constant impact energy of 1.18 J. Core crush was the only damage mode present, as the face sheet remained adhered to the honeycomb core following impact and resulted in a residual dent on the surface of the face sheet. The depth of each residual dent was measured using 3D laser scanning. Figure 40 defines the residual face sheet indentation depth (Δ_{RMAX}) along with the residual indentation width ($2R_{ind}$). The width of the core damage ($2R_{damage}$) extends past the visual indentation on the surface.

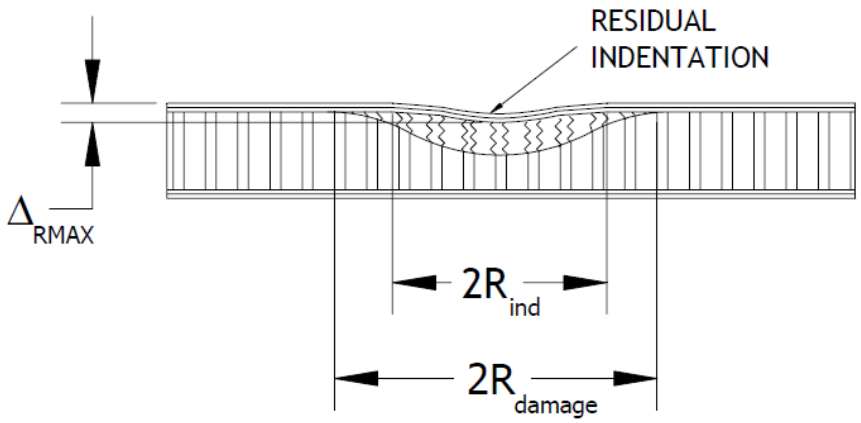

Figure 40: Residual indentation of the face sheet and honeycomb core. The change in the face sheet depth is given by Δ_{RMAX} where the indicated surface damage is given by $2R_{ind}$ .The diameter of the core crush from a cross sectional slice is given by $2R_{damage.}$ [34].

The test panels manufactured for this study used a honeycomb core material of 5052-H34 aluminum, a cell size of 0.125 inches (3.175 mm), a cell wall thickness of 0.007 inches (0.178 mm) and a panel thickness of 0.5 inches (12.7 mm). The core was sandwiched between two face sheets manufactured from laminate plies with orientations of 0 and 90 degrees, while changing the number of plies for each trial. Table 6 below gives the number of plies, their respective orientations, surface preparation and impact energy for each trial.

Test Panel ID	Number of plies	Layup Orientation	Surface Preparation	Impactor	Impact Energy (J)	Impact Velocity (m/s)
Test Panel 2	5	[0/90/0/90/0]	Sand + Acetone	1	1.18	3.96
Test Panel 3	6	[0/90/0/90/0/90]	Sand + Acetone	1	1.18	3.96
Test Panel 4	7	[0/90/0/90/0/90/0]	Sand + Acetone	1	1.18	3.96
Test Panel 5	8	[0/90/0/90/0/90/0/90]	Sand + Acetone	1	1.18	3.96

Table 6: Properties of Test Panels 2-5, panel surface preparation and impact configuration for the core crush detection study.

For this study, the test panels were manufactured using the same techniques as outlined in Section 3.1. After the face sheets had cured, they were wet sanded using 120 grit sandpaper; this allows more surface area for the film adhesive to bond to, which prevented the face sheet disbonding from the core during the impact event. In Figure 41, image (a) shows the residual indentation with a green ring showing the diameter, while image (b) on the right shows the cross section of the dent and confirms that the predicted core crush extends out past the indicated surface indentation as expected [34].

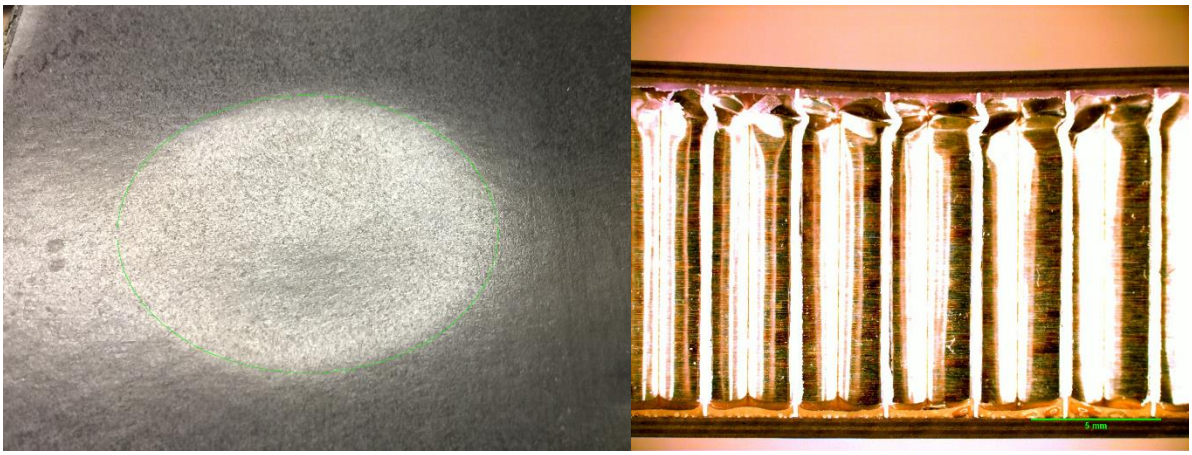

(a) (b)

Figure 41: Surface indentation for test Panel 2, Green circle is ~38 mm (5 Ply, [0/90/0/90/0]) (6.3x zoom) (Scale Bar = 1.0 mm)

After the honeycomb panels had been impacted they were scanned using a FAROARM 3D laser scanner. This type of laser scanner uses triangulation to determine the 3D geometry of the scanned surface with the scanning head attached to a 7-axis arm bolted to the work surface. The system has a single point repeatability of 0.024-0.064 mm, which means if a location is measured multiple times, it is expected to vary less than 0.064 mm across each of the measurements [19]. The scanning head projects a 150 mm line of dots on to the panel surface which is called the beam width or stripe width. The line is a series of dots called a flying dot arrangement and everywhere that a dot is projected onto the surface is recorded as a 3D point cloud containing millions of data points per test panel scanned. A mesh fit was used to fill in the small gaps between the recorded information to turn the point cloud into a surface body. Once the deformed surface of the indented panel had been established, a deviation analysis was performed relative to the undamaged planar surface to extract the depths of each of the impact locations. An example of a 3D scanned impact location is shown in Figure 42 (a), which displays a series of isolines at set intervals for the impact depth. The green surrounding the impact is considered to be the undamaged surface of the face sheet to within 0.01 mm.

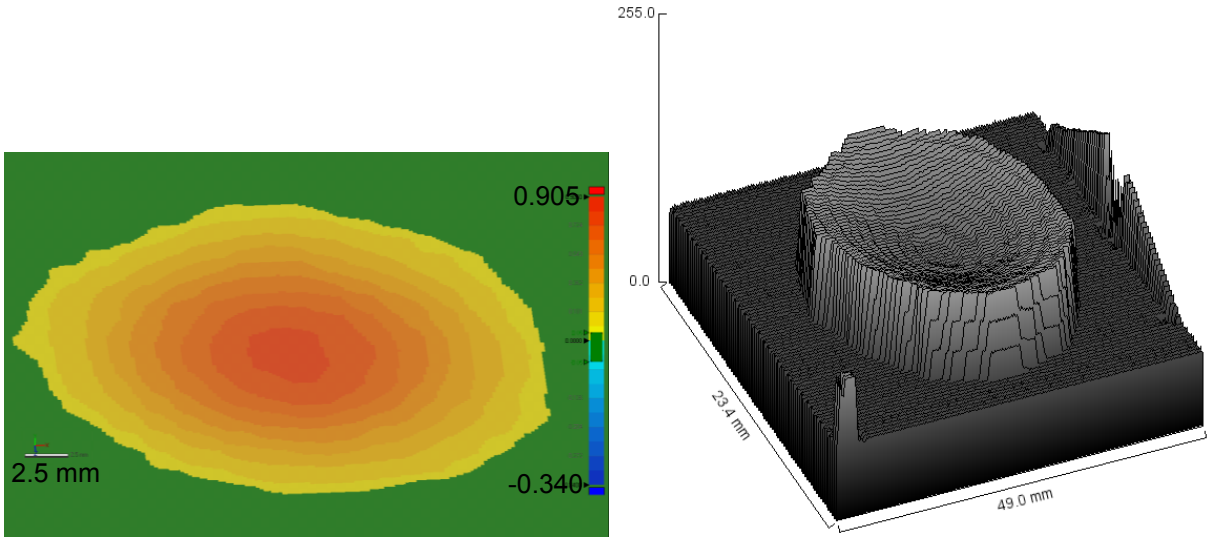

(a) (b)

Figure 42: Test Panel 2 (5 Ply [0/90/0/90/0]) (a) Deviation analysis showing dent depth. (b) Exaggerated 3D contour plot showing dent profile (Viewing angle of 45°, (Scale Bar = 2.5 mm)

An example of a 3D scanned face sheet is shown in Figure 43, where the green surface is a mesh fit applied to the surface of the face sheet and allows a deviation of 0.05 mm. This deviation value was used for each of the scanned face sheets and provides a clearly defined impact diameter $2R_{ind}$.

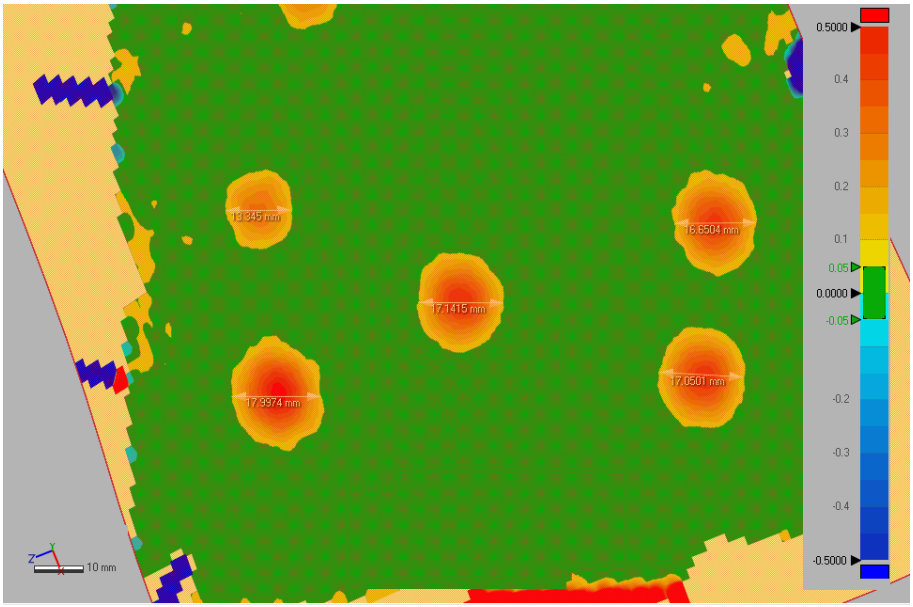

Figure 43: Test Panel 2 (5 Ply, [0/90/0/90/0]) Deviation analysis displaying measured depths and diameters ($2R_{ind}$) for five impact locations (units are in mm) (Scale Bar = 10.0 mm).

The average dent depths for each of the 5, 6, 7 and 8 ply test panels are shown below in Figure 44. The error bars indicate the average of the dent depths for the 6 repeats performed for each face sheet thickness.

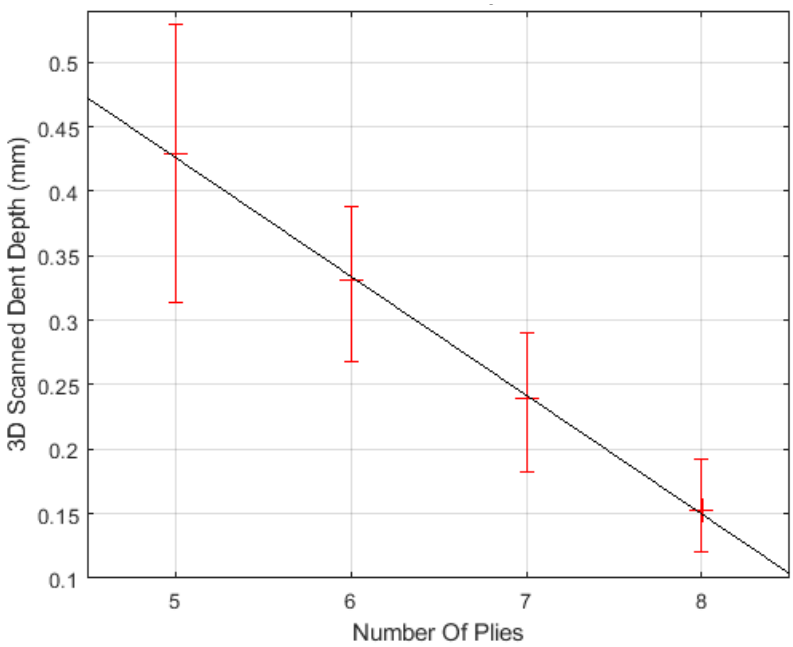

Figure 44: 3D Laser scanned impact depths for test panels 2-5 with an Impact energy of 1.18 J

As the number of plies was increased in increments of 1.52 mm (0.006 inch) in thickness, the residual indentation depth decreased linearly. This was expected, as increasing the number of plies in a layup increases the face sheet's overall stiffness. This relationship is also displayed in Figure 45 for the impact location's measured diameter. The diameter of the measured impact also displayed a linearly decreasing value as the number of plies was increased in a layup. The larger error bars represent the minimum and maximum measured diameters and are due to the irregularity in the shape of the impact locations, which is believed to be linked to the honeycomb core's ribbon direction.

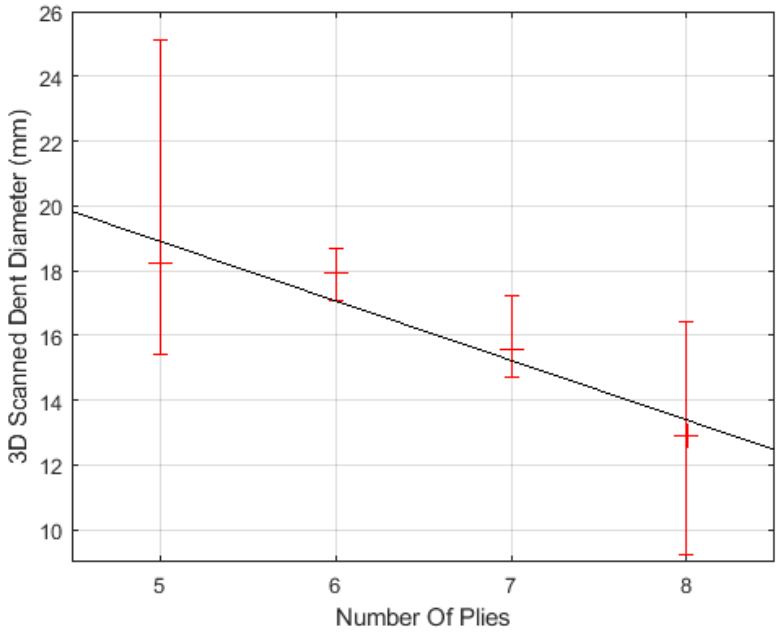

Figure 45: 3D Laser scanned impact diameters for test panels 2-5 with an Impact energy of 1.18 J.

After 3D scanning test panels 2-5, they were scanned using IR thermography to determine if the core crush was visible in a thermal image. IR thermography was not able to detect core crush, due to the face sheet remaining adhered to the film adhesive and honeycomb core. The thermal energy was able to pass through the face sheet, film adhesive and into the honeycomb core without being obstructed by a small void. It was found that if the top cell walls of the honeycomb core remained adhered to the film adhesive and none of the fillets became unbonded, IR thermography was not able to display the small creases that now exist in the cell walls after the impact due to the thermal energy still being able to pass through. Figure 46 (a) shows test panel 2 with 6 indents circled in green. Figure 46 (b) shows the IR image taken of test panel 2, where neither the indents nor the core crush are visible. The flat brown paint was applied to the face sheet to increase the surfaces emissivity value, this however did not help with the detection of core crush.

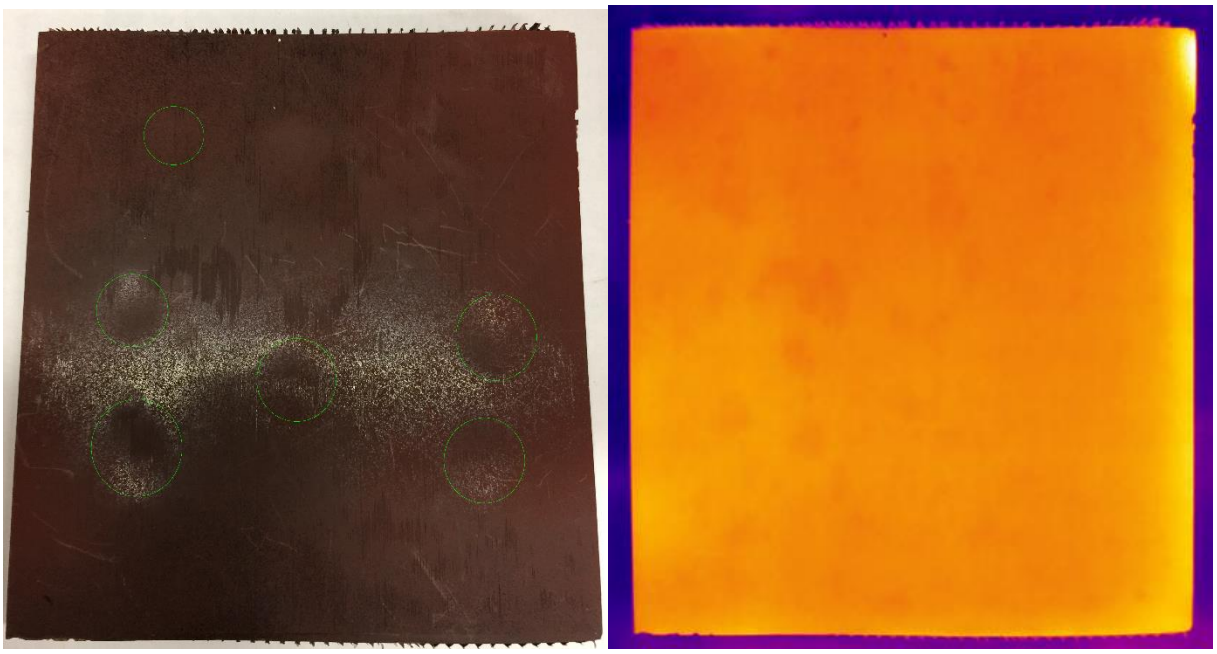

(a) (b)

Figure 46: Test Panel 2 (5 Ply, [0/90/0/90/0]) Impactor 1, Impact energy of 1.18 J. Visual Image (a) IR thermal image (b).

4.2 Detecting a disbond between the face sheet and core

The purpose of this study was to determine if IR thermography is capable of detecting and measuring the diameter of a face sheet to film adhesive disbond. A range of disbond diameters were created by impacting the face sheet with energies between 0.29-1.47 J, while keeping the impactor size and face sheet layup constant throughout all the trials. Disbonds were created by not wet sanding the face sheets prior to bonding to the core. The smooth surface finish of the face sheet resulted in a poor bond with the honeycomb core and produced a disbond rather than residual indentation. The face sheet was able to relax back to its original position after the impact event, as an adequate amount of time was given for complete relaxation. No trace of damage to the face sheets surface was visible even though there was a disbond and core crush below the impact site. Results from Section 4.1 showed that IR thermography was not able to detect core crush; therefore in the current study, any damage visible through IR is from the small void that forms between the face sheet and the adhesive that remained attached to the core. In addition to IR thermography destructive inspection was used to measure the depth and diameter of core crush present. The values measured from the destructive cross section were compared to the values indicated by an IR thermography scan to establish a relationship between the indicated maximum temperature to core crush depth and temperature distribution to the disbond diameter. Figure 47 specifies the diameter of the indicated core damage ($2R_{ind}$) from a cross section cut and diameter of the disbonded face sheet from a thermogram ($2R_{disbond}$).

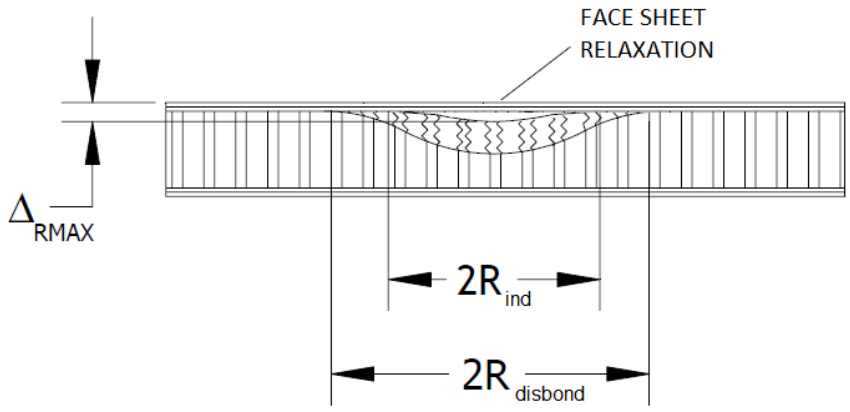

Figure 47: Residual indentation of the honeycomb core and width of the disbond indicated from thermography. The change in the face sheet depth is given by Δ_{RMAX} where the indicated core crush diameter is given by $2R_{ind}$ .The indicated disbond diameter is given by $2R_{disbond.}$[34].

The test panels manufactured for this study use a honeycomb core material of 5052-H34 aluminum, with a cell size of 0.125 inches (3.175 mm), a wall thickness of 0.007 inches (0.178 mm) with a height of 0.5 inches (12.7 mm). This was sandwiched between two face sheets, each manufactured using 5 plies of carbon fiber with a layup pattern of [0/90/0/90/0] and bonded using FM 300 film adhesive. A 5 ply layup was based on a realistic layup for an F/A-18 aircraft horizontal rear stabilizer rudder [13]. Impactor 1 was used for each of the trials, which has a mass of 0.15 kg and a diameter of 52.6 mm. The drop height started at 0.2 m and was increased by 0.1 m for each consecutive trial up to a final drop height of 1.0 m to create a range of disbond diameters. Table 7 provides the layup orientations, surface preparation and impact energies used for each of the nine trials, which consisted of one impact for each of the listed energies.

Test Panel ID	Number of plies	Layup Orientation	Surface Preparation	Impactor	Impact Energy (J)	Impact Velocity (m/s)
Test Panel 1	5	[0/90/0/90/0]	Acetone	1	0.29	1.98
Test Panel 1	5	[0/90/0/90/0]	Acetone	1	0.44	2.42
Test Panel 1	5	[0/90/0/90/0]	Acetone	1	0.59	2.80
Test Panel 1	5	[0/90/0/90/0]	Acetone	1	0.74	3.13
Test Panel 1	5	[0/90/0/90/0]	Acetone	1	0.88	3.43
Test Panel 1	5	[0/90/0/90/0]	Acetone	1	1.03	3.70
Test Panel 1	5	[0/90/0/90/0]	Acetone	1	1.18	3.96
Test Panel 1	5	[0/90/0/90/0]	Acetone	1	1.32	4.20
Test Panel 1	5	[0/90/0/90/0]	Acetone	1	1.47	4.43

Table 7: Properties of Test Panel 1, Layup, surface preparation, impact energies and velocities tested.

The presence of a disbond was identified by the face sheet relaxing and returning to its original pre-impact position. Relaxation of the face sheet can occur immediately or in some cases it took over a week to fully spring back. For example, the image in Figure 48 (a) was taken of a preliminary test panel immediately after an impact event using a 1.03 kg steel ball with an impact velocity of 2.45 m/s and an impact energy of 3.08 J which shows visible damage to the face sheet. The indentation remained for 270 seconds before the face sheet relaxed back to its original position as shown in Figure 48 (b). *Prior* [13] noted that spring back of a dented composite face sheet can be delayed and can slowly relax for over a week following the impact event due to the buildup of residual stress in the face sheet. However, for each of the impact energies, the film adhesive disbonded from the face sheet when the face sheet reached its maximum impact depth. The face sheet was able to relax back to its original position immediately compared to *Prior's* [13] situation where the face sheet remained adhered to the honeycomb core and took a number of minutes to relax back to its original position.

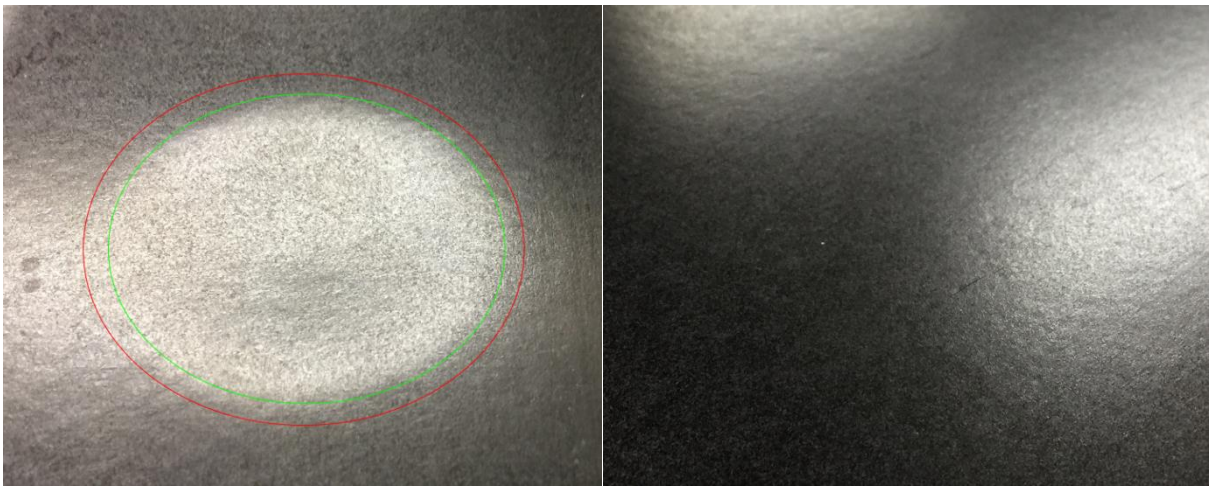

(a) (b)

Figure 48: Preliminary test panel. Impact energy of 3.08 J. (a) Indentation of the face sheet immediately after the impact event. (b) Relaxation of the face sheet occurring 270 s following the impact event which shows a flat face sheet. The green circle represents the indicated core crush diameter ($2R_{ind}$) while the red circle represents the IR thermography disbond diameter ($2R_{disbond}$). Green circle is ~38 mm, Red circle is ~40 mm.

A cross section image of Figure 48 (b) in Figure 49 below, shows the disbond that was created between the face sheet and the film adhesive after the face sheet has relaxed back to its

original position. The diameter of core crush appears larger than the diameter of the disbonded face sheet.

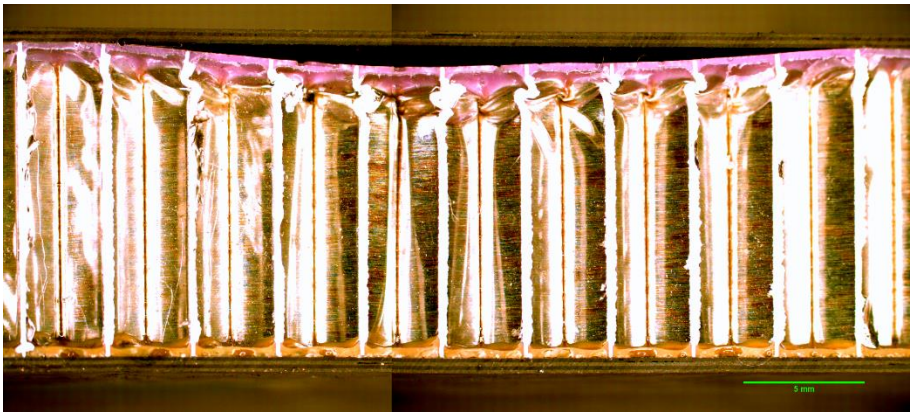

Figure 49: Preliminary test panel. Cross section of an impacted panel with the disbond between the face sheet and the adhesive clearly visible (6.3x zoom). (Scale Bar = 5.0 mm)

The temperature distribution across a disbond location like the one pictured in Figure 50 (a), takes on a Gaussian shape with the surface temperature at the direct center of the impact appearing the hottest and dropping in temperature as you travel further from the center to the outer circumference of the impact. This can be seen in a close up of an IR image with a hot white center (a) and the corresponding temperature profile with a Gaussian distribution overlay for the 1.32J impact in Figure 50 (b).

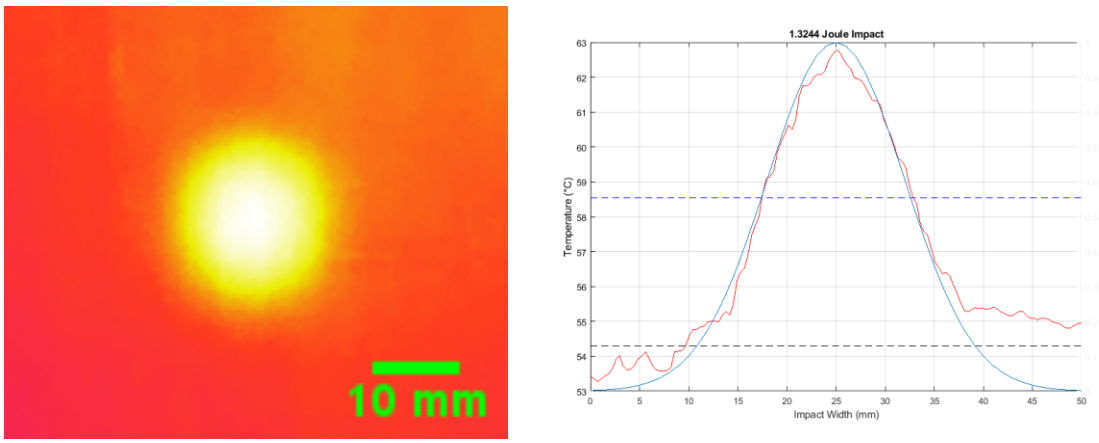

(a) (b)

Figure 50: Test Panel 1 (5 Ply, $[0/90/\bar{0}]_2$) 1.32J Impact. IR thermal image with Plateau Equalization algorithm applied (a) Temperature profile (b). The black dotted line is the average surface temperature.

The center of the impact has the most separation from the crushed film adhesive and honeycomb core and the amount of separation from the face sheet decreases to zero as you reach the circumference of the impact. Even though the film adhesive has become disbonded from the face sheet around the outer circumference of the impact, the gap between the face sheet and the film adhesive is very small and thermal energy is able to bridge the gap between them, which can lead to an inaccurate estimation of a disbond width. To estimate a disbond diameter using IR thermography, *Wysocka-Fotek's* [35] method of placing a temperature line profile over the impact location was used as shown in Figure 51. First the average surface temperature of a non-defective region was established and a base line is plotted (b). Starting from half of the defects height (a), a tangent line is plotted and intersected with the baseline temperature line for each side of the defect. The width in-between the two intersected lines is then taken as the defects width and this method was used to determine the defect width from the IR profiles in the current study.

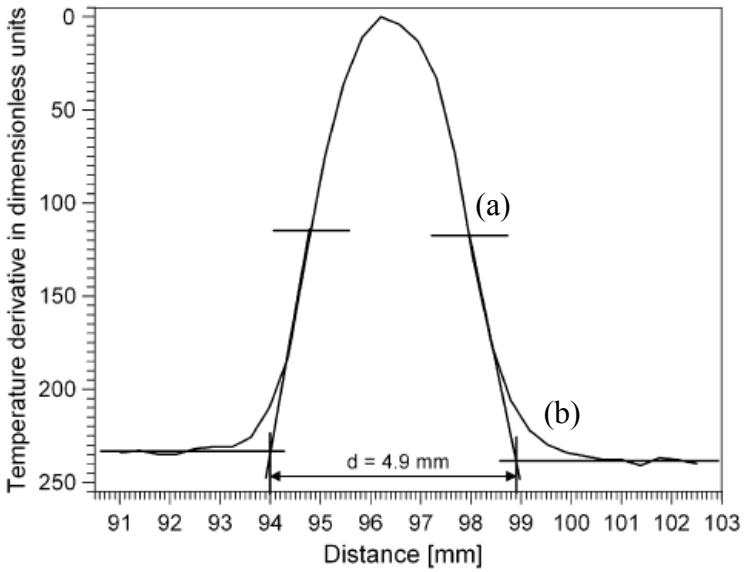

Figure 51: *Wysocka-Fotek's* method for measuring a defects width [35].

The diameter of the disbond region was determined visually using the cross-section (microscope) and using the IR temperature profile for each impact energy are shown in Table 8 following Figure 57. The disbond diameter measured from a thermal scan was always between 50 and 75% larger than those measured from the cross-section images.

4.2.1 Diameter of core crush and disbond

The IR image of the disbonded region, a graph of the temperature versus the location across the impact region and the cross-section of the impact region are shown in Figures 52-57 for impacts between 0.29 and 0.59J and between 1.03 and 1.32J respectively. These results represent a small and large disbond, and the images for the remaining impact locations may be found in Appendix A.

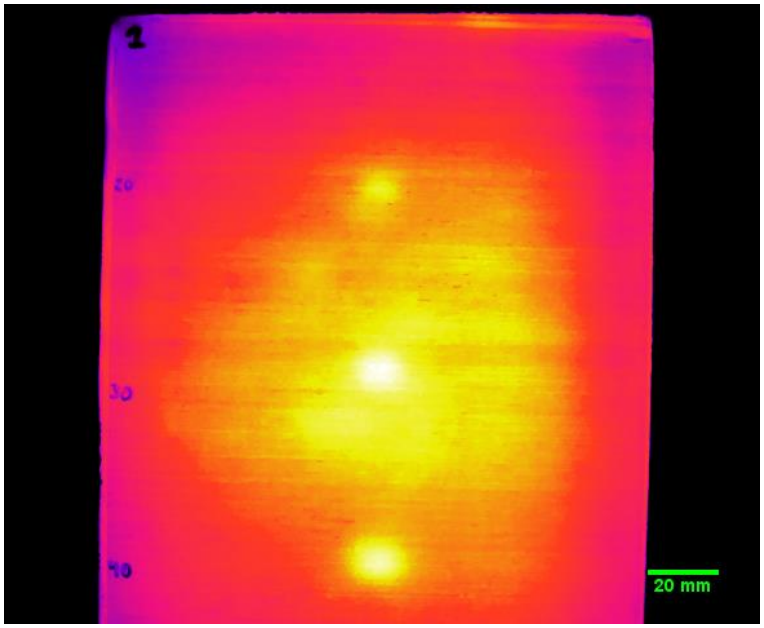

Figure 52: Test Panel 1 (5 Ply, [0/90/0/90/0]) IR image for three impact energies; 0.29, 0.44 and 0.59 J from top to bottom on the panel. Thermography Plateau Equalization applied.

The three impacted locations are displayed as bright hot spots when compared to the surrounding non-damaged face sheet. This indicates that a disbond has occurred, blocking the thermal energy from penetrating further into the honeycomb core. A temperature line profile was taken across the impact location's using FLIR's ResearchIR software. The temperature profile data was exported to Matlab, allowing the diameter of the disbond to be measured. This is shown in Figure 53, using the *Wysocka-Fotek's* method, with the black line representing the average surface temperature of the face sheet and the blue line representing the diameter at half of the peaks maximum temperature, with the two black tangent lines to measure the diameter.

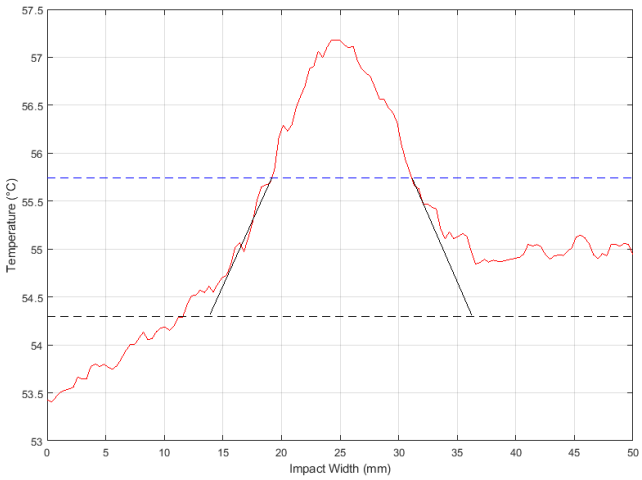

Figure 53: Test Panel 1 (5 Ply, [0/90/0/90/0]) Showing a graph of the temperature versus the location across the damage region for the 0.29J impact. Thermography measured diameter = 22.6 mm. The black dotted line is the average surface temperature, where the blue dotted line is half of the peaks height.

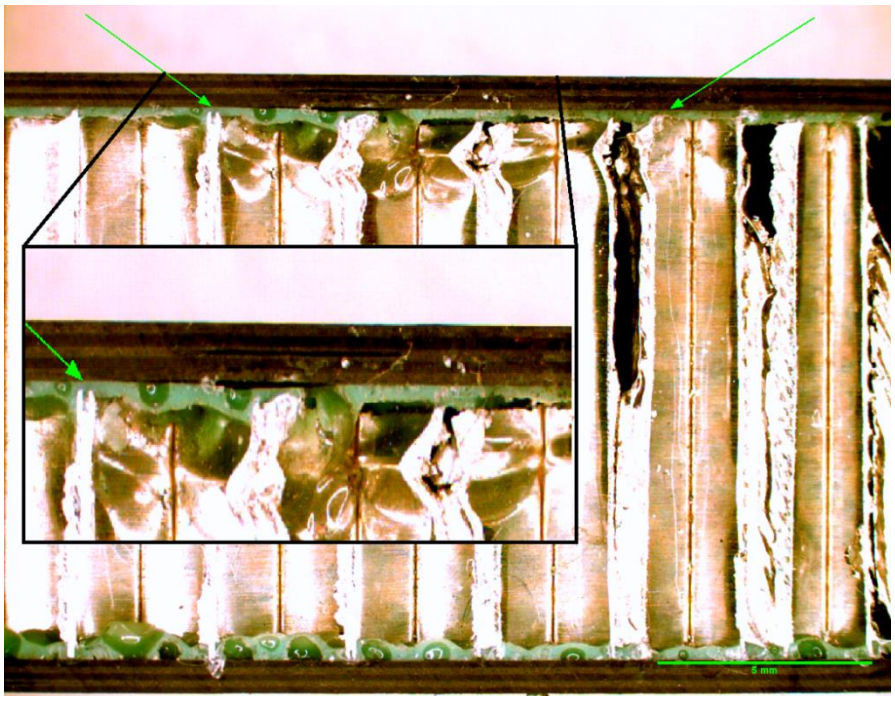

Figure 54: Test Panel 1 (5 Ply, [0/90/0/90/0]) Showing the cross-section of the damage region for the 0.29J impact. Microscope measured diameter = 10.6 mm, Microscope core crush depth = 0.09 mm. (6.3x zoom) (Scale Bar = 5.0 mm)

ImageJ is an image processing application which allows manipulation and spatial calibration of acquired images [36]. This program was used to measure the diameter of the disbond as well as the depth of core crush experienced. Once the magnification on the microscope had been set, a calibration slide was used in conjunction with ImageJ to set a scale on the images. The measured diameter of the disbond was visually the same as the diameter of core crush experienced. However, the diameter measured using IR thermography was over double the core crush diameter. This was first thought to be caused by not cross sectioning the impact location perfectly through the center, which would cause a smaller measured diameter using a microscope. The same results were reached after cross sectioning each of the impact locations. The measuring differences are discussed at the end of this study and are thought to be caused by lateral diffusion within the face sheet. The following image in Figure 55 shows three impact locations for energies of 1.03, 1.18 and 1.32 J. They each exhibit an increasing maximum temperature at the center of the impact location as the impact energy was also increased agreeing with Figure 52 above.

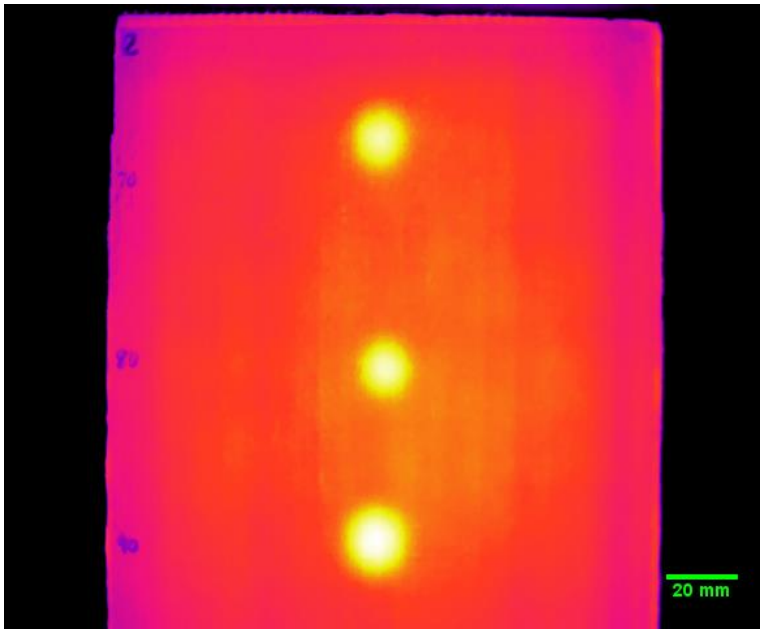

Figure 55: Test Panel 1 (5 Ply, [0/90/0/90/0]) IR image for three impact energies; 1.03, 1.18 and 1.32 J from top to bottom on the panel. Thermography Plateau Equalization applied.

The temperature line profile of the top 1.03 J impact location is shown in Figure 56; this impact energy was measured to have a maximum temperature of 61.7°C compared to the maximum temperature of 57.2°C reached from a 0.29 J impact.

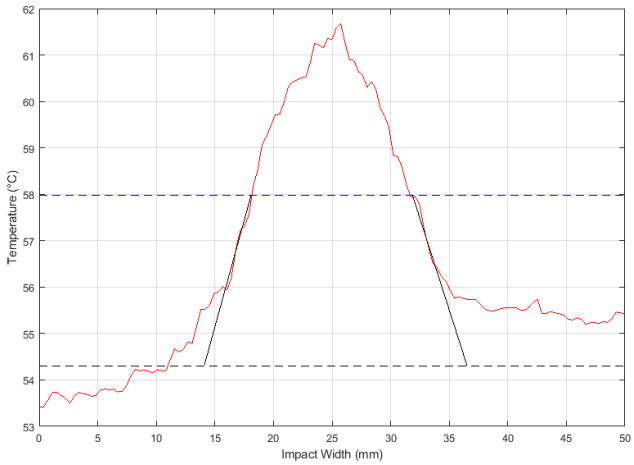

Figure 56: Test Panel 1 (5 Ply, [0/90/0/90/0]) Showing a graph of the temperature versus the location across the damage region for the 1.03 J impact. Thermography measured an impact width of 22.4 mm. The black dotted line is the average surface temperature, where the blue dotted line is half of the peaks height.

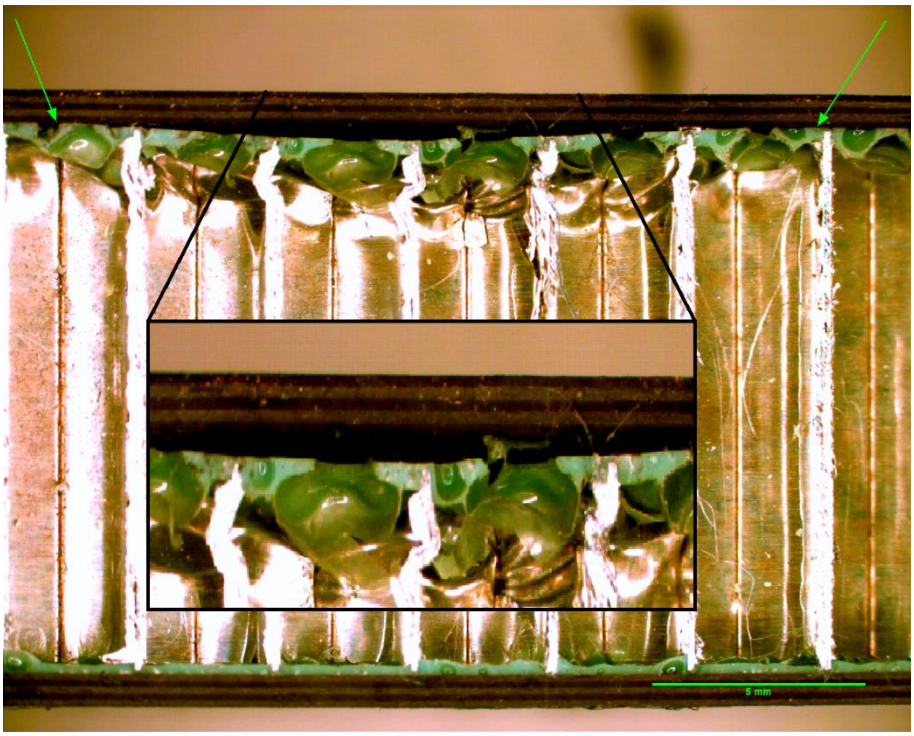

Figure 57: Test Panel 1 (5 Ply, [0/90/0/90/0]) Showing the cross-section of the damage region for the 1.030 J Impact. Microscope measured diameter = 17.6 mm, Microscope core crush depth = 0.43 mm. (6.3x zoom)(Scale Bar = 5.0 mm)

A larger 1.03 J impact energy resulted in a larger depth of core crush, while only marginally increasing the disbond diameter. It was first thought that the maximum temperature reached at the center of a disbond location was the result of a larger diameter disbond, but after looking at the slope of the measured diameter verses the impact energy and comparing that to the slope of maximum temperature verses the impact energy, the depth of core crush was determined to be a larger contributor to the maximum temperature achieved and not the disbond diameter. Table 8 provides the measured diameters for each of the impact energies, which are all between 50 and 75% larger for the IR thermography measured values.

Impact Energy (J)	Microscope Diameter (mm)	Thermography Diameter (mm)
0.29	10.6	22.6
0.44	12.9	21.2
0.59	14.8	22.1
0.74	15.3	25.8
0.88	17.4	23.2
1.03	17.6	22.4
1.18	14.9	19.6
1.32	18.5	25.3
1.47	18.8	27.4

Table 8: Measured values for each impact energy, displaying a 50-75% increase in IR thermography measured diameters over cross section values.

One possible explanation for the large diameters measured using IR thermography is due to visually having to establish the circumference of the disbond when measuring under microscope. At the very edge of the disbond, the gap in-between the film adhesive and face sheet becomes too small to identify in a cross-section image and may result in a smaller measurement value. IR thermography measured the disbond diameter and not the core crush diameter which is thought to be the circumference of the disbond from a cross section image. Figure 58 displays the visually identifiable disbond and compares it to the thermography measured disbond.

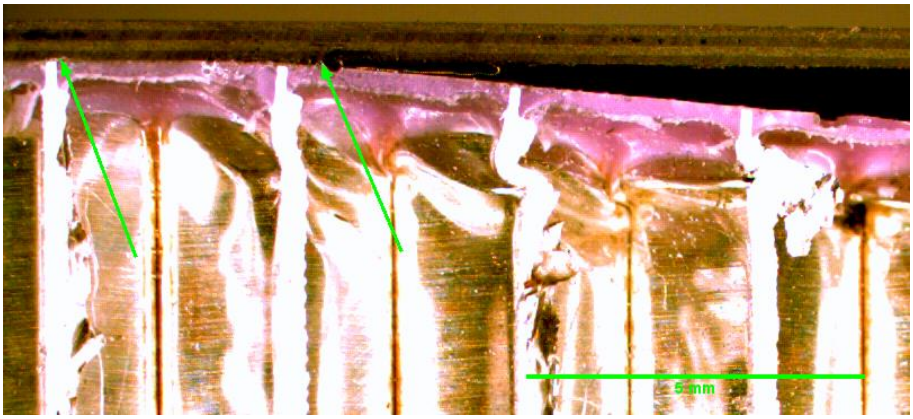

Figure 58: The left arrows shows where thermography indicated the disbond starts, where the right arrow shows where the disbond visually extends to. (6.3x zoom) (Scale Bar = 5.0 mm)

Figure 59 plots the disbond diameter versus the impact energy for each of the measurement methods. Eddy current scanning was also performed to validate the microscope measured values incase scaling or measurement errors existed. The values measured using eddy current scanning closely resemble the microscope measured width values and are plotted in Figure 59. Eddy current scan images are provided in Appendix A. A second analysis was conducted for the thermography measured widths using the Full Width Half Maximum (FWHM) approach, which are displayed in blue in Figure 59. This method uses a similar approach to the *Wysocka-Fotek's* method shown in Figure 51 by measuring from the half maximum value. The *Wysocka-Fotek's* method draws two tangent lines intersecting the half maximum values to the baseline temperature. The Full Width Half Maximum approach draws two vertical lines from the half maximum value directly to the baseline temperature. The width of the defect is measured between these two vertical lines and does not consider the tails of the distribution.

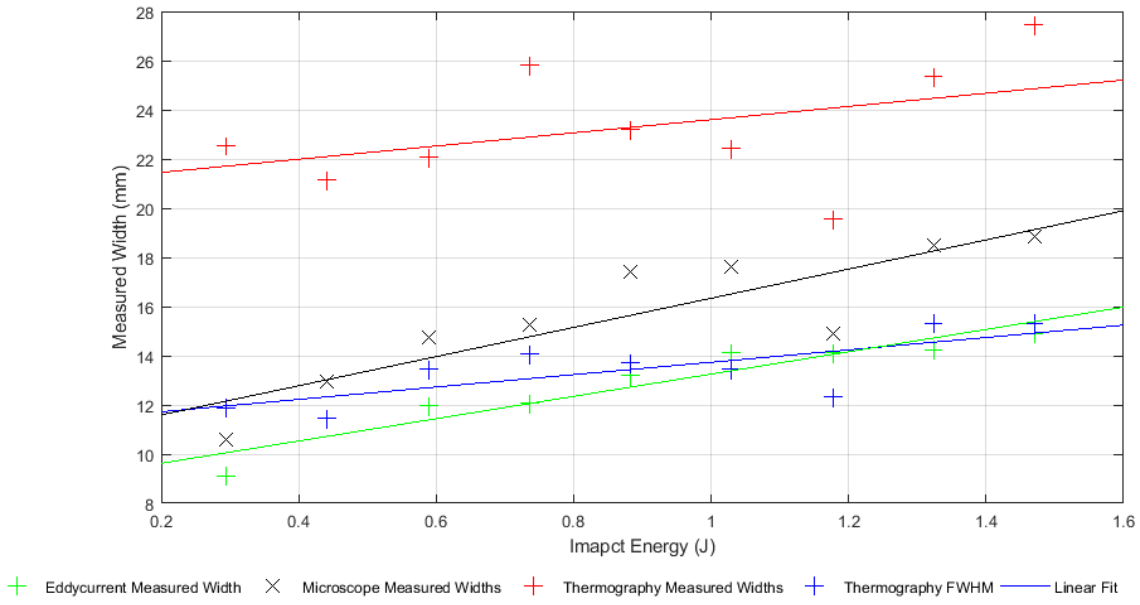

Figure 59: Disbond diameter versus impact energy for IR measurements and cross-section measurements. Thermography measured width (*Wysocka-Fotek's),* Thermography FWHM (Full Width Half Maximum method, -Appendix A).

After the analysis was completed using *Wysocka-Fotek's* method [35], the thermography measured diameters were all 50-75% larger than expected. The second analysis using the FWHM approach produced values that closely agreed with the eddy current results, but underestimated the width when compared to microscope measured values. Many have adapted the FWHM approach to provide a better fit to their results. A method by *Sharath, Menaka* and *Venkatraman* shown below in Equation 16, takes into account the thermal diffusivity and detection time, which accounts for lateral heat diffusion [38].

$$FWHM = D - 1.08\sqrt{(\alpha t)} \qquad 16$$

Where α is the face sheets thermal diffusivity and t is the detection time. Using this method, the measured width decreases in time, and measuring the width as soon as possible yields a better result. Others like *Avdelids, Gan, Ibarra-Castanedo* and *Maldague*, simply use a FWHM measurement [39], an example of this method is shown in Appendix A. As mentioned in Figure 58, the disbond might extend slightly further than visually indicated and depending on which type of defect and material are being measured, different measurement techniques should be considered.

The measured disbond diameter was proportionally larger as the impact energy was increased. The slopes for the impact energy verses diameter for each measuring method all exhibit a similar increasing slope. The IR thermography data points have some scatter, which could be due to surface imperfections or areas which contain imperfections within the face sheet. It was noted that the maximum temperature of a disbond location increased linearly with the impact energy, but after examining the slopes of each, the maximum temperature appeared to have a larger correlation to the depth of core crush and not as much to the disbond diameter discussed in Section 4.2.2. The depth of core crush is examined in the next section, which compares the maximum temperature measured using IR thermography with the amount of core crush measured using a microscope.

4.2.2 Depth of core crush

Figure 60 shows the temperature profiles across the damaged region for all impact energies. The maximum temperature for each of the damaged regions followed a linearly increasing trend shown in Figure 62, as the impact energy was increased. The dotted black line represents the non-defective region, which has an average surface temperature of 54.1°C. The temperature line profile directly above the dotted line displays the smallest 0.29 J impact, which has a maximum temperature of 57.2°C and is closely followed by the 0.44 J impact, which has a maximum temperature of 57.5 °C. This increasing relationship continues to the 1.47 J impact, which has a maximum temperature of 64.8°C and is expected to increase as the impact energy is further increased.

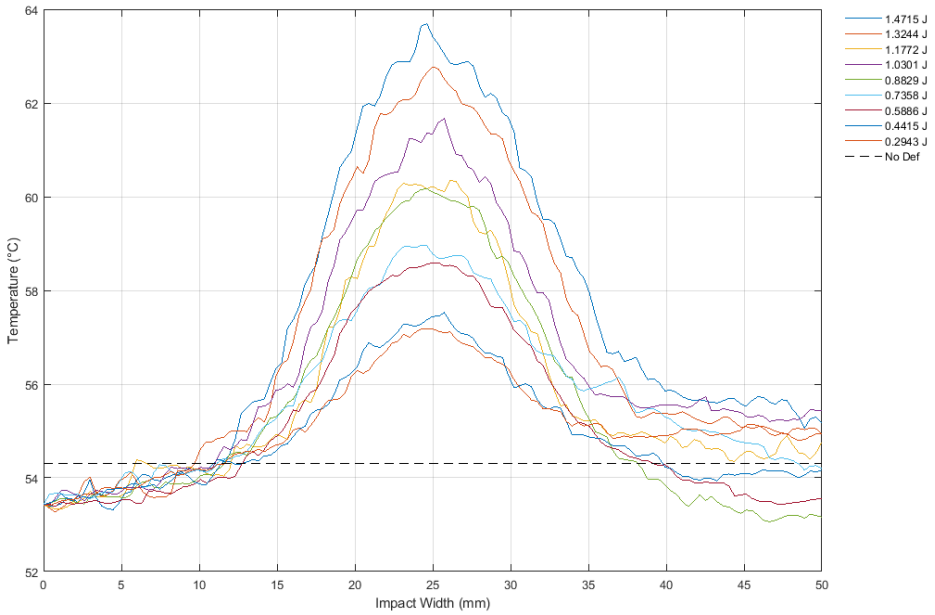

Figure 60: Test Panel 1 (5 Ply, [0/90/0/90/0]) Temperature line profiles for impacts 0.29-1.47 J. The black line represents the average surface temperature.

Table 9 displays the observed depth of core crush from a cross-section image as well as the maximum temperature within the damaged region from the IR thermography images for each impact energy.

Impact Energy (J)	Microscope Depth (mm)	Thermography Temperature (°C)
0.29	0.09	57.18
0.44	0.20	57.68
0.59	0.29	58.77
0.74	0.37	58.24
0.88	0.17	60.46
1.03	0.43	62.86
1.18	0.33	62.03
1.32	0.52	65.52
1.47	0.56	64.80

Table 9: Observed depth of core crush values for each impact energy.

The impact energy was increased 400% from 0.29 to 1.47 J, while the observed depth of core crush was measured to have an increase of 490% from 0.09 to 0.56 mm. The maximum temperature of the impact location increased 13% from 57.2 to 64.8°C as the impact energy was increased by 400%. Figure 61 displays a proportional relationship between the depth of core crush measured using a cross-sectional microscope image and the impact energy. As shown in Section 4.1, where the face sheet remained adhered to the honeycomb core, a larger impact energy resulted in a larger depth of core crush. This study follows the same trend, where increasing the impact energy resulted in a larger air gap in-between the face sheet and film adhesive once the face sheet had relaxed back to its original shape.

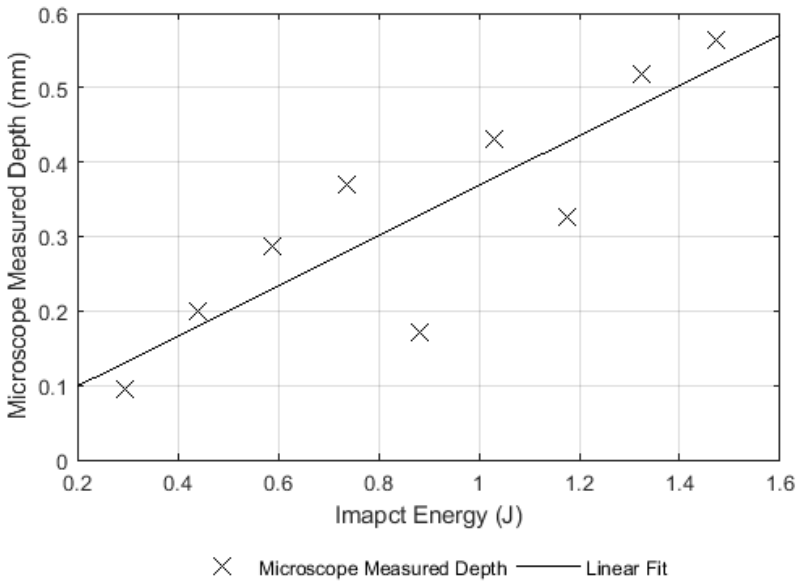

Figure 61: Microscope measured depth of core crush.

The first outlier in Figure 61 represents the 0.88 J Impact and is discussed in further detail below. This was due to the film adhesive not completely disbonding from the face sheet, which did not allow a correct measurement of the depth of core crush. The remaining impact energies displayed a linearly increasing depth of core crush as the impact energy was increased. The maximum temperature recorded for each impact location also displayed this same trend, as shown in Figure 62.

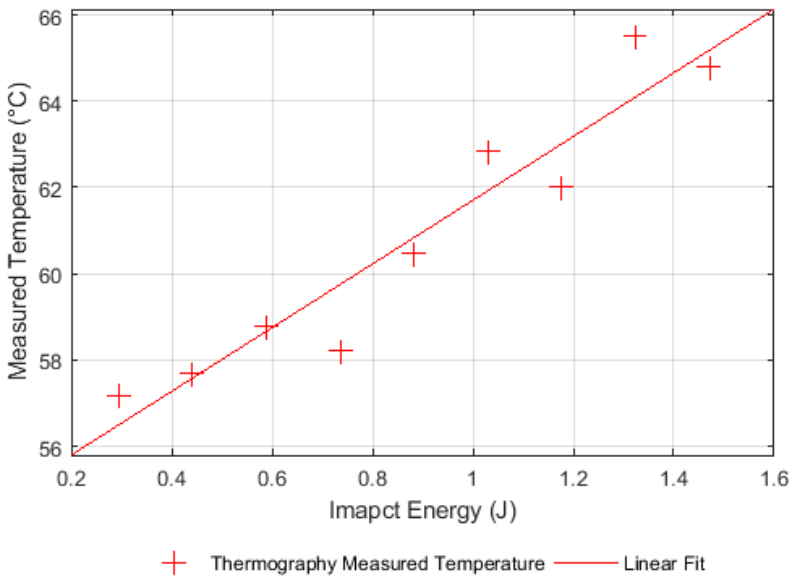

Figure 62: Thermography measured maximum temperature for each of the nine impact energies.

The maximum temperature for each impact energy is plotted against the microscope measured depth of core crush and is shown in Figure 63. This again displays a linearly increasing trend with the exception of the 0.88 J impact energy (Green), which remains an outlier.

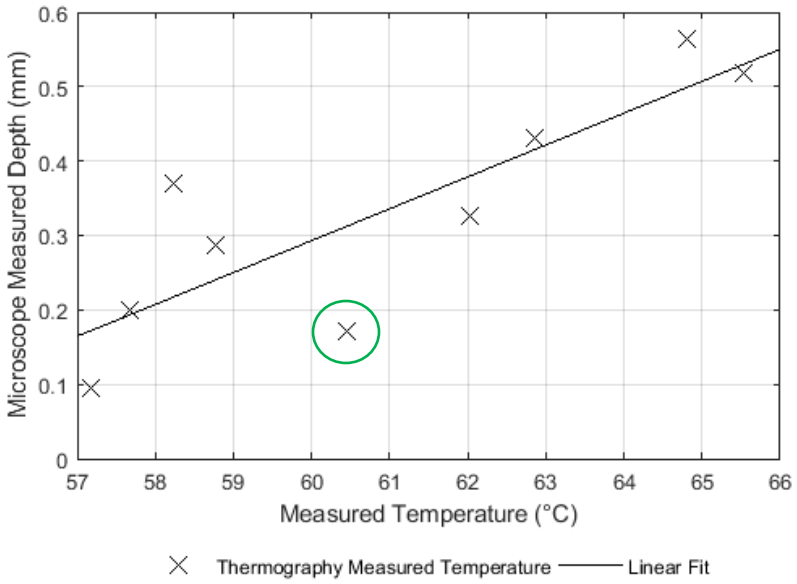

Figure 63: Thermography measured maximum temperature verses microscope core crush depth.

It was thought that a larger impact energy would produce a disbond region with a larger diameter, resulting in a higher maximum temperature due to the Gaussian distribution. It was found that the Gaussian distribution increased in height at a faster rate than it did in width. This is thought to happen due to thermal energy building up in the small air gap created under the face sheet. A larger impact energy resulted in a larger depth of core crush, which in turn created a larger air gap than a smaller impact energy. The larger air gap is able store more thermal energy before it penetrates further into the test panel, resulting in a higher maximum temperature for a larger impact energy.

4.2.3 Measurements errors

Some of the scatter in the depth of core crush measurements in Figure 61 can be attributed to variations in the bond strength between the film adhesive and the face sheet. The strength of the film adhesive bond can fluctuate in-between different face sheets as well as different regions on the same face sheet. The sanded or non-sanded surface finish and foreign contaminates may differ across each of the face sheets, which can lead to a distribution of energies needed to disbond the face sheet from the film adhesive. The 0.88 J impact location did not completely disbond from the face sheet, which resulted in a smaller disbond depth in-between the face sheet and film adhesive as shown in Figure 64 and Figure 65. The film adhesive around the outer circumference of the impact location has become disbonded from the face sheet, while the film adhesive at the center of the impact location remains bonded. When this happens, the film adhesive is not able to pull the crumpled honeycomb back to its original position before the impact and becomes unbonded from the cell walls. However, if the distance from the bottom side of the face sheet to the top of the honeycomb core is measured, it does not follow the linear relationship established by the other impacts. The measured depth of core crush of 0.57 mm would make this impact energy have a larger amount of core crush than the 1.47 J Impact event which had a measured core crush of 0.56 mm. This may suggest that the face sheet is able to slightly pull the film adhesive and honeycomb core up from its maximum crush depth before the face sheet becomes disbonded from the film adhesive and relaxes back to its original position.

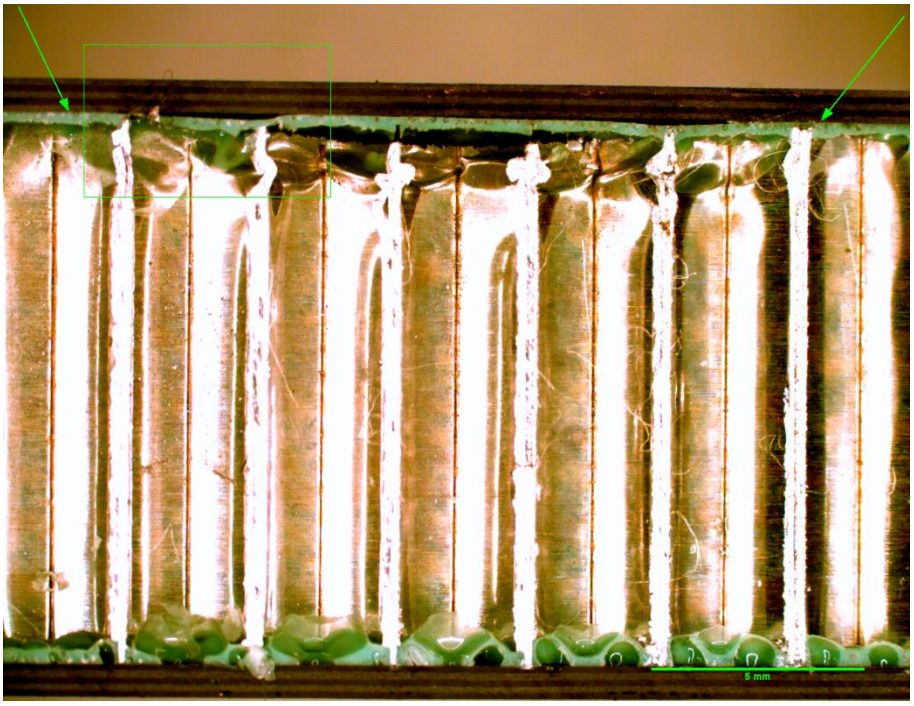

Figure 64: Test Panel 1 (5 Ply, [0/90/0/90/0]) Impact energy of 0.88 J. The green arrows point to where the disbond visually starts and the green box is looked at in more detail in Figure 65. (6.3x zoom) (Scale Bar = 5.0 mm)

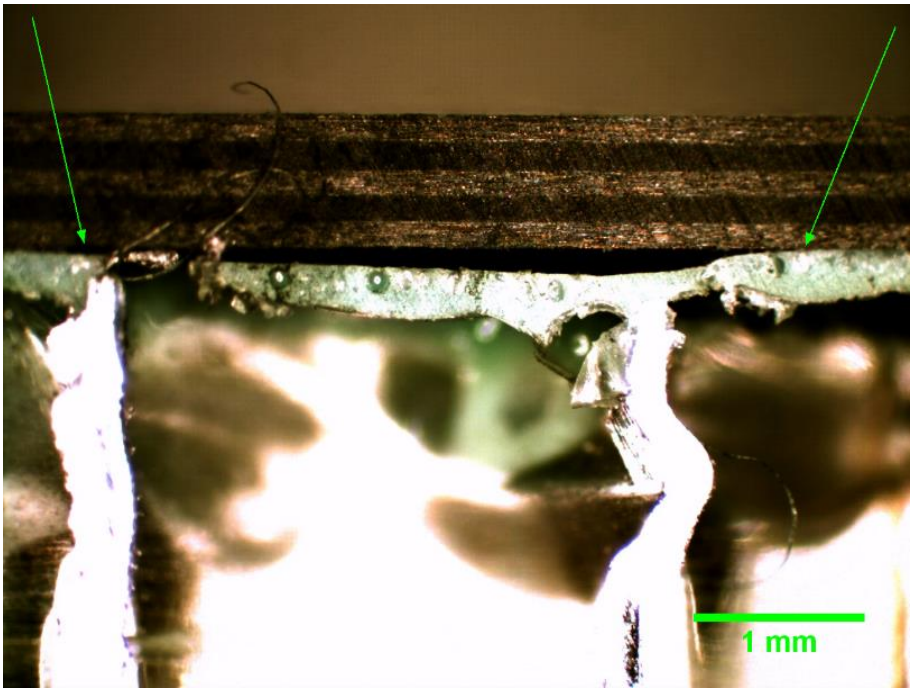

Figure 65: Test Panel 1 (5 Ply, [0/90/0/90/0]) Impact energy of 0.88 J. The green arrows point to where the disbond visually starts with the right side staying adhered (center of impact). (40x zoom)

When viewing a thermogram of this type of damage, the size and depth of the damaged area can be misinterpreted as it appears smaller and has a cooler temperature than an impact where the film adhesive has become completely disbonded from the face sheet. It is a very subtle difference in temperature change when the film adhesive remains adhered to the face sheet. This is compared in Section 4.5, where a ~1°C difference is observed between the two cases. A closer view of the honeycomb core becoming unbonded from the film adhesive is shown in Figure 66. The film adhesive has cracked at the bonding location, allowing the honeycomb core to stay compressed, while the face sheet and sections of the film adhesive have relaxed back to their original position before the impact event.

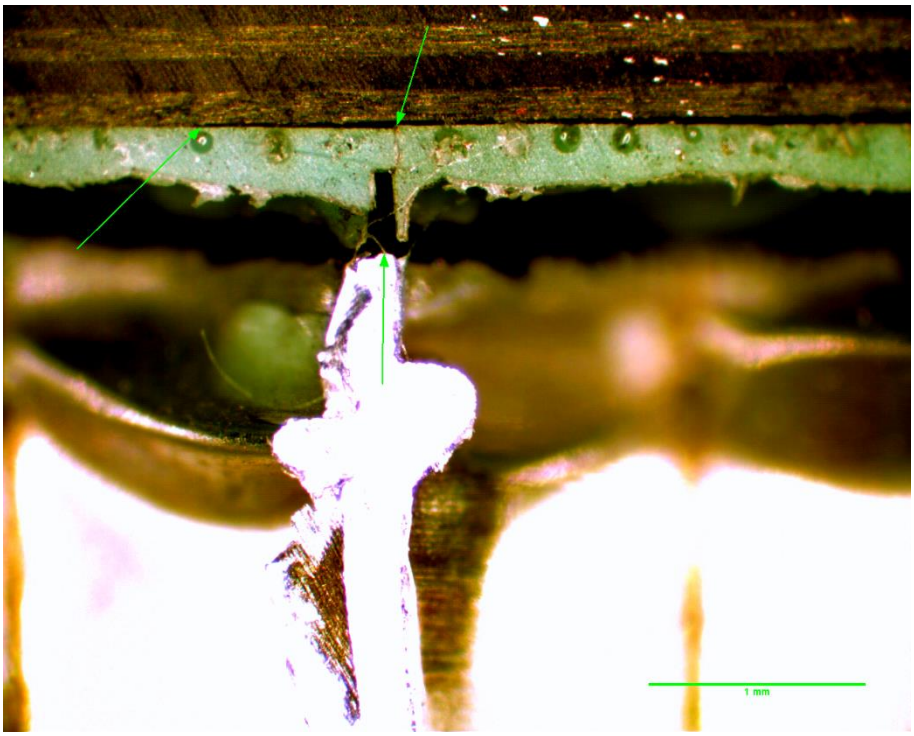

Figure 66: Test Panel 1 (5 Ply, [0/90/0/90/0]) Impact energy of 0.88 J. The green arrows point to where the film adhesive has cracked and has become unbonded from the cell wall allowing the core to remain depressed while face sheet and film adhesive relax back to their original position. (40x zoom) (Scale Bar = 1.0 mm)

4.2.4 IR Thermography examination errors

The diameter of a disbond was measured using *Wysocka-Fotek's* method [35], which relies on placing tangent lines from half of the temperature peak height to the average surface temperature. Because the center of the impact location was estimated, the temperature line profile may vary by a number of pixels. This measured diameter may be different than the cross section diameter measured using a microscope and leads to inconsistencies when comparing the two measuring techniques. This method also relies on setting an average surface temperature within the plot, which may be a few fractions of a degree off depending on the impact regions location under the halogen heating bulbs.

4.2.5 Destructive examination errors

A rotary wet-saw with a 200 mm diamond blade was used to section each of the test panels in order to view the cross section of each of the impact locations. However errors arise when attempting to section the impact locations perfectly through their center.

1. The location of the impact needs to be marked while viewing the test panel through an IR camera. Placing the mark in the direct center of the impact location relies on human judgement and may differ by 1-3 mm. As the impact locations ranged in width, if the mark is placed a couple mm from the center, the measured diameter and depth of the damage will not be an accurate representation of the original damage.

2. The rotary wet-saw uses a diamond blade that has a cutting width of 0.66 mm, which in turn removes 0.66 mm worth of material while sectioning the impact location.

3. When sectioning the impact locations, the cut was performed off-center to avoid removing material from the deepest part of the dented area. However this relates back to uncertainty number one, if the initial mark was placed off-center, then the cut location would also be off-center and the cross section would not be an accurate representation of the damage.

The cross sections were then examined under a microscope at 6.3x zoom. ImageJ software was used to measure the maximum depth in which the face sheet, film adhesive and honeycomb core were compressed to. The software requires human judgement to measure the gap and errors will arise if the measuring points vary by a number of pixels. Figure 67 shows an example of how not correctly marking the center results in a smaller measured width. The radius of the impact is given by r and the distance from the center to the cut edge is given by d. As mentioned in Section 3.3.5, it is difficult to mark where the exact center of a disbond location is. Take for example, the actual disbond width is 14 mm, if the indicated center mark varies by 1.5 mm and the blade width is 0.66 mm, then the measured width would be 13.3 mm.

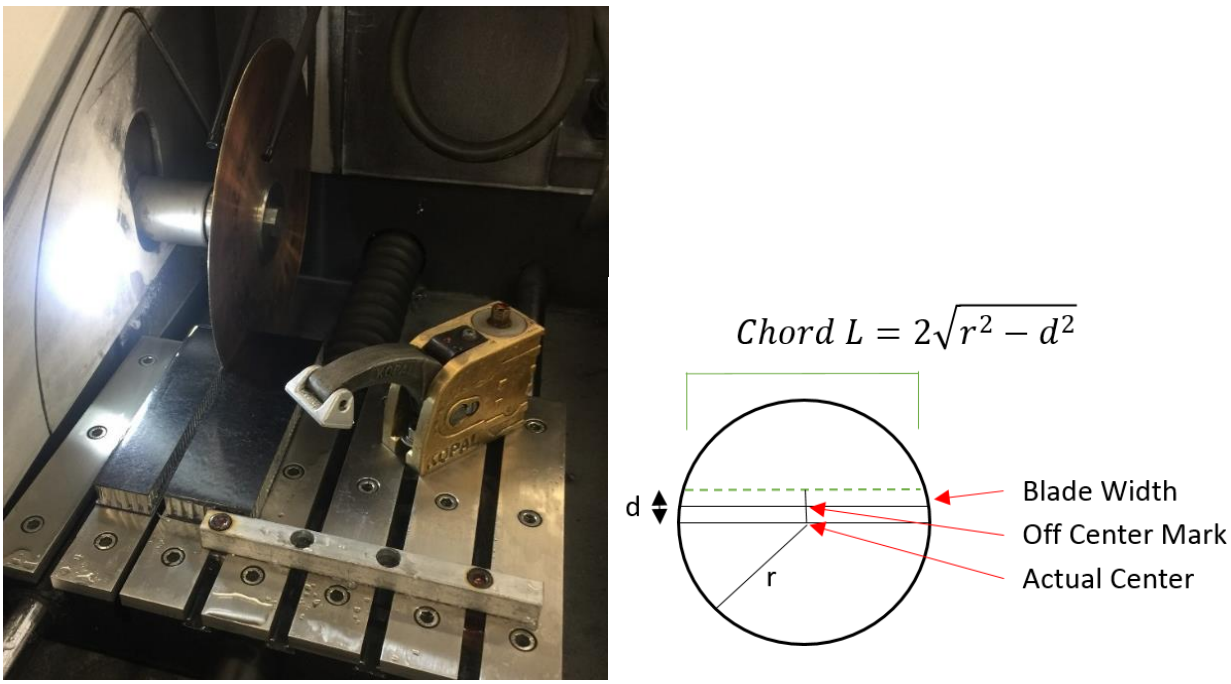

(a) (b)

Figure 67: Rotary wet-saw used for cross sectioning the impact locations (a), Chord length for an off enter cross section cut (b).

When combining the microscope measuring errors as well as the thermography measuring errors, it is expected that a 5-10% total measuring error exists for the reported values.

4.3 Detecting flaws at different depths

The previous two studies have focused on damage occurring to the honeycomb core and whether IR thermography was capable of detecting it. This study focused on defects occurring within the composite face sheet and if IR thermography was capable of determining the depth of the void based on its thermal signature and detection time. An existing standard thick face sheet composed of 84 plies of carbon fiber was used for this study; the face sheet contained 12.4 mm (0.5 inch) diameter flat bottom holes drilled to different depths, leaving incremental amounts of carbon fiber left. This is shown in Figure 68 with the front face of the test panel shown on the left (a) and the drilled out backside of the panel shown on the right (b). The left row of holes was considered for this study, which includes holes with 0.01-0.1 inches (0.254-2.54 mm) worth of carbon fiber left.

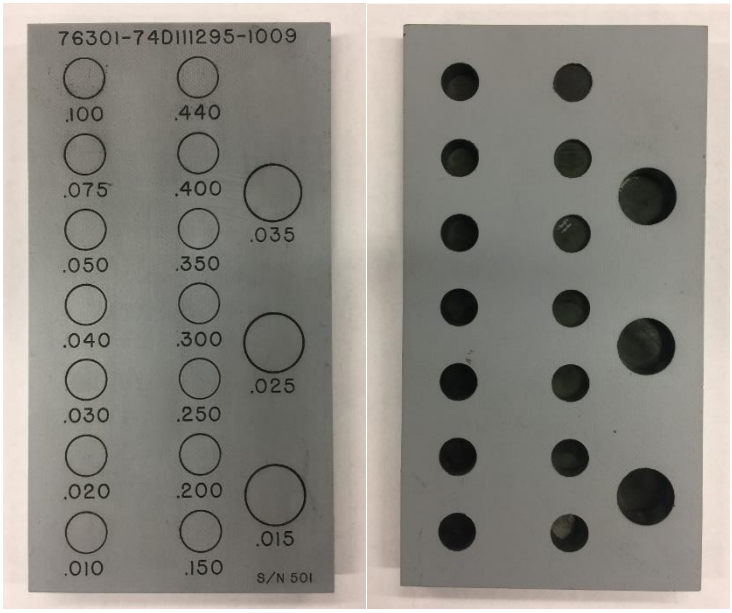

(a) (b)

Figure 68: Test Panel 6 (84 Ply, $[0/90/-45/+45/90/0]_{14}$) Front face (a) and bottom face with flat bottom holes drilled (mirrored image)(b). Units are in inches.

The incremental holes simulate delaminations or voids occurring within the face sheet of a standard honeycomb test panel. When a delamination occurs, a small air pocket is formed, creating a discontinuity, which disrupts the thermal energy from penetrating further into the test panel. The values represent the amount of carbon fiber left after drilling the hole and not the depth of the hole.

Thermal energy was applied to the front face of the test panel and each of the drilled out locations was monitored over a number of minutes to establish a relationship between the discontinuities' depth and the monitored temperature. It was found that deeper defects required a longer heating period, as the thermal energy dissipates within the carbon fiber and is not able to reach the deeper voids. Contrary to this, heating the face sheet for an extended period of time over saturated the surface and shallower voids. A heating period of 3 seconds was chosen for depths up to 2.54 mm (0.1 inch) deep. Figure 69 shows the acquired thermogram of the test panel immediately after the heat was shut off. The temperature profile across each of the defects is shown below it in Figure 70 and displays a linear relationship between the peak temperature and the known defects depth. However, it does not provide any information about an unknown defects depth and further analysis is required to determine this information.

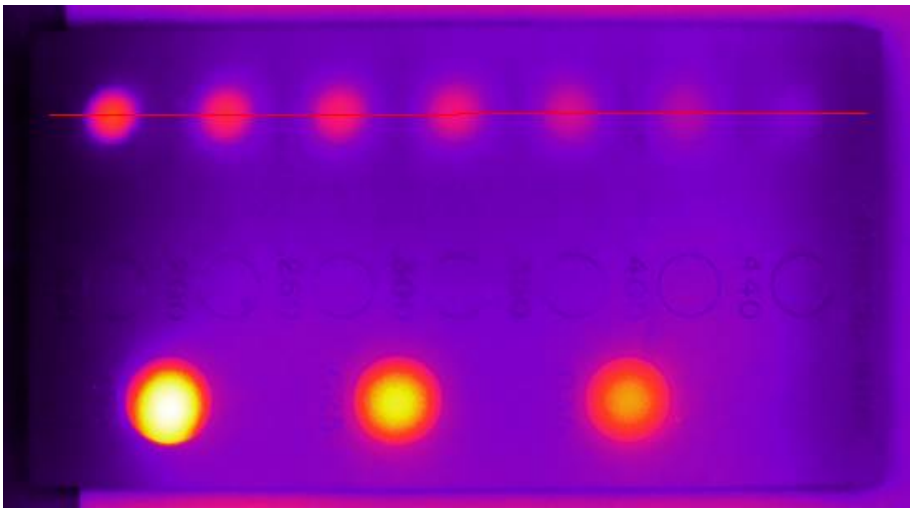

Figure 69: Test Panel 6 (84 Ply, $[0/90/-45/+45/90/0]_{14}$) Front face with a line profile taken across the 0.01-0.1 inch (0.254-2.54 mm) holes. Plateau Equalization algorithm applied.

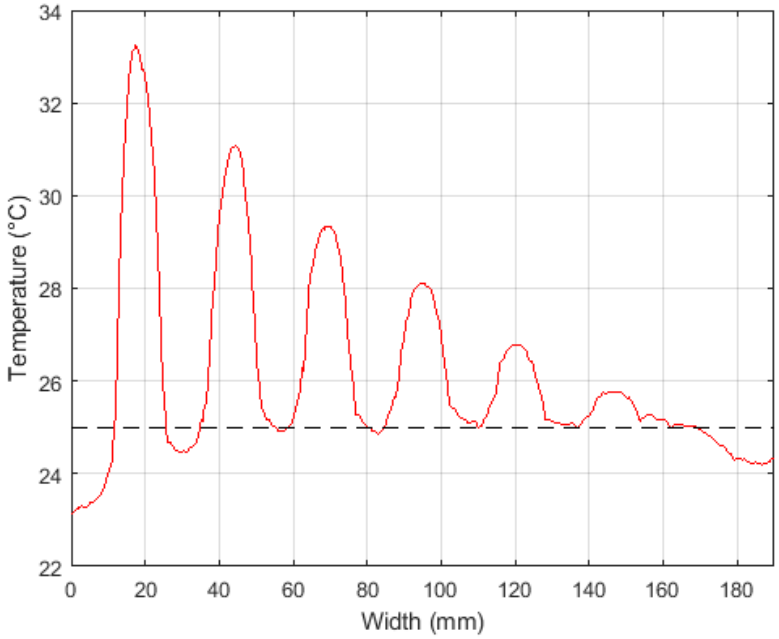

Figure 70: Test Panel 6 (84 Ply, $[0/90/-45/+45/90/0]_{14}$) Line profile taken across the 0.01-0.1 inch (0.254-2.54 mm) holes. With the hottest temperatures on the left side of the plot being the thinnest amount of face sheet (deepest hole).

As may be observed in Figure 70 above, the measured diameter of a defect appears to get larger as the depth is increased. The actual diameter of the hole is 12.4 mm and the IR thermography measured diameters started at 13. 6 mm for the shallowest 0.254 mm void and increased to 16.0 mm for the deepest 1.90 mm void. This is due to the thermal energy starting to disperse outwards into the face sheet and not directly down into the void as shown in Figure 71. Most research documents, including this one, rely on using the 1D heat diffusion equation as the face sheet is considered relatively thin. However these results suggest that using the 3D heat diffusion equation would provide a more accurate estimation of a defect's depth and width as the 3D equation. This takes into account lateral heat diffusion as the thermal energy dissipating in all directions and not just straight into the test panel.

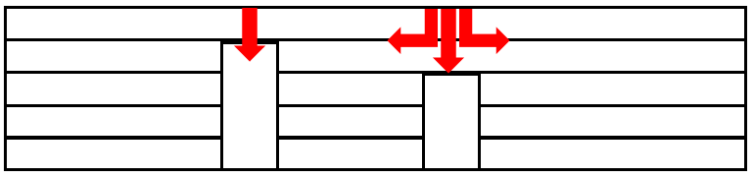

Figure 71: Thermal energy dispersing as depth increases.

To determine the depth at which the void was located, the panel's thermal contrast was monitored for a defective location as well as a non-defective location. The equation for Standard Thermal Contrast, shown in the image processing section by Equation 14 is again presented below.

$$C_{Std}(t) = \frac{T_{Def}(t) - T_{Def}(t_0)}{T_{SA}(t) - T_{SA}(t_0)} \tag{14}$$

Heat was applied to the front face of the test panel for 3 seconds and then immediately shut off, the temperature at each of the defective areas was monitored for 700 frames (@30 Hz), while the face sheet cooled off. The temperature profiles are presented in Figure 72 by a temperature verses frame number plot.

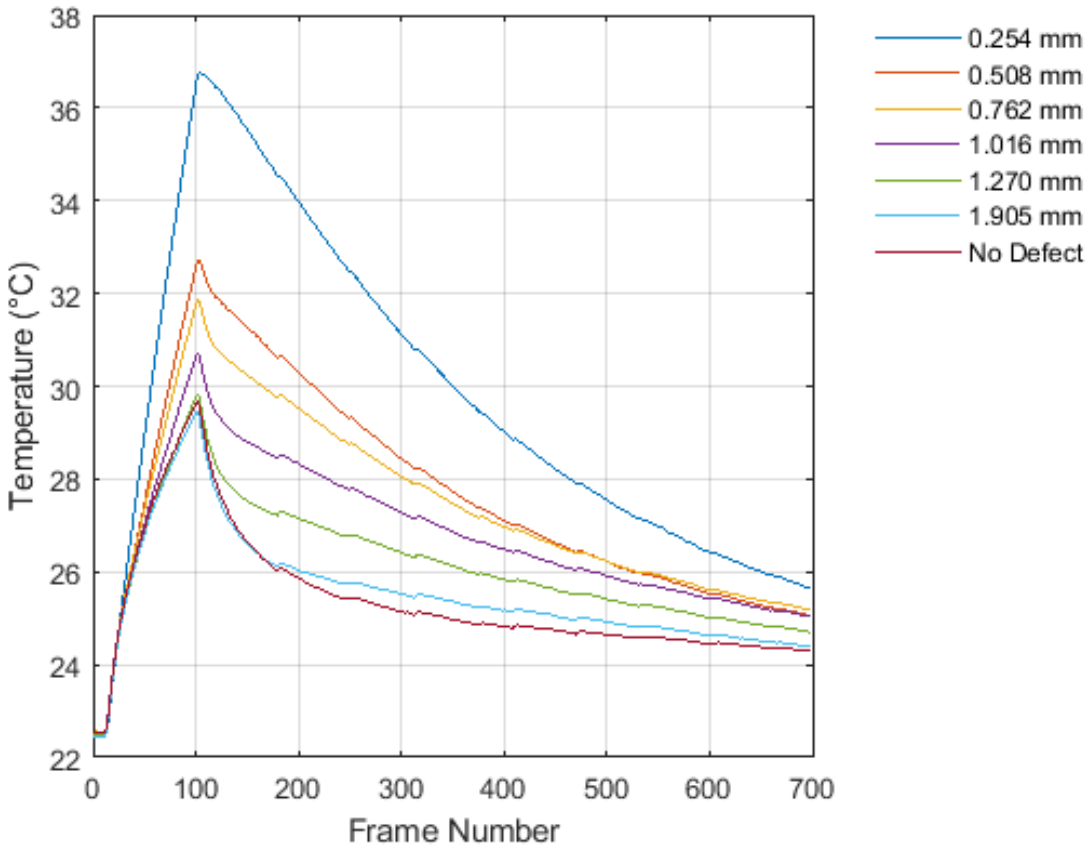

Figure 72: Test Panel 6 (84 Ply, $[0/90/-45/+45/90/0]_{14}$) Temperature vs frame number. Images were recorded at 30 frames per second for 20 minutes with a temperature reference marker at the center of each hole. The small bumps in the plot at frame numbers 180, 310 and 410 are due to the camera performing a sensor calibration.

It was shown that a location that does not contain a defect does not heat up as quickly and cools down rapidly as the heat is dispersed into the surrounding carbon fiber. In locations where the face sheet is thin, as in the 0.01 inch (0.254 mm) defect's location, the thermal energy is not able to penetrate further into the test panel and the face sheet heats up very rapidly. This location was not able to disperse the thermal energy as readily and remained at a higher temperature for a longer period of time. The time in which the defect reached its maximum thermal contrast was determined from the sequence of images and substituted into Equation 14 to determine the location's standard thermal contrast. The results are plotted and shown in Figure 73. The 'No Defect' temperature line profile is not included in Figure 73 as it is only used to determine the standard thermal contrast for the defect.

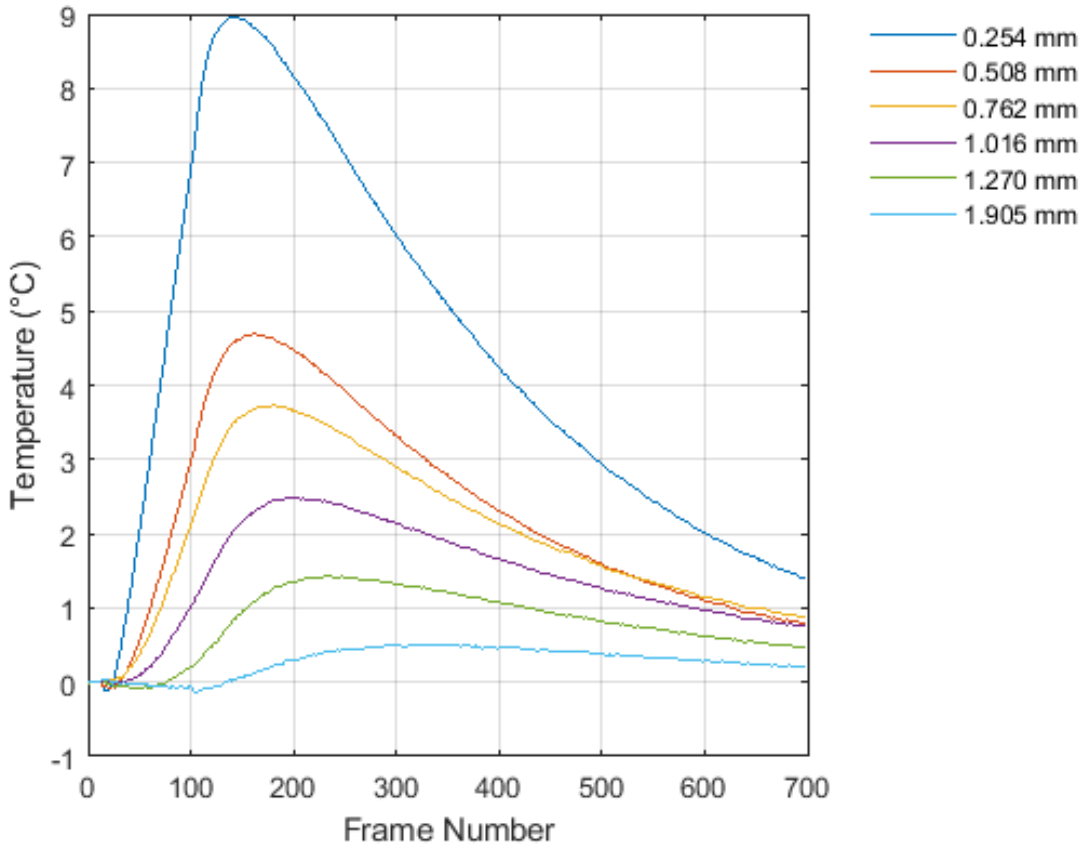

Figure 73: Test Panel 6 (84 Ply, $[0/90/-45/+45/90/0]_{14}$) Standard thermal contrast versus frame number. Images were recorded at 30 frames per second for 20 minutes with a temperature reference marker at the center of each hole.

With the defective areas standard thermal contrast now known, the results were plotted to establish a relationship between the time at which the maximum thermal contrast occurred and the defect's depth. This is shown in Figure 74, which displays a linearly increasing relationship between a defect's maximum thermal contrast time and the defect's depth within the test panel.

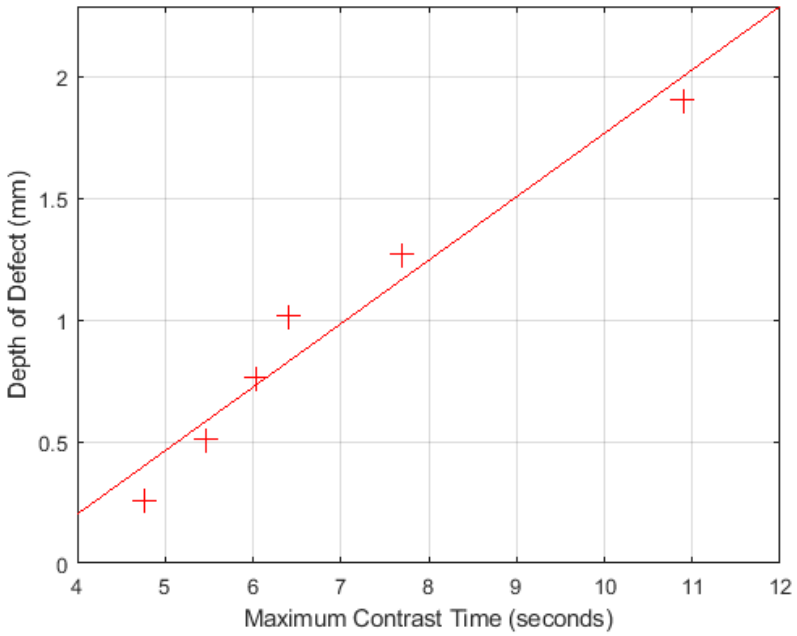

Figure 74: Test Panel 6 (84 Ply, $[0/90/-45/+45/90/0]_{14}$) Maximum thermal contrast verse frame number, showing that deeper voids are detected later in time and follow a linear relationship.

From these results, knowing that the depth of a void plotted against the time in which the void's maximum thermal contrast is reached allows one to predict an unknown defect's depth. In order to predict this, a reference test panel made from the same material, which has the same thermal properties as the panel being tested is needed. The test panel should have a series of reference depths, as the panel tested in this study to accurately estimate an unknown defect's depth from the surface. Having an IR camera that is capable of recording at a higher frame rate allows a closer approximation of the void's depth. The FLIR T620 used for this study has the slowest recommended 30 frames per second acquisition time for an analysis of this type. Recording with a newer IR camera such as a FLIR A6750sc, which has a frame rate of 4100 frames per second, would allow a closer approximation and would be able to pin point which ply the defect is in [36]. Taking into account the difference between the 1D heat diffusion equation and the 3D heat diffusion equation would also provide a more accurate value for the depth and diameter of

a defect. As the thermal energy is able to disperse outwards within the plies, the width appears larger in an IR thermography image than it actually is. The amount of dispersion would vary depending on what material the heat is being applied to, but does provide a source of error if not considered as in this case.

4.4 Detecting core separation

The purpose of this study was to test IR thermography's ability to detect damage occurring to the cell walls of the honeycomb core. The first study focused on detecting core crush from an impact event, where this study looks at detecting core damage from fatigue or thermal expansion causing shearing or ripping further into the core at the impact site. Damage occurring within the honeycomb core is not as obvious to spot as damage occurring to the tops of the cell walls. The applied thermal energy needs to penetrate further into the test panel without being obstructed by a defect in the face sheet and into the vertical walls of the honeycomb cells. As the walls of the cells are only 0.178 mm thick, the IR thermal camera needs to detect the small temperature difference if there is a discontinuity within a cell wall. Having multiple camera lenses is useful and allows a closer look at the cell walls, as opposed to a wider field of view required when looking for defects in the face sheet.

The test panel manufactured for this study uses a honeycomb core material of 5052-H34 aluminum, with a cell size of 0.125 inches (3.175 mm), a wall thickness of 0.007 inches (0.178 mm) with a height of 0.5 inches (12.7 mm). This was sandwiched between two face sheets, each manufactured using 5 plies of carbon fiber with a layup pattern of [0/90/0/90/0] and bonded using FM 300 film adhesive. Three different types of damage were created for this study, including horizontal and vertical slicing of the core, as well as crushing of the core. The specifications for each defect are shown in Table 10 which provides the size and type of damage created as well as the ply layup and surface preparation for each trial.

Test Panel ID	Number of Plies	Layup Orientation	Surface Preparation	Core Defect	Defect Size (mm)
Test Panel 7	5	[0/90/0/90/0]	Acetone	Slice 1	L = 28.5 (b)
Test Panel 7	5	[0/90/0/90/0]	Acetone	Slice 2	L = 22.9 (a)
Test Panel 7	5	[0/90/0/90/0]	Acetone	Crushed Core 1	D = 14.4 (c)
Test Panel 7	5	[0/90/0/90/0]	Acetone	Crushed Core 2	D = 19.8 (d)
Test Panel 7	5	[0/90/0/90/0]	Acetone	Slice 3	Depth = 2.5 mm
Test Panel 7	5	[0/90/0/90/0]	Acetone	Slice 4	Depth = 3.5 mm
Test Panel 7	5	[0/90/0/90/0]	Acetone	Slice 5	Depth = 6.5 mm
Test Panel 7	5	[0/90/0/90/0]	Acetone	Slice 6	Depth = 8.5 mm

Table 10: Properties for test panel 7 and created damage types. The first four damage types are label below in Figure 75 (a-d).

For the first four defects, the damage to the honeycomb core was produced before the face sheet was adhered to it. This consisted of two dents produced by the Impactors 1 and 2 being pushed down into the honeycomb core, which crushed the cell walls deep enough that the film adhesive did not bond to the core. As shown in Figure 75, two vertical slices were added beside the crushed core, one of which was a thin slice only affecting a single column of cells (b), while the second slice was first cut and then the cell walls were crushed down to produce a V shaped valley (a).

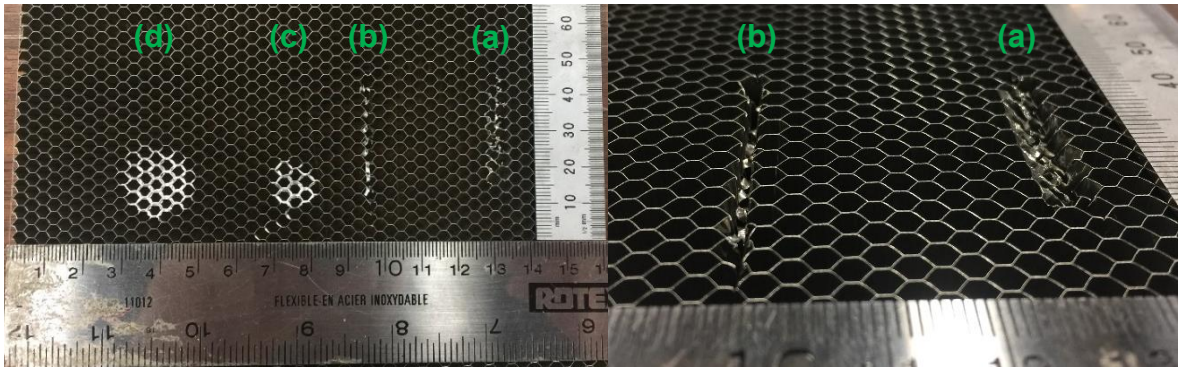

(a) (b)

Figure 75: Test Panel 7 (5 Ply, [0/90/0/90/0]) First four defects created before the face sheet was adhered to the honeycomb core.

Figure 76 shows the acquired thermogram for the first four defects. The locations in which the core was crushed before the face sheet was adhered look similar to the results presented in Section 4.2, where the honeycomb core as well as the film adhesive were crushed to their maximum depth and remained depressed before the face sheet was able to relax back to its original position thereby creating a disbond. A small, ~1°C temperature difference is present when comparing these two types of defects. The film adhesive, which remains attached to the face sheet in Figure 76 (c,d) is able to absorb more of the applied thermal energy, making it appear slightly cooler than a disbond between the film adhesive and face sheet.

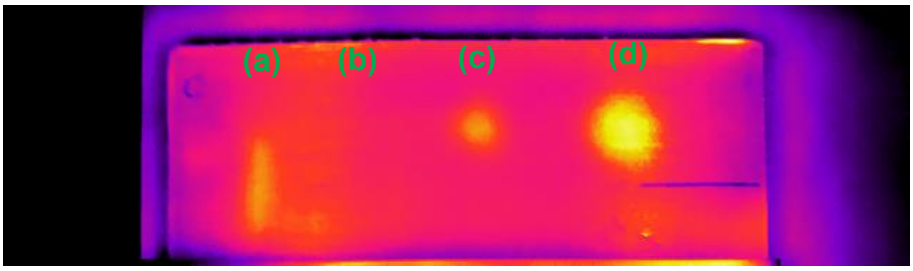

Figure 76: Test Panel 7 (5 Ply, [0/90/0/90/0]) IR thermal image of the face sheet. The scan was not able to detect slice 1, which only affects one column of cells. Advanced Plateau Equalization algorithm applied.

Figure 76 shows the acquired IR thermography image for the first four defects. A temperature line profile was taken across each of the defects and are shown in Figure 77.

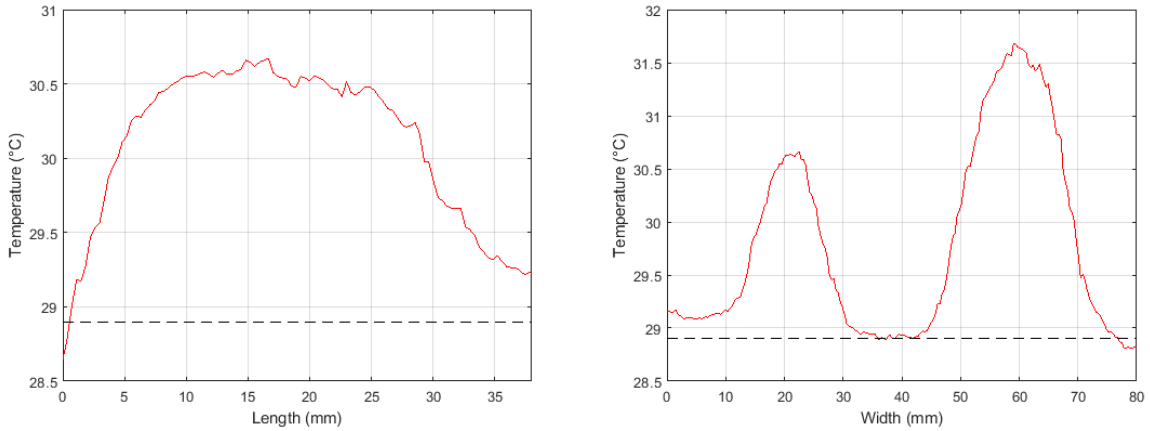

(a) (b)

Figure 77: Test Panel 7 (5 Ply, [0/90/0/90/0]) Temperature line profile for the length of slice 2 (a) and diameter of crushed core 1 and 2 (c and d).

The line profile taken for both the slice and the core crush overestimated the defect's size. The diameter of the small core crush was measured to be 19.1 mm versus the actual diameter of 14.4 mm, while the diameter of the larger core crush was measured to be 26.8 mm versus the actual diameter of 19.8 mm. The thermal energy dissipated around the slice, which makes it appear wider and longer, affected the measured length of 32.9 mm versus the actual length of 22.9 mm. This effect was also seen in the third study (4.3) where the diameter of the deeper voids appeared wider due to the thermal energy dispersing outwards in the thicker face sheet. The slice, which only affected one column of cells, was not detected by the IR camera, but it is thought that changing the lens to have a closer look at the cell walls would be beneficial and offer a better possibility of detecting it. The over estimation of a defect's size was discussed in the last study (4.3) and is attributed to thermal energy laterally dissipating into the face sheet.

For the second set of damage (slices 3 through 6), the defects were created after the face sheet had been adhered to the honeycomb core, and consists of four horizontal slices at varying depths along the side of the test panel as shown in Figure 78 (a). Thermal energy was applied to the top face sheet for 2 seconds before the images were acquired. The 2 second heat time allowed the thermal energy to penetrate deep enough into the test panel to detect the deepest 8.5 mm slice without oversaturating the thermogram. The IR thermography results for this study are shown in Figure 78, which are followed in Figure 79 by a plot of the slice's depth as a function of the maximum temperature the slice reached.

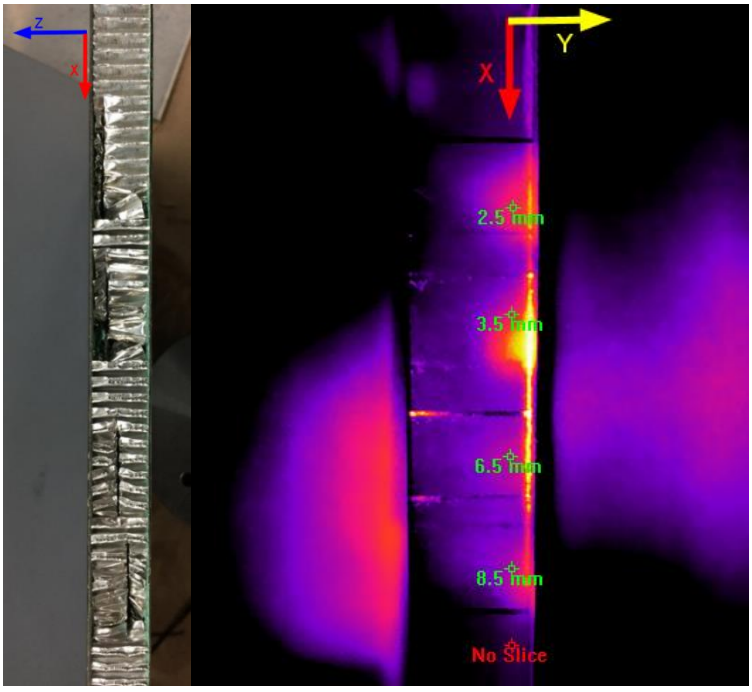

(a) (b)

Figure 78: Test Panel 7 (5 Ply, [0/90/0/90/0]) IR thermal image of the face sheet showing the maximum temperatures for slices 3-6. When creating the 3.5 mm slice, a small section of film adhesive was torn from the face sheet resulting in a temperature spike just below the labeled [3.5 mm]. Advanced Plateau Equalization algorithm was applied.

The maximum temperature for each of the slices was recorded and plotted below in Figure 79. The maximum temperature follows a linearly decreasing trend as the depth of the slice is increased.

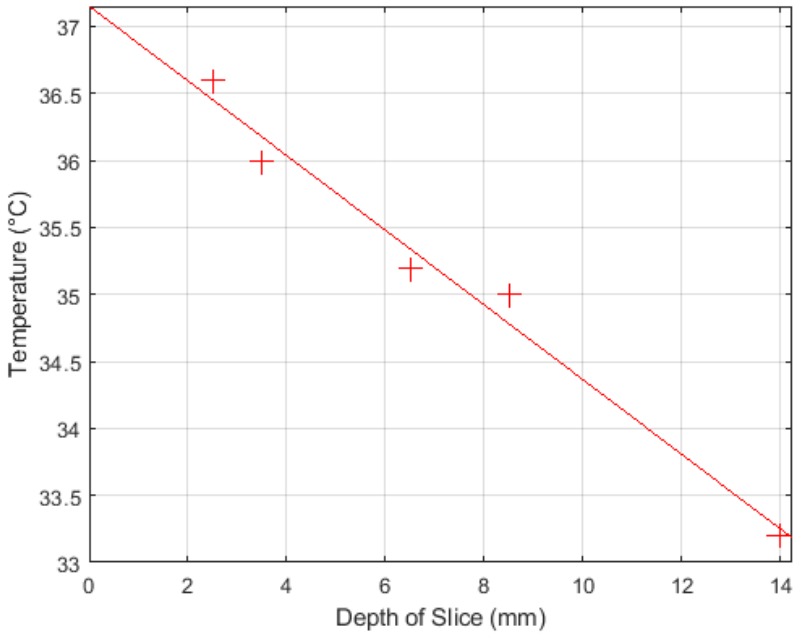

Figure 79: Test Panel 7 (5 Ply [0/90/0/90/0]) Maximum temperature for slices 3-6 as well as a non-defective region plotted at a depth of 14mm.

As shown in the Section 4.2, the maximum temperature of the impact location is related to the defect's diameter and depth. The closer a void is to the surface, the hotter that location will appear and the shorter the detection time that is required. It is usually quite obvious if a defect occurs within the face sheet versus in the core material as the honeycomb core hexagonal shape becomes visible after the thermal energy has passed through the face sheet. Detecting slicing or ripping of the honeycomb cell walls is more difficult than detecting defects occurring in the composite face sheet and requires thoroughly inspecting a suspected region using a smaller field of view at an increased zoom. Increasing the zoom, allows the identification of individual cell walls for inspection and offers a better idea if a discontinuity is present.

4.5 Distinguishing Each Type of Flaw

It is important to distinguish which type of defect is detected from a thermal scan, as some types are more critical than others and might require immediate attention or repairs. The purpose of this study was to provide information on how to distinguish a disbond from a core to film adhesive unbond or a delamination occurring within the plies, or distinguishing water ingress from a region with excess adhesive. Figure 80 displays each of the defects discussed in Section 2.3 with the exception of water ingress, which is looked at in more detail in the next study (4.6) using passive thermography. In Figure 80, the honeycomb core cell walls, the area inside an individual cell of the honeycomb core as well as various different types of defects are visible. It is sometimes helpful to view the thermograms in grayscale (pictured below) opposed to a pseudocolor image to help distinguish different types of defects. This is highly dependent on the post processing algorithms used, and is up to the user to decide.

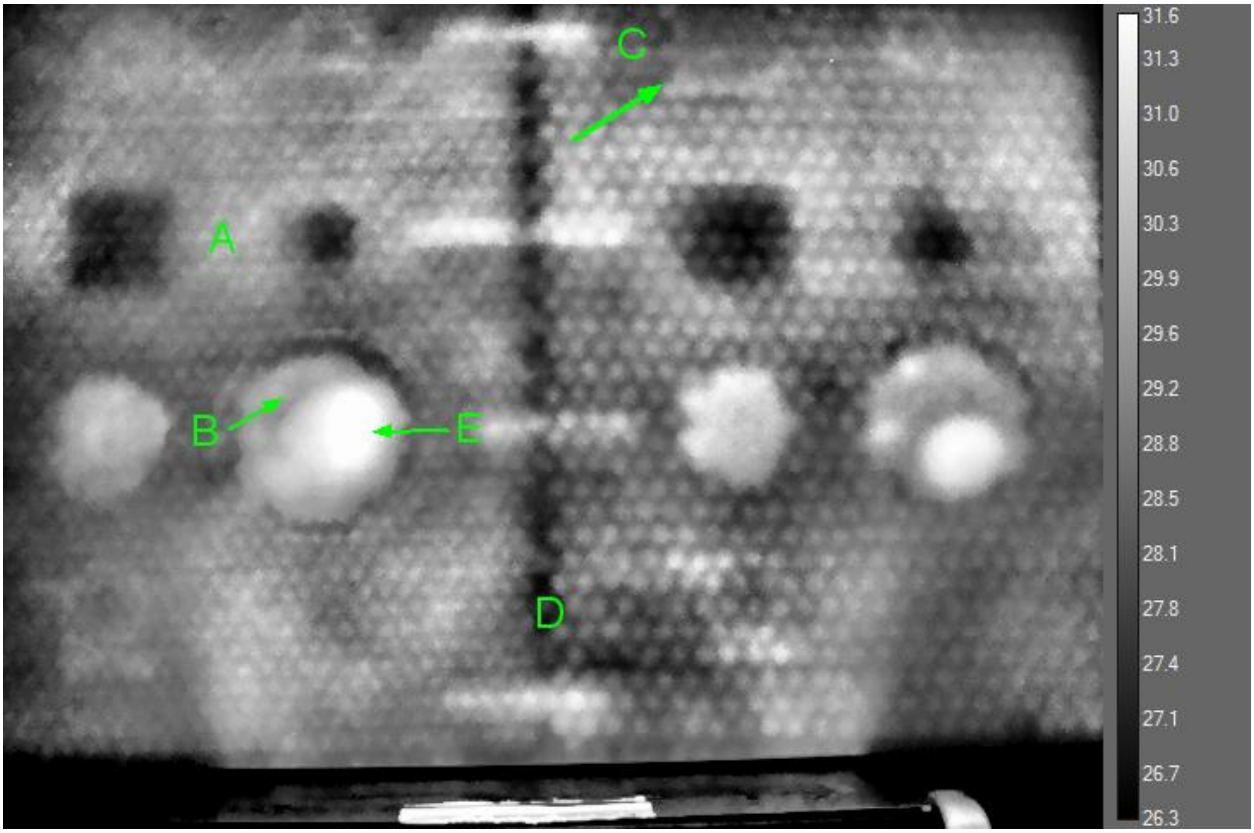

Figure 80: Test Panel 8 (6 Ply, [0/90/-45/+45/90/0]) A: Excess adhesive, B: Face sheet-film adhesive disbond, C: Adhesive-Core disbond, D: Core splice, E: Delamination between plies. Advanced Plateau Equalization algorithm was applied.

4.5.1 Excess Adhesive

An area which contains excess adhesive is perhaps the easiest to distinguish from the other types. This is the only type to show up as a darker, colder area as opposed to the other types, which show as a bright hot area. Water ingress also shows up as a dark cold region, but can be distinguished from excess adhesive by using passive thermography, which is discussed in the next study (4.6). Figures 81 and 82 provide an IR thermography image of a region with excessive adhesive, a temperature line profile taken across the right defect as well as the cross sectioned image.

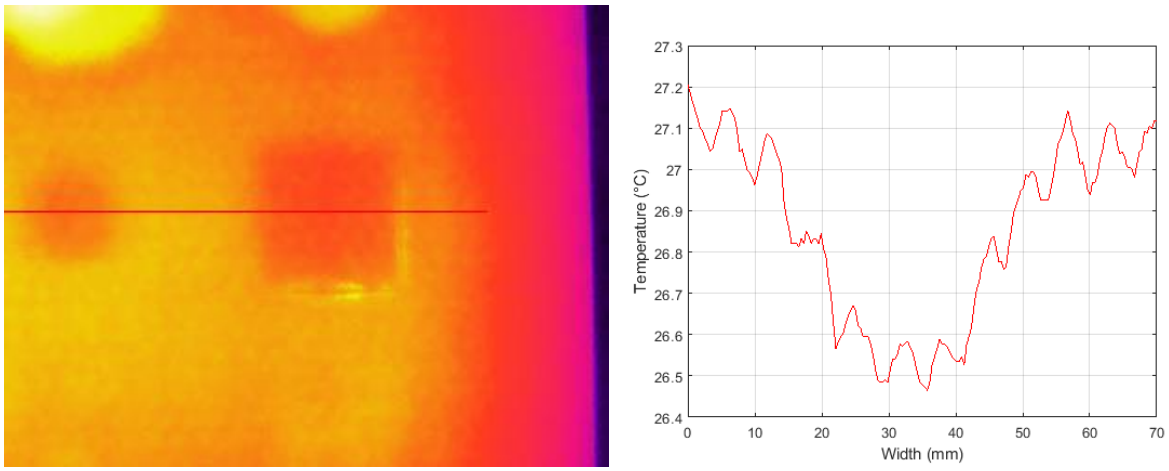

(a) (b)

Figure 81: Test Panel 8 (6 Ply, [0/90/-45/+45/90/0]) Thermography image of excess adhesive contained between the face sheet and honeycomb core (a) Temperature line profile taken across the right defect (b). Plateau Equalization algorithm was applied.

Figure 82: Test Panel 11 (5 Ply, [0/-45/90/+45/0]) The green arrows point to the two layers of film adhesive, which are able to absorb extra thermal energy.

It is shown that a region, which contains too much adhesive, is able to absorb more of the applied thermal energy than the surrounding areas, which contain the regular amount of film adhesive. The area with double the amount of film adhesive drops in temperature by just under 1°C, which is enough to display a dip in the temperature line profile indicating a flaw.

4.5.2 Disbond and Delamination

A disbond in-between the face sheet and film adhesive can appear similar to a delamination in-between plies, however there is a small ~1°C temperature difference between them when they are compared side by side. Due to the delamination occurring in between plies, the thermal energy is blocked from penetrating any deeper. This slight difference is enough to tell how deep the defect is. In Figure 83, the disbonded impact area on the right also contains a delamination in-between plies. A small step in the temperature line profile reveals this, which has almost the same maximum temperature of the smaller impact area on the left, which only contains a disbond.

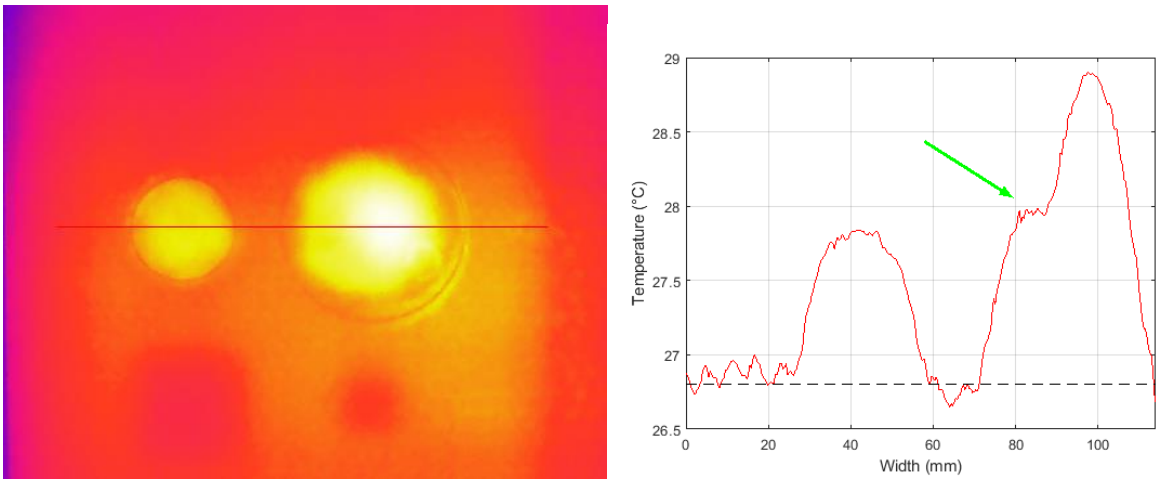

(a) (b)

Figure 83: Test Panel 8 (6 Ply, [0/90/-45/+45/90/0]) Thermography image of two disbond locations occurring in-between the face sheet and film adhesive (a). The larger impact on the right also contains a delamination, which causes the spike in the temperature profile (b). Plateau Equalization algorithm was applied.

Any disbond or delamination will show up as a hot spot compared to the surrounding non-defective regions. It is then up to the technician to further study the defective location and determine its type and potential risk to the strength of the face sheet.

4.5.3 Adhesive to Core Disbond

An adhesive-to-core disbond may appear similar in temperature and look similar to a disbond occurring in-between the face sheet and film adhesive. However, under closer inspection, the drops in the temperature line profile are due to the honeycomb core underneath that location dissipating the applied thermal energy. In a location where the core has become unbonded from the film adhesive, the energy cannot penetrate any further down, causing that location to appear hotter. Small dips in the temperature line profile are still present, which are caused by the valleys left in the film adhesive from once being bonded to the honeycomb core. Figures 84 and 85 demonstrate a film adhesive to core disbond.

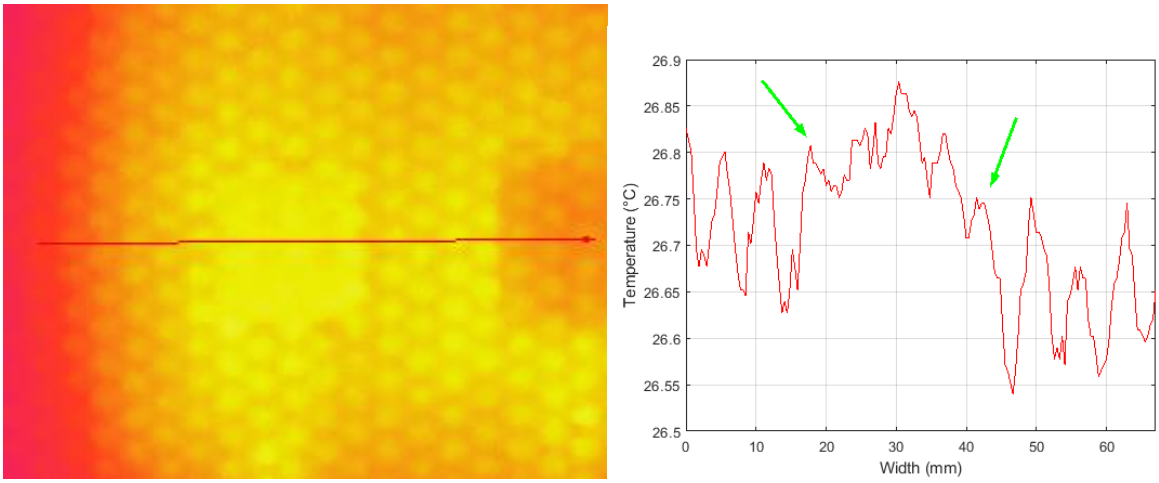

(a) (b)

Figure 84: Test Panel 8 (6 Ply, [0/90/-45/+45/90/0]) Thermography image of a honeycomb core-to-film adhesive unbond. The lack of honeycomb cells in the center of this image may make this type of defect stand out against the surrounding area (a). The temperature line profile confirms this with a noticeable lack of valleys there (b). Plateau Equalization algorithm was applied.

Figure 85: Test Panel 11 (5 Ply, [0/-45/90/+45/0] Impact energy of 0.88 J. The green arrows point to where the honeycomb core has become unbonded from the film adhesive, leaving a small void.

4.5.4 Interlaminate Voids from Manufacturing

Poor manufacturing of the face sheets may lead to porosity or unbonded locations in-between the individual plies. Figure 86 is an example of a face sheet that contains many interlaminate voids that could be mistaken for impact damage if it was put in service before inspecting it with a thermal camera. The surface of this face sheet appears smooth and was adhered to the honeycomb core before these voids were detected.

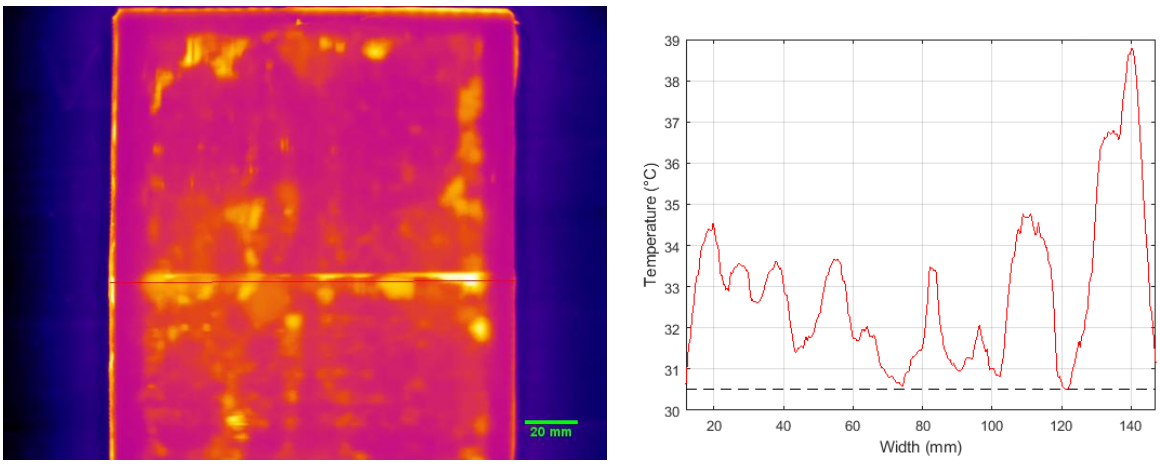

(a) (b)

Figure 86: Test Panel 9 (6 Ply, [0/90/-45/+45/90/0]) Thermography image of a number of manufacturing errors occurring within the face sheet. These small air pockets each correspond to a temperature spike in the temperature line profile (b). Plateau Equalization algorithm was applied.

4.6 Detecting water ingress

This study looks at how water ingress into the honeycomb core can be detected using passive IR thermography instead of the active techniques discussed in the previous sections. Water that is able to seep into the honeycomb cells, either during flight or while the aircraft is stationary may be detected using passive IR thermography, due to its difference in thermal diffusivity from the surrounding carbon fiber and aluminum. The trapped water has the lowest thermal diffusivity and highest heat capacity between the three and will cause a large temperature gradient when viewed through a thermal camera.

The test panels manufactured for this study use a honeycomb core material of 5052-H34 aluminum, with a cell size of 0.125 inches (3.175 mm), a wall thickness of 0.007 inches (0.178 mm) with a height of 0.5 inches (12.7 mm). This was sandwiched between two face sheets, each manufactured using 5 plies of carbon fiber with a layup pattern of [0/90/0/90] and bonded using FM 300 film adhesive. To add the water to the cells, holes were drilled through the back side of the test coupon after it was completely manufactured and water was added to individual cells using a syringe. It was thought that adding water to the cells before the face sheet was adhered to the core would cause the water to evaporate or leak out during the curing process. The drilled holes were then sealed using silicone to trap the water. Once the silicone had cured, the test panel was placed in a freezer for a number of hours to allow the water to freeze as well as let the entire test panel drop to the same temperature. The test panel was then removed from the freezer and placed under the IR camera, which monitored it for 150 seconds; this was enough time to clearly show the trapped ice compared to the surrounding non defective areas. Regions of interest were placed on non-defective areas of the panel's surface as well as the cells, which contained the trapped ice. The temperature was monitored in these locations and the temperature rise for each is plotted in Figure 87.

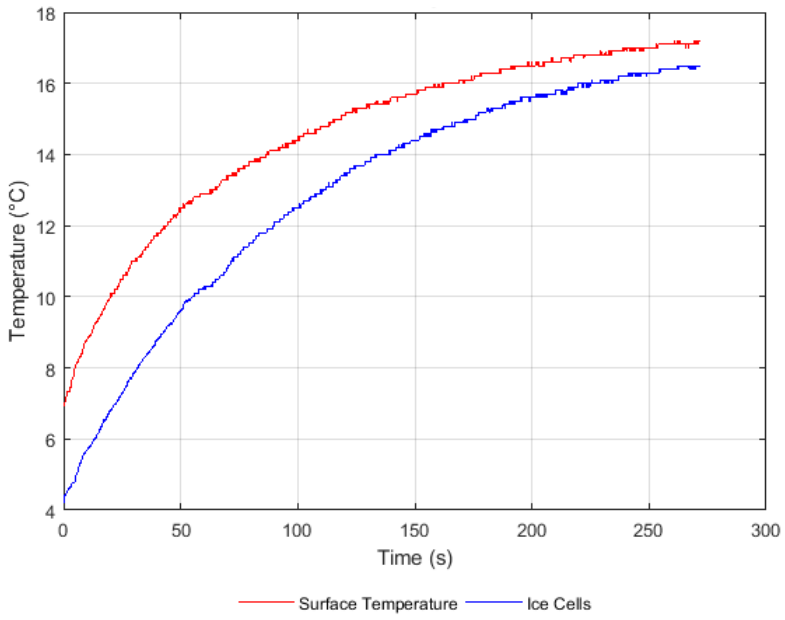

Figure 87: Test Panel 10 (4 Ply, [0/90/0/90]) Temperature profiles for a location which contains ice in 6 of the honeycomb cells (Blue) and a non-defective region (Red).

The small temperature difference at the start of the trial is due to the surface of the test panel heating up in the approximate 5 seconds it took to transfer the test panel from the freezer to in front of the IR camera. Images were taken every 30 seconds and stacked in sequence to show the temperature evolution of the surface of the test panel; these can be seen in Figure 88. When ice is present under the face sheet, it becomes very obvious to spot, however, estimating how many cells were affected was difficult. This is due to a problem discussed earlier when using the 1D versus 3D heat diffusion equation. The ice is able to absorb thermal energy out of the surrounding cells, which do not contain trapped ice, making them appear colder.

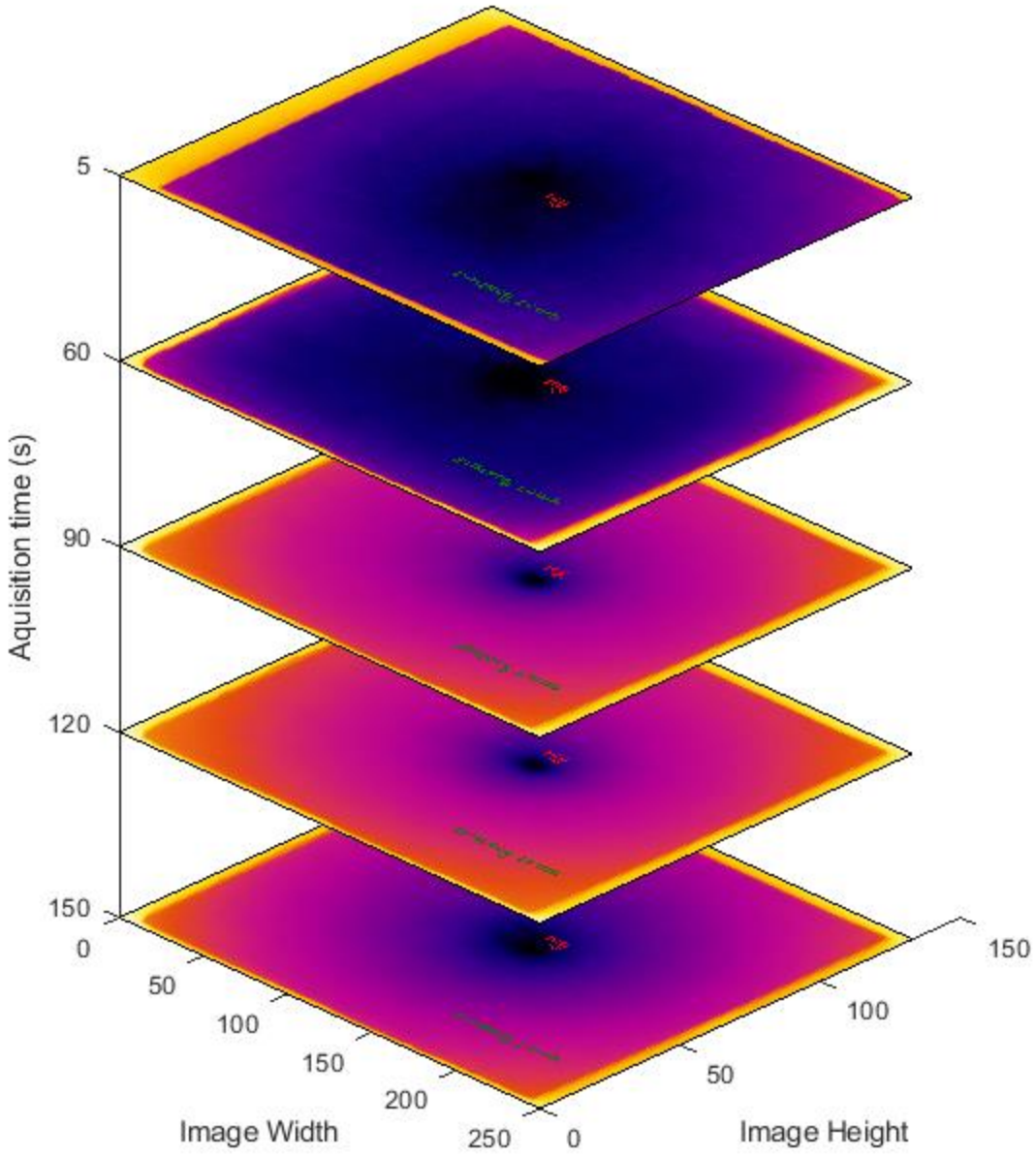

Figure 88: Test Panel 10 (4 Ply, [0/90/0/90]) Time evolution of the face sheet represented by five images in the stack. Images were acquired every 30 seconds and after 150 seconds, ice indicated by the dark blue location at the center of the test panel becomes quite obvious compared to the surrounding non-defective area.

When detecting water or ice using passive thermography, it is important to monitor the surface temperature of the face sheet immediately after the environmental conditions have changed. The solid ice takes a longer period of time to reach room temperature when compared to the surrounding aircraft materials. The ice first needs to melt into a liquid before warming up, and this small time delay before the ice has melted offers enough thermal contrast to distinguish a region containing sub-surface ice. It is best to perform passive thermography with the same techniques in mind as active thermography, which is to create a large thermal gradient between the defective region and surrounding region. When looking for trapped ice, best results are acquired when taking the test panel from a sub-zero environment immediately to a warm environment. If this technique is used on panels, which are insitu, this would require taking the aircraft into a warm hangar and examining the panels quickly before the ice has a chance to melt.

4.7 Thermographic Signal Reconstruction method

This study looks at using time dependent calculations to reduce an image's noise, while increasing its temporal and spatial resolution. Taking a sequence of images at a high frame rate allows one to see the applied thermal energy propagate down through the face sheet and offers the ability to look at individual plies, as opposed to a single frame in time. Looking at Figure 89, the first image was acquired 0.73 seconds after the heating lamps were turned off, the surface is noisy and the temperature is fairly uniform across the face sheet's surface. The next slice in the sequence, taken 0.27 seconds later shows small bright patches, which represent small delaminations in the third carbon fiber ply. This is shown in detail in the upper right of Figure 89. In the third slice, which was acquired 1.73 seconds after the heating lamps were turned off, a disbond located in the bottom center of the test panel is now visible. After the thermal energy had travelled through all five plies and reached the boundary between the face sheet and film adhesive, three disbond locations became visible and are shown in detail in the bottom right of Figure 89.

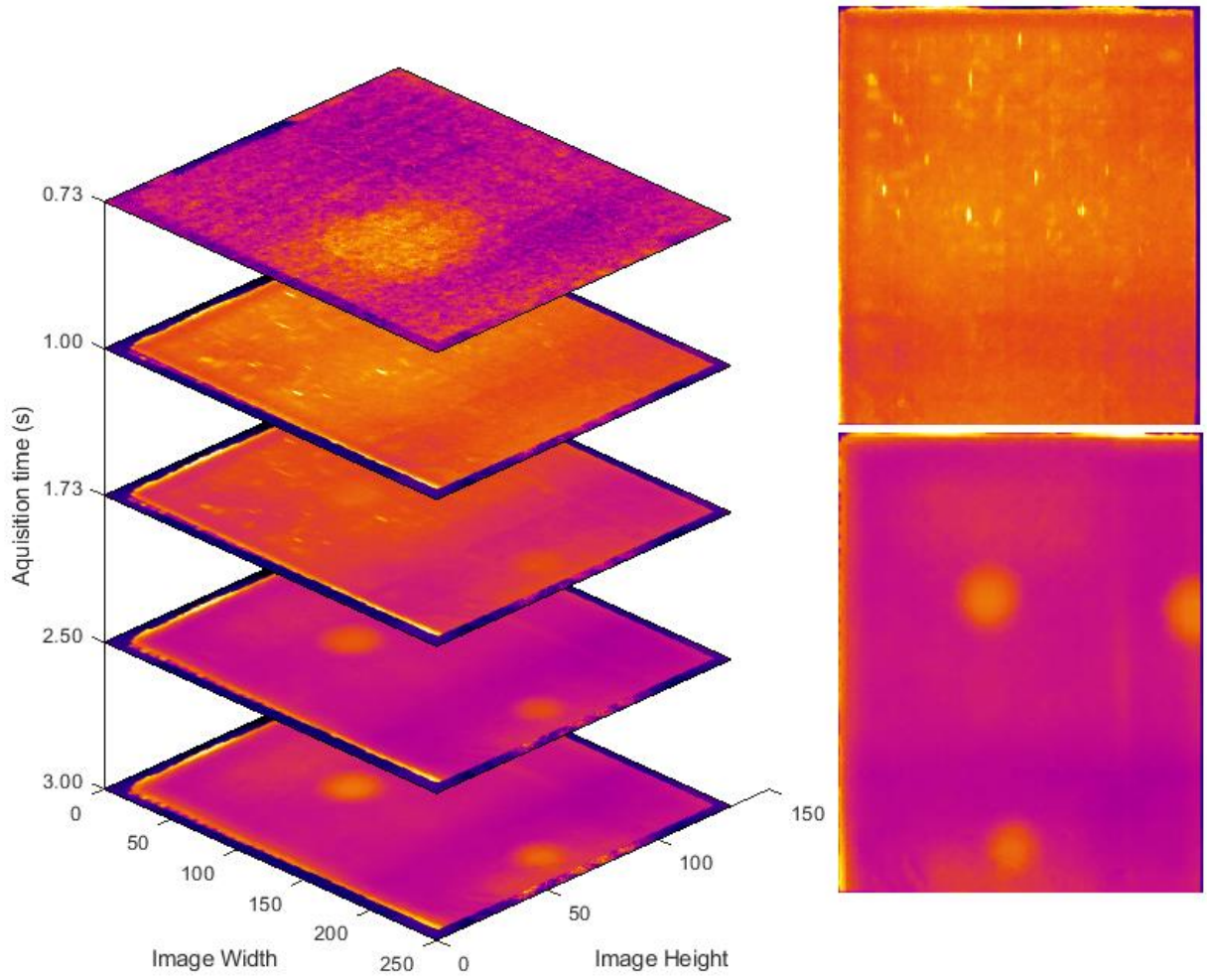

Figure 89: Test Panel 1** (4 Ply, [0/90/0/90]) Sequence of images taken after a 1 second heating period, showing delaminations in the third ply and three core-face sheet disbonds.

Figure 89 demonstrates how taking a sequence of images allows monitoring of the thermal energy as it propagates into the test panel. Noise filtering as described in Section 2.4.7 as well as contrast adjustments were performed to achieve a clean image, which clearly shows all of the defective regions. If a defective area is still not clearly visible from taking a sequence of images, applying the Thermographic Signal reconstruction technique (TSR) technique may help to identify these regions. For the next trial, the TSR method was used to demonstrate its ability to locate a defective region in a much shorter period of time by taking the first and second derivative of each image in the sequence. As mentioned in Section 2.4.6, the first derivative of a

thermogram gives the rate of cooling, while the second derivative of a thermogram gives the rate of change in the rate of cooling.

The same test panel used in Section 4.3, which was used to determine a defect's depth was also used in this study and was subjected to a 0.5 second heating period followed by a 5 second cooling period. A sequence of thermograms was recorded throughout the heating and cooling cycle at a rate of 30 frames per second for a total of 150 frames.

Using Equation 8 from Section 2.4, a 5th order polynomial was fit to the temperature decay curve and was reconstructed using Equations 9 and 10, producing the nine TSR images in Figure 90.

$$ln[T(t)] = \sum_{n=0}^{N} a_n [\ln(t)]^n \tag{9}$$

$$T(t) = exp\left(\sum_{n=0}^{N} a_n [\ln(t)]^n\right) \tag{10}$$

Using Equation 10, the first and second derivative images in Figure 90 can be produced using Equations 11 and 12 below. A non-processed image, a TSR processed image, as well as the first and second derivative images given by Equations 11 and 12 are provided for each of the nine frames and compared in Figure 90 for the samples heating and cooling period.

$$\frac{dln(T)}{dln(t)} = \sum_{n=0}^{N} n a_n \ln(t)^{n-1} \tag{11}$$

$$\frac{d^2 \ln(T)}{d^2 \ln(t)} = \sum_{n=2}^{N} n(n-1) a_n \ln(t)^{n-2} \tag{12}$$

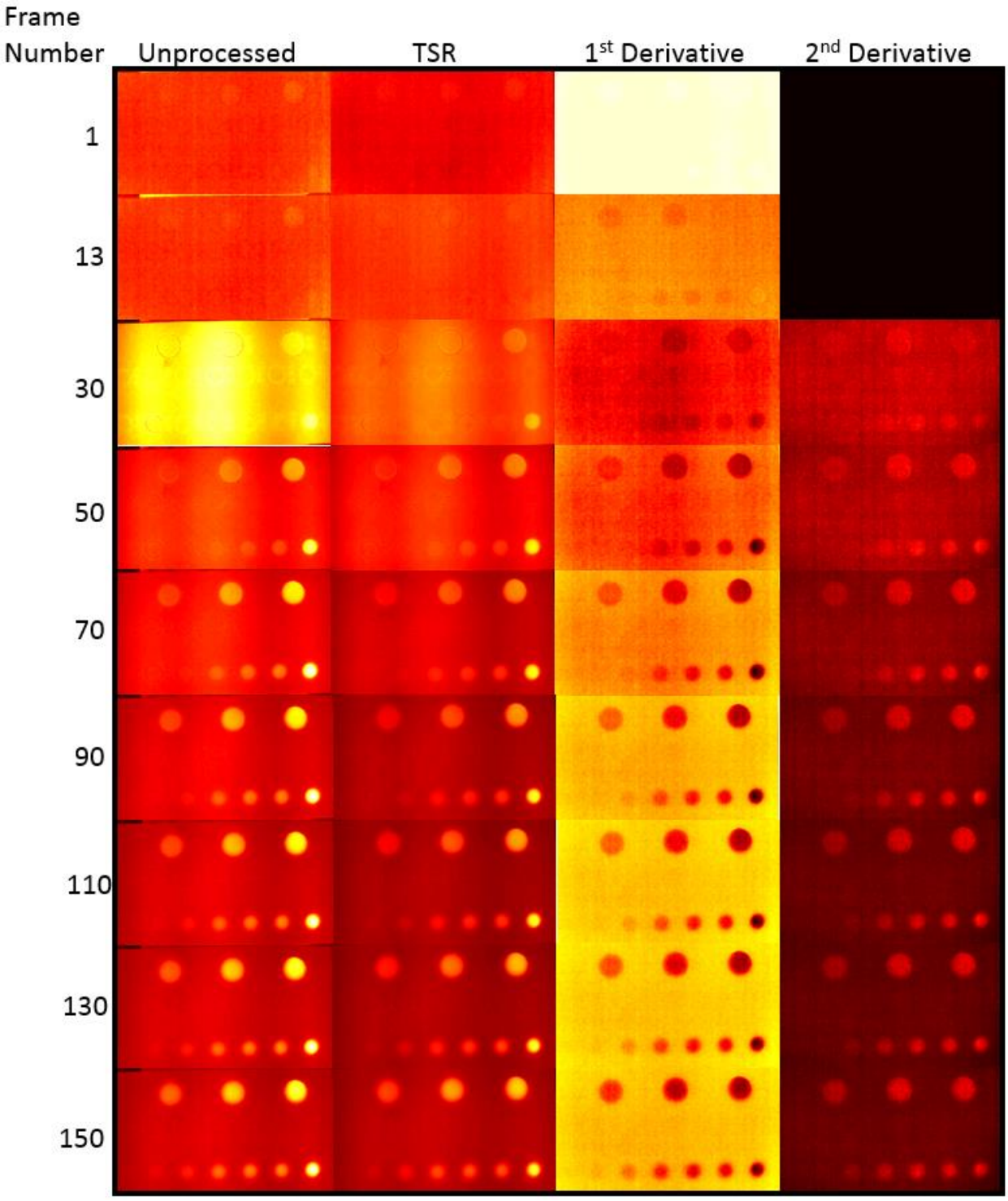

Figure 90: Test Panel 6 (84 Ply, $[0/90/-45/+45/90/0]_{14}$) Thermographic-signal-reconstructed images for selected frames. The heating period takes place between frames 13-30, at which it reaches its maximum temperature, followed by a cooling period from frames 30-150. Displaying unprocessed, TSR processed and the first derivative and second derivative images.

As soon as the halogen lamps are turned on in the 13th frame, it becomes immediately obvious that the first derivative image is displaying three of the seven defects of the bottom row. Once the halogen lamps turned off in 30th frame, the surface temperature had reached its maximum temperature and the surface starts to cool down. The unprocessed image is noisy and saturated, making this image unusable and hard to distinguish any sort of defect in it. Looking at the first and second derivative images, which display the rate of cooling and rate of change in the rate of cooling, four of the seven defects are faintly displayed. Moving ahead to the 50th frame, the unprocessed image clearly displays the 0.254 mm defect, but none of the other defects are obvious. This is where the TSR method thrives, as the first and second derivative images clearly display defects 0.254-1.016 mm.

As the thermal energy propagates down into the sample, the unprocessed image in the 70th frame is now faintly displaying the first four defects, 0.254-1.016 mm, while the first derivative image is starting to display the 5th, 1.270 mm defect. After this point in time, the unprocessed image can faintly display five of the seven defects, but is not able to detect the remaining two at depths of 1.905 and 2.54 mm deep.

It is interesting to note that the first and second derivative image displays each of the defects at a similar color, as the first derivative displays their cooling rate and not their temperature as in the unprocessed image. The TSR method does a great job at removing noise, and displaying defects with a very low thermal contrast. The first and second derivative images are able to display defects much earlier time, than a single thermogram.

The TSR method can be used with great success when looking for defects with a very low thermal contrast. It is good practice to run the TSR method when an image contains a lot of noise as the first and second derivatives display the rate of heating or cooling and helps to reveal low contrast areas. There isn't a set guideline when it comes to applying algorithms, in most cases the first and second derivative of the TSR image result in the cleanest images and remove any unwanted hotspots. However, the TSR method takes a lot of processing power and time as the algorithm needs to map each pixel separately. Choosing which order of polynomial to fit to the data can be difficult and the optimal choice depends on how much noise is present in the acquired images. Choosing a small degree requires less computation time, and also contains less oscillations in the fit. Choosing a large degree, is computationally heavy and will contain many oscillations in the fit, some of which will caused by unwanted noise. Therefore,

choosing a degree appropriate for the acquired data is required. In most cases a 5^{th} or 7^{th} order polynomial provides a clean image, while minimizing computation time.

5 CONCLUSION

A detailed explanation of the manufacturing process for carbon fiber sandwich panels has been presented. Different damage types were introduced into the test panels and pulsed thermography was used to successfully detect and identify each damage type.

- In the case where the face sheet remains adhered to the honeycomb core after an impact event, a visual indentation to the face sheet can be measured using the edge of light method [36] and 3D laser scanning. According to the Federal Aviation Administration's guidelines for testing and inspecting composite honeycomb panels, if the residual indentation is visible and remains adhered to the core, the damage must be able to withstand a once per lifetime load (ultimate limit load) and requires repairing if the indentation grows, cracks or becomes disbonded [12].

- Disbonds occurring in-between the face sheet and film adhesive provide the greatest contrast and are easily detectible. Section 4.2 establishes a relationship between acquired thermogram data and a disbond's depth and width. The face sheet's thermal diffusivity influences the amount of lateral heat diffusion, which can result in a larger measured diameter if the 1D heat diffusion equation is used. The 3D heat diffusion equation should be used in place to account for this error. The width of a defect should be measured as quickly as possible to prevent this, and depending on the type of defect, different measuring techniques should be experimented with. Disbonds occurring in-between the film adhesive and honeycomb core are distinguishable from a face sheet-to-adhesive disbond using a temperature line profile.

- The depth of a delamination or disbond may be calculated using its standard thermal contrast. A calibration defect with a known depth and dimeter is required for this method, as well as the face sheet's material properties and provides an accurate method for determining an unknown defects depth and size.

- Matrix cracking and delaminations occurring in the face sheet can be identified and flagged for further examination using a higher resolution NDT method.

- Water ingress is easily detectable due to its low thermal diffusivity and high heat capacity. Passive thermography was able to detect trapped ice and distinguish it from the surrounding non-defective carbon fiber face sheet. For best results, this method should be applied immediately after the aircraft has been brought from a sub-zero environment to a warm environment.

- The Thermographic Signal Reconstruction method reduces the noise in an acquired thermogram while increasing its temporal and spatial resolution. This method is able to detect a defect in a much shorter period than a single thermogram. The first and second derivatives provide the rate of cooling and the rate of change in the rate of cooling. These can both successfully locate defects with a low thermal contrast.

The testing apparatus was designed and manufactured for less than $100, while the FLIR T620 camera had been previously purchased for ~$25K. The infrared camera, lighting setup and image processing were all integrated together using Matlab, Arduino coding and software. The test apparatus may be compared to a commercial flash or pulsed thermography system such as a Thermal Wave Imaging VoyageIR Pro [37], which retails for ~$250K. The same lighting and camera geometry are used, while the bulbs and infrared camera differ. Both systems provide similar detection capabilities and are able to locate damage occurring to the composite face sheet and honeycomb core. In future work, the testing apparatus will be upgraded with Xenon flash bulbs to help increase the contrast of acquired thermograms. Matlab code will be written to automatically identify and measure regions of interest to mitigate subjective inspector interpretations.

5 REFERENCES

[1] Van der Heyden, E. (n.d.). Non-destructive testing for gas turbines - From selecting the best NDT technique to monitoring inspection quality [Pamphlet]. Laborelec.

[2] Hsu, D. K. (n.d.). Nondestructive inspection of composite structures: methods and practice. 17th World Conference on Nondestructive Testing,. Center for Nondestructive Evaluation

[3] Richardson, M. O., & Wisheart, M. J. (1996). Review of low-velocity impact properties of composite materials. Composites Part A.

[4] Odom, B. (n.d.). The Saturn V Moon Rocket. https://history.msfc.nasa.gov/milestones/chpt7.pdf Milestones in Space Exploration - Marshall Space Flight Center (MSFC)

[5] P. (2018, February 15). Saturn V is the Biggest Engine Ever Built. Retrieved August 11, 2018, from https://www.popularmechanics.com/science/a227/1280801/

[6] Young, A. (2009). The Saturn V F-1 Engine: Powering Apollo into history. New York: Springer. Non-Destructive Testing

[7] Bielefeld, M. (n.d.). Boeing 747-8: One plane, six million parts. Retrieved August 22, 2018 from https://magazin.lufthansa.com/xx/en/fleet/boeing-747-8-en/one-plane-six-million-parts/

[8] Aviation maintenance technician handbook: Airframe (Vol. 1). (2012). U.S. Department of Transportation, Federal Aviation Administration.

[9] Farooq, U., Myler, P., & Kandola, B. (2009). Prediction of barely visible impact damage in composite panels subjected to blunt nose impact. UBIR: University of Bolton Institutional Repository,4.

[10] Wowk, D., & Marsden, C. (2016). Effects of skin thickness and core density on the residual dent depth in aerospace sandwich panels. International Journal of Computational Methods and Experimental Measurements, 4(3), 336-344. doi:10.2495/cmem-v4-n3-336-344

[11] Minakuchi, S., Uezono, T., & Takeda, N. (2012). Formation and relaxation of residual facesheet dent on foam-core sandwich structures by localized transverse loading. Journal of Sandwich Structures & Materials, 15(1), 71-91. doi:10.1177/1099636212456862

[12] Fawcett, A. J., & Oakes, G. D. (n.d.). Boeing Composite Airframe Damage Tolerance and Service Experience [PPT]. Boeing Commercial Airplanes. 787 Program

[13] Prior, S. (2016). Characterization of sandwich panels subject to low-velocity impact (Unpublished master's thesis).

[14] Edwards, A. K. (2011). Characterization of the effects of water and disbond on ultrasonic signals in honeycomb composite structures(Unpublished master's thesis).

[15] Liu, Z., Genest, M., Marincak, A., & Forsyth, D. S. (2007). Characterization of surface deformation with the Edge of LightTM technique. Machine Vision and Applications,19(1), 35-42. doi:10.1007/s00138-007-0075-1

[16] Raišutis, R., Voleišis, A., & Kažys, R. (2008). Application of the through transmission ultrasonic technique for estimation of the phase velocity dispersion in plastic materials. ULTRAGARSAS, 63(3).
[17] Abarkane, C., Galé-Lamuela, D., Benavent-Climent, A., Suárez, E., & Gallego, A. (2017). Ultrasonic Pulse-Echo Signal Analysis for Damage Evaluation of Metallic Slit-Plate Hysteretic Dampers. Metals, 7(12), 526. doi:10.3390/met7120526
[18] Thwaites, S., & Clark, N. (1995). Non-Destructive Testing Of Honeycomb Sandwich Structures Using Elastic Waves. Journal of Sound and Vibration, 187(2), 253-269. doi:10.1006/jsvi.1995.0519
[19] Reyno, T., Marsden, C., & Wowk, D. (2018). Surface damage evaluation of honeycomb sandwich aircraft panels using 3D scanning technology. NDT & E International, 97, 11-19. doi:10.1016/j.ndteint.2018.03.007
[20] L. (2018, May 02). HandySCAN 3D to Assess Hail Damage on Aircraft. Retrieved from https://www.creaform3d.com/blog/2015/09/the-handyscan-3d-to-assess-hail-damage/
[21] Edwards, A. K., Savage, S., Hungler, P. L., & Krause, T. W. (2011). Examination of F/A-18 honeycomb composite rudders for disbond due to water using through-transmission ultrasonics. Ultrasound, 66(2). doi:10.5755/j01.u.66.2.529
[22] Foreman, C. (2008). Nondestructive detection and characterization of damages in honeycomb composite structures (Unpublished master's thesis).
[23] Vollmer, M., & Möllmann, K. (2018). Infrared thermal imaging: Fundamentals, research and applications. Weinheim: Wiley-VCH.
[24] FLIR T620. (n.d.). Retrieved November 20, 2018 from https://www.flir.ca/products/t620/
[25] Ciampa, F., Mahmoodi, P., Pinto, F., & Meo, M. (2018). Recent Advances in Active Infrared Thermography for Non-Destructive Testing of Aerospace Components. Sensors,18(2), 609. doi:10.3390/s18020609
[26] Wong, E. (2014). Lecture presented at Western University, Introduction to Thermal Physics, London, ON.
[27] Ibarra-Castanedo, C., Genest, M., Guibert, S., Piau, J., Maldague, X. P., & Bendada, A. (2007). Inspection of aerospace materials by pulsed thermography, lock-in thermography, and vibrothermography: A comparative study. Thermosense XXIX. doi:10.1117/12.720097
[28] Kretzmann, J. E. (2016). Thermographic Image Processing Toolbox for Pulsed and Transient Thermography(Vol. 1, Rep. No. 1). South Africa.
[29] ResearchIR. (n.d.). Retrieved January 10, 2019, from https://www.flir.com/products/researchir/
[30] Rock West Composites PROPreg Data sheet Appendix B
[31] FM® 300 epoxy film adhesive Data sheet Appendix B
[32] FM® 73 epoxy film adhesive Data sheet Appendix B
[33] R&B INC. (n.d.). Standard Test Method for Measuring the Damage Resistance of a Fiber-Reinforced Polymer Matrix Composite to a Drop-Weight Impact Event(Tech. No. 1). American Society for Testing and Materials. doi:ASTM D 7136 / D 7136M-12

[34] Shyprykevich, P. (2003). Guidelines for analysis, testing, and nondestructive inspection of impact-damaged composite sandwich structures. Washington, D.C.: Office of Aviation Research, Federal Aviation Administration.

[35] Wysocka-Fotek, O., Oliferuk, W., & Maj, M. (2012). Reconstruction of size and depth of simulated defects in austenitic steel plate using pulsed infrared thermography. Infrared Physics & Technology, 55(4), 363-367. doi:10.1016/j.infrared.2012.02.004

[36] ImageJ. (n.d.). Retrieved November 20, 2018, from https://imagej.nih.gov/ij/

[37] Thermal Wave Imaging VoyageIr Pro. (n.d.). Retrieved November 20, 2018 from https://www.thermalwave.com/1/376/voyageir_2.asp

[38] Sharath, D., Menaka, M., & Venkatraman, B. (2012). Defect Characterization Using Pulsed Thermography. Journal of Nondestructive Evaluation,32(2), 134-141. doi:10.1007/s10921-012-0166-4

[39] Avdelidis, N. P., Gan, T., Ibarra-Castanedo, C., & Maldague, X. P. (2011). Infrared thermography as a nondestructive tool for materials characterisation and assessment. Thermosense: Thermal Infrared Applications XXXIII. doi:10.1117/12.887403

5 APPENDICES

Appendix A - Surplus Figures

3D Scanning

3D laser scanning results for various 1.18 J impacts occurring to (5,6,7,8) plies of carbon fiber.

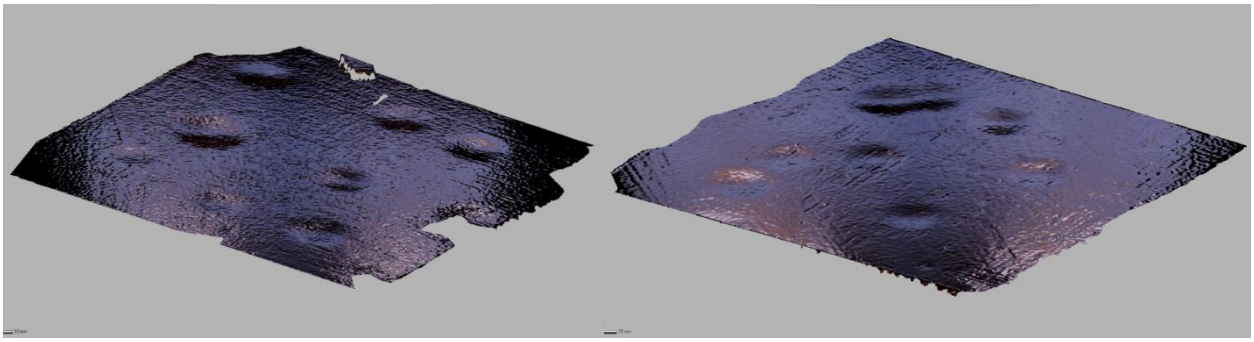

Figure 91: Test Panel 2 (5 Ply, [0/90/0/90/0]) (Left) Test Panel 3 (6 Ply, [0/90/0/90/0/90]) (Right) Impactor 1, Impact energy of 1.18 J. 3D Scanned face sheet with a high gloss texture applied to reveal the impact locations.

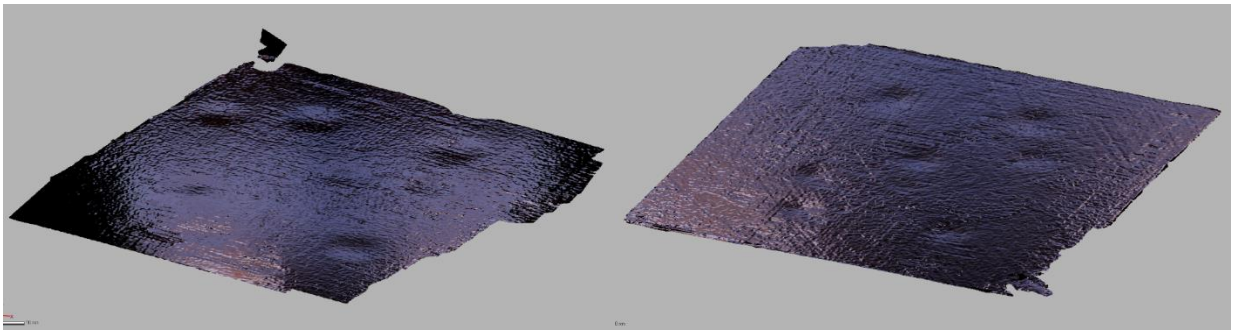

Figure 92: Test Panel 4 (7 Ply, [0/90/0/90/0/90/0]) (Left) Test Panel 5 (8 Ply, [0/90/0/90/0/90/0/90]) (Right) Impactor 1, Impact energy of 1.18 J. 3D Scanned face sheet with a high gloss texture applied to reveal the impact locations.

Excess Infrared thermography results

The same combination of plies and orientations shown above in Section 5.2 were impacted using the same energies mentioned in Section 4.2. The result was a mixture of disbonds and core crush. This was a new batch of carbon fiber and performed differently under impact testing.

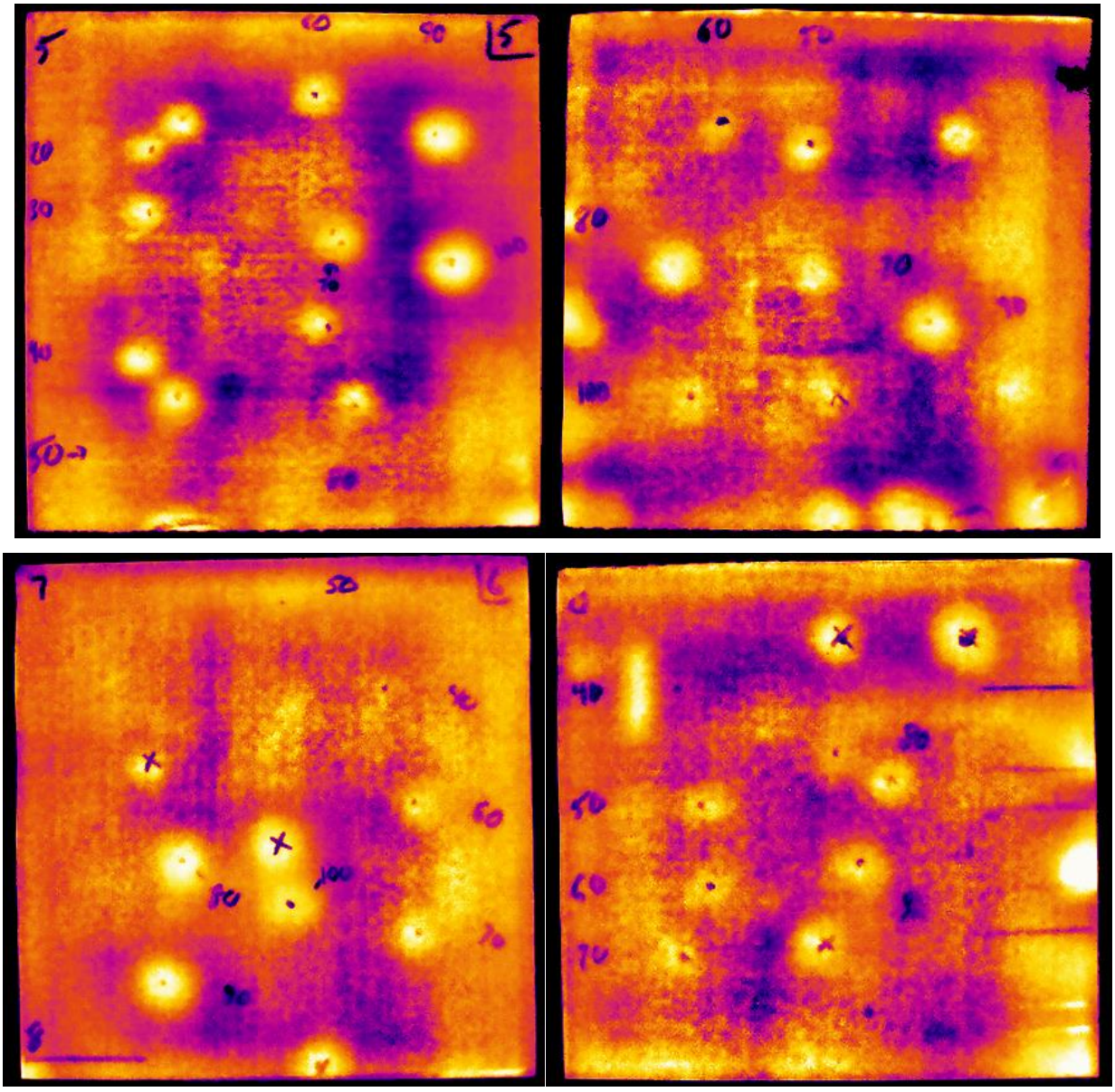

Figure 93: Test Panel 77** (5,6,7,8 Ply, [0/90].

0.7357 J Impact

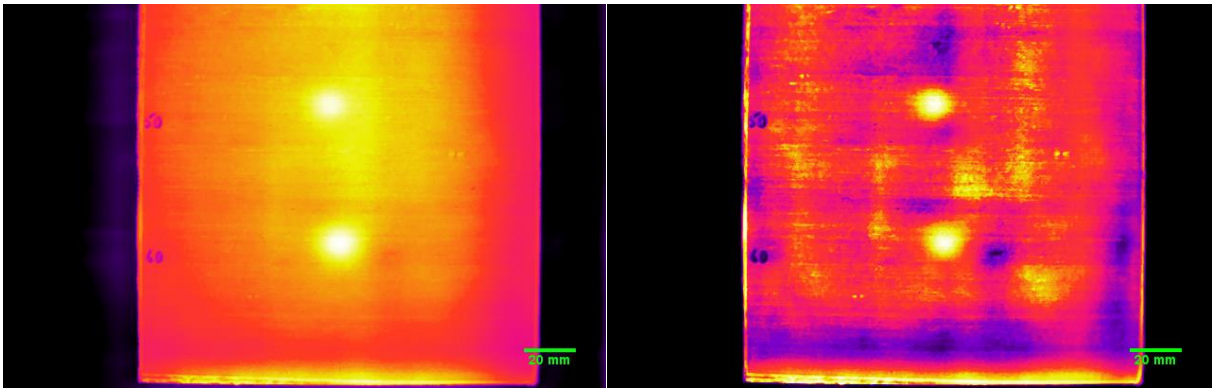

Figure 94: Test Panel 1 (5 Ply, [0/90/0/90/0]) 0.7357-0.8829 J Impacts. Plateau Equalization (Left) Advanced Plateau Equalization (Right)

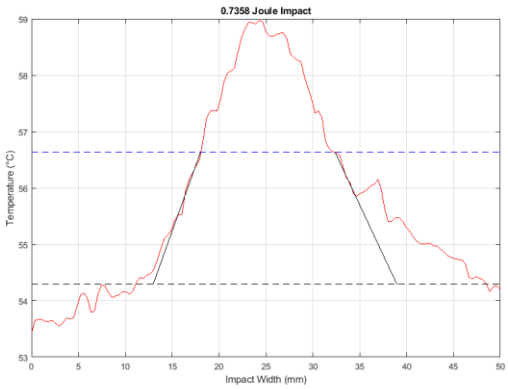

Figure 95: Test Panel 1 (5 Ply, [0/90/0/90/0]) 0.7357 J Impact. Thermography measured width = 25.8 mm (Left), Microscope measured width = 15.3 mm, Microscope measured core crush depth = 0.37 mm (Right).

1.4715 J Impact

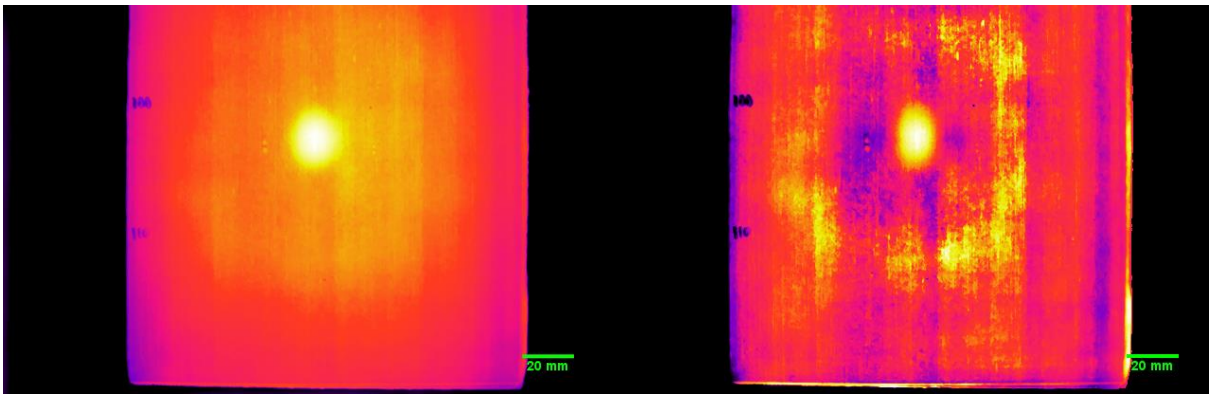

Figure 96: Test Panel 1 (5 Ply, [0/90/0/90/0]) 1.4715 J Impact. Plateau Equalization (Left) Advanced Plateau Equalization (Right)

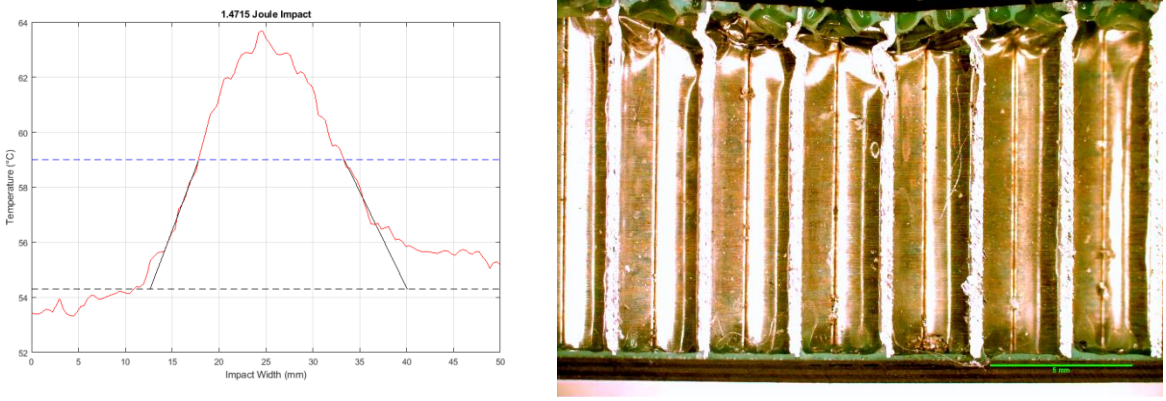

Figure 97: Test Panel 1 (5 Ply, [0/90/0/90/0]) 1.4715 J Impact. Thermography measured width = 27.4 mm (Left), Microscope measured width = 18.8 mm, Microscope measured core crush depth = 0.56 mm (Right).

Eddy current results

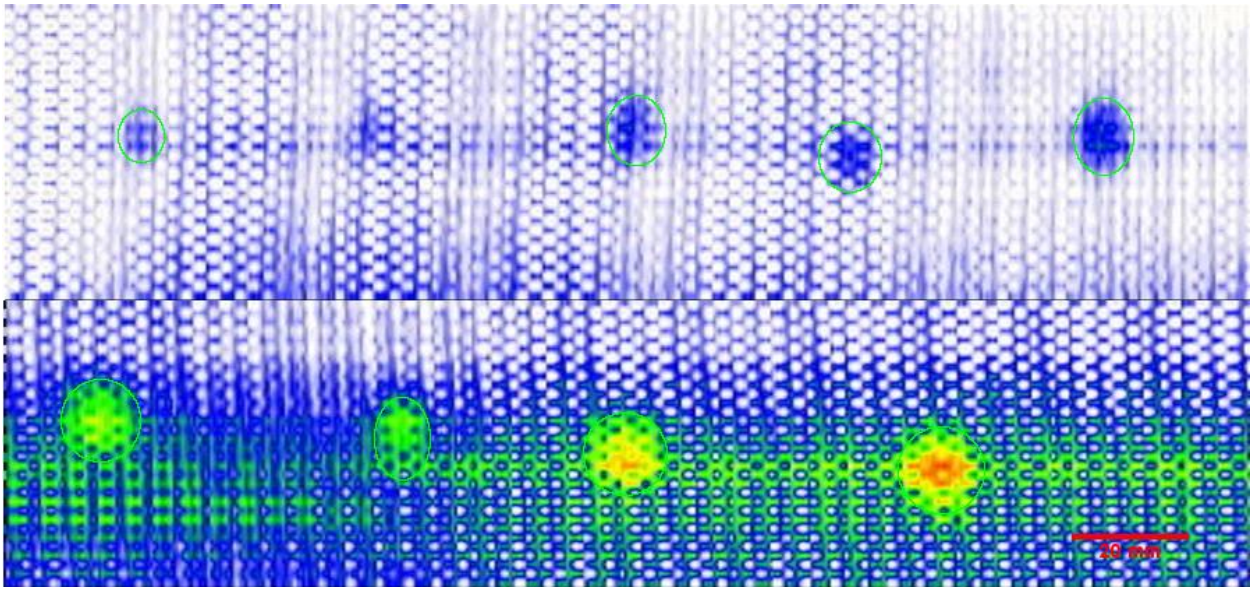

Figure 98: Test Test Panel 1 (5 Ply, [0/90/0/90/0]) Eddy Current scan: From left to right: 0.2943-1.0301 J Impacts (Top). 1.1772-1.4715 J Impacts (Bottom).

FWHM

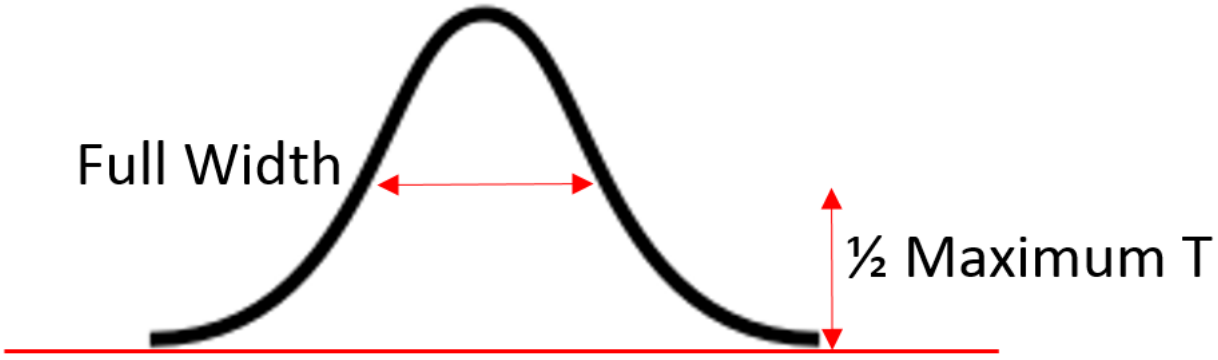

Appendix B - Material Data Sheets

FM® 73 EPOXY FILM ADHESIVE

TECHNICAL DATA SHEET

DESCRIPTION

FM® 73 film adhesive is a toughened, general purpose aerospace epoxy designed to provide excellent structural performance from -67°F to 180°F (-55°C to 82°C). FM 73 film adhesive is formulated to provide outstanding durability in bonding metals and is also suitable for boding many structural composite systems.

Extensive testing has proven that FM 73 adhesive meets stringent environmental resistance and bonding durability requirements. To achieve maximum environmental resistance and bonding durability the use of BR® 127 corrosion inhibiting primer is recommended in bonding metallic components.

FEATURES & BENEFITS

- Demonstrates excellent peel strength and structural performance from -67°F to 180°F (-55°C to 82°C)
- Resistant to pre-bond humidity exposure
- Good moisture and corrosion resistance in high humidity
- Shop life of 15 days at 75°F (24°C)

SUGGESTED APPLICATIONS

- Metal-to-metal bonding
- Composite-to-composite bonding
- Composite-to-metal bonding

AEAD-00019
REV: 01
11 AUGUST 2011

CHARACTERISTICS

General Information

FM 73 adhesive is manufactured as a supported film with either knit or mat carrier, or as an unsupported film. FM 73 adhesive supported with a knit carrier offers optimum mechanical performance while the random mat version, FM 73 M adhesive, provides superior handling characteristics. FM 73 M adhesive can be supplied in a one-side tacky (OST) version which allows bonding of large metal parts without concerns of trapping air during lay-up. In addition, FM 73M OST adhesive film can be manufactured in widths up to 72 inches (183 cm) to accommodate large part fabrication.

A shop life in excess of 30 days at conditions of 75°F (24°C) or below allows the user a great deal of freedom in material handling and inventory control.

Table 1 I Product description

Product Number	Nominal Weight, lb/ft^2 (g/m^2) [1]	Nominal Thickness, inches (mm)	Color	Carrier
FM 73 film adhesive	0.045 (210) 0.060 (300) 0.085 (420)	0.007 (0.18) 0.010 (0.25) 0.015 (0.38)	Yellow Yellow Yellow	Polyester knit, both sides tacky
FM 73M film adhesive	0.030 (150) 0.045 (210) 0.060 (300) 0.085 (420)	0.005 (0.13) 0.007 (0.18) 0.010 (0.25) 0.015 (0.38)	Dark Green Yellow Yellow Yellow	Polyester mat, both sides tacky
FM 73M OST film adhesive	0.030 (150) 0.060 (300) 0.085 (420)	0.005 (0.13) 0.010 (0.25) 0.015 (0.38)	Dark Green Yellow Yellow	Polyester mat, one side tacky
FM 73U film adhesive	0.020 (100) 0.030 (150)	0.0035 (0.09) 0.005 (0.13)	Green Yellow	Unsupported

[1] Weight tolerance equals nominal weight ± 0.005 lb/ft^2 (± 25 g/m^2)

Table 2 I Handling properties

Volatiles	1.25% maximum
Outgassing properties (after complete cure)	0.78% TWL and 0.00% CVCM (NASA Reference Publication 1124, Rev. 8/87)
Recommended storage	Store at or below 0°F (-18°C)
Shelf life	12 months from date of shipment at recommended storage conditions
Shop life	15 days at or below 75°F (24°C)

Table 3 I Product description: BR 127 corrosion inhibiting primer

Color	Yellow
Solids	10% ± 1% sprayable
Density	7.3 lb/gal (875 g/liter)
Shop life	10 days at 90°F (32°C)
Shelf life	12 months from date of shipment at recommended storage conditions
Recommended storage	Store at or below 0°F (-18°C)

The following products are recommended for use with FM 73 film adhesive:

- BR® 127 corrosion inhibiting primer
- FM® 410 -1 and FM® 490A core splice foam adhesives for honeycomb splicing and bonding to spars
- CYCOM® 919 advanced composites
- CYCOM® 950 advanced composites

PROPERTIES

Table 4 I Mechanical Performance: Metal-to-Metal[1]

Property and Test Condition[2]	FM 73M 0.03 lb/ft² (150 g/m²)	FM 73M OST 0.03 lb/ft² (150 g/m²)	FM 73M 0.06 lb/ft² (300 g/m²)
Tensile shear, psi (MPa)			
-67°F (-55°C)	5890 (40.6)	6130 (42.3)	6340 (43.7)
75°F (24°C)	5770 (39.8)	6200 (42.8)	6680 (46.1)
180°F (82°C)	4050 (27.9)	3760 (25.9)	4400 (30.4)
Blister detection, psi (MPa)			
-67°F (-55°C)	5290 (36.5)	5100 (35.2)	5210 (36.0)
75°F (24°C)	4860 (33.5)	4700 (32.4)	4890 (33.7)
180°F (82°C)	3650 (25.2)	3580 (24.7)	3760 (25.9)
Climbing drum metal-to-metal peel, in-lb/in (Nm/m)			
-67°F (-55°C)	55 (220)	61 (270)	68 (300)
75°F (24°C)	66 (290)	73 (330)	87 (390)
180°F (82°C)	85 (380)	91 (410)	130 (570)
ASTM D-1781-76			
Floating roller peel, lb/in (KN/m)			
-67°F (-55°C)	56 (9.8)	51 (8.9)	44 (7.7)
75°F (24°C)	64 (11.2)	63 (11.0)	73 (12.8)
180°F (82°C)	55 (9.6)	49 (8.6)	76 (13.3)
ASTM-D-3167-76			

[1] Typical average results with BR 127 primer and recommended cure cycle:

- 30 minutes to 250°F (120°C)
- 60 minutes at 250 ± 5°F (120 ± 3°C) under 40 ± 5 psi (0.28 ± 0.03 MPa) pressure
- FPL etch was used for cleaning aluminum skins prior to bonding

[2] Materials:

- Tensile shear: 0.063 in. (1.60 mm) 2024-T3 clad
- Blister detection: 0.064 in (1.63 mm) 2024-T3 bare
- Climbing drum peel: 0.020 in to 0.040 in (0.51 mm to 1.03 mm) 2024-T3 clad
- Floating roller peel: 0.025 in to 0.063 in (0.64 mm to 1.60 mm) 2024-T3 bare

Table 5 I Mechanical Performance: Metal-to-Metal (continued)[1]

Property and Test Condition[2]	FM 73M OST 0.06 lb/ft² (300 g/m²)	FM 73 0.06 lb/ft² (300 g/m²)	FM 73 0.085 lb/ft² (425 g/m²)
Tensile shear, psi (MPa)			
-67°F (-55°C)	6680 (46.1)	6650 (45.9)	6770 (46.7)
75°F (24°C)	6580 (45.4)	6500 (44.9)	6840 (47.2)
180°F (82°C)	4540 (31.3)	4340 (30.0)	4770 (32.9)
Blister detection, psi (MPa)			
-67°F (-55°C)	5420 (37.4)	5460 (37.7)	5290 (36.5)
75°F (24°C)	4900 (33.8)	5100 (35.2)	5050 (34.8)
180°F (82°C)	4350 (30.0)	4080 (28.2)	4120 (28.4)
Climbing drum metal-to-metal peel, in-lb/in (Nm/m)			
-67°F (-55°C)	65 (290)	73 (330)	88 (390)
75°F (24°C)	83 (370)	95 (420)	150 (650)
180°F (82°C)	130 (580)	130 (560)	160 (690)
ASTM D-1781-76			
Floating roller peel, lb/in (KN/m)			
-67°F (-55°C)	58 (10.2)	66 (11.6)	52 (9.1)
75°F (24°C)	65 (11.4)	65 (11.4)	79 (13.8)
180°F (82°C)	95 (16.6)	96 (16.9)	110 (20.0)
ASTM-D-3167-76			

[1]Typical average results with BR 127 primer and recommended cure cycle:

- 30 minutes to 250°F (120°C)
- 60 minutes at 250 ± 5°F (120 ± 3°C) under 40 ± 5 psi (0.28 ± 0.03 MPa) pressure
- FPL etch was used for cleaning aluminum skins prior to bonding

[2]Materials:

- Tensile shear: 0.063 in. (1.60 mm) 2024-T3 clad
- Blister detection: 0.064 in (1.63 mm) 2024-T3 bare
- Climbing drum peel: 0.020 in to 0.040 in (0.51 mm to 1.03 mm) 2024-T3 clad
- Floating roller peel: 0.025 in to 0.063 in (0.64 mm to 1.60 mm) 2024-T3 bare

Table 6 I Mechanical Performance: Metallic Structural Sandwich[1]

Property and Test Condition[2]	FM 73M 0.06 lb/ft² (300 g/m²)	FM 73M OST 0.06 lb/ft² (300 g/m²)	FM 73 0.06 lb/ft² (300 g/m²)
Sandwich peel, in-lb/3 in (Nm/m)			
-67°F (-55°C)	50 (74)	46 (68)	53 (79)
75°F (24°C)	86 (130)	83 (120)	95 (140)
180°F (82°C)	38 (56)	33 (49)	41 (61)
Flatwise tensile, psi (MPa)			
-67°F (-55°C)	1500 (10.4)	1450 (10.0)	1680 (11.6)
75°F (24°C)	1050 (7.3)	1080 (7.4)	1300 (8.9)
180°F (82°C)	720 (5.4)	660 (4.6)	660 (4.6)

Table 7 I Mechanical Performance: Metallic Structural Sandwich (continued)[1]

Property and Test Condition[2]	FM 73M 0.085 lb/ft² (425 g/m²)	FM 73M OST 0.85 lb/ft² (425 g/m²)	FM 73 0.085 lb/ft² (425 g/m²)
Sandwich peel, in-lb/3 in (Nm/m)			
-67°F (-55°C)	70 (100)	75 (110)	87 (130)
75°F (24°C)	120 (180)	128 (190)	145 (220)
180°F (82°C)	40 (59)	55 (82)	65 (96)
Flatwise tensile, psi (MPa)			
-67°F (-55°C)	1580 (10.9)	1680 (11.6)	1730 (11.9)
75°F (24°C)	1450 (10.0)	1400 (9.7)	1400 (9.7)
180°F (82°C)	830 (5.7)	780 (5.5)	880 (6.0)

[1]Typical average results with BR 127 primer and recommended cure cycle:

- 30 minutes to 250°F (120°C)
- 60 minutes at 250 ± 5°F (120 ± 3°C) under 40 ± 5 psi (0.28 ± 0.03 MPa) pressure
- FPL etch was used for cleaning aluminum skins prior to bonding

[2]Materials:

- Skins: 0.020 in (0.5mm) 2024-T3 clad
- Core: 0.25 in (6.35 mm) 0.004 NP 5052

Table 8 I Mechanical Performance after Environmental Exposure[1]

Property and Test Condition	FM 73M 0.03 lb/ft² (150 g/m²)	FM 73M 0.06 lb/ft² (300 g/m²)	FM 73 0.06 lb/ft² (300 g/m²)
Tensile shear, psi (MPa) after:			
30 days at 120°F (50°C) and 95 – 100% R.H.	4960 (34.2)	4990 (34.4)	5140 (35.5)
30 days salt spray	4790 (33.1)	4930 (33.9)	5240 (36.1)
7 days immersion in JP-4 fuel (MIL-J-5624)	4780 (33.0)	4980 (34.4)	5270 (36.3)
7 days immersion in hydrocarbon fluid (TT-S-735)	4880 (33.6)	5040 (34.8)	5230 (36.1)
7 days in Skydrol 500*	4770 (32.9)	5060 (34.9)	5140 (35.5)

[1] Fluid exposure coupons are individual blister detection coupons with cut edges exposed and tested at 75 ± 5°F (24 ± 3°C)

* Product of Solutia Inc.

Table 9 I KGR-1 Stress Strain Data for FM 73M Adhesive Film, 0.06 lb/ft² (300 g/m²) with BR 127 Corrosion Inhibiting Primer with no Prebond or Postbond Exposure

[*f* = Shear Stress, psi (MPa), Σ = Shear Strain, in/in, G = Shear Modulus, psi (Mpa)]

Test Temperature	Linear Limit (LL)			Knee (KN)		Ultimate Failure (UL)	
	F	Σ	G	*f*	Σ	*f*	Σ
-67°F (-55°C)	3350 (23.1)	0.026	131,000 (904)	7220 (49.8)	0.097	8080 (55.7)	0.447
75°F (24°C)	2510 (17.3)	0.021	122,000 (842)	4690 (32.4)	0.062	5930 (40.9)	0.873
140°F (60°C)	1460 (10.1)	0.022	65,900 (455)	2620 (18.1)	0.073	5060 (34.9)	1.430
180°F (82°C)	980 (6.8)	0.028	37,800 (261)	1600 (11.0)	0.064	5150 (35.5)	1.623

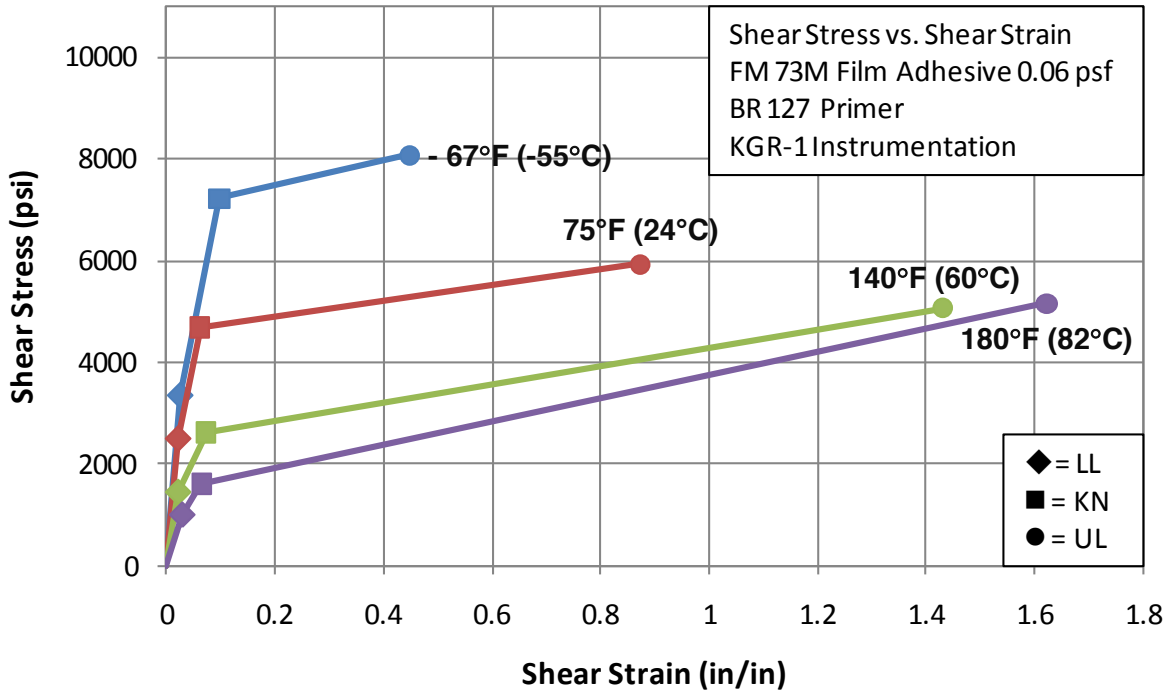

Table 10 I KGR-1 Stress Strain Data for FM 73M Adhesive Film, 0.06 lb/ft^2 (300 g/m^2) with BR 127 Corrosion Inhibiting Primer with Postbond Exposure of 100% R.H. at 140°F (60°C) until Saturated
[f = Shear Stress, psi (MPa), Σ = Shear Strain, in/in, G = Shear Modulus, psi (Mpa)]

Test Temperature	Linear Limit (LL)			Knee (KN)		Ultimate Failure (UL)	
	f	Σ	G	f	Σ	f	Σ
-67°F (-55°C)	3440 (23.7)	0.028	123,000 (849)	8070 (55.7)	0.100	8700 (60.0)	0.315
75°F (24°C)	2100 (14.5)	0.022	95,000 (655)	4200 (29.0)	0.081	5210 (35.9)	0.970
140°F (60°C)	1290 (8.9)	0.026	53,200 (368)	-	-	4210 (29.0)	1.420
180°F (82°C)	-	-	-	-	-	3540 (24.4)	1.620
215°F (102°C)	-	-	-	-	-	910 (6.3)	0.930

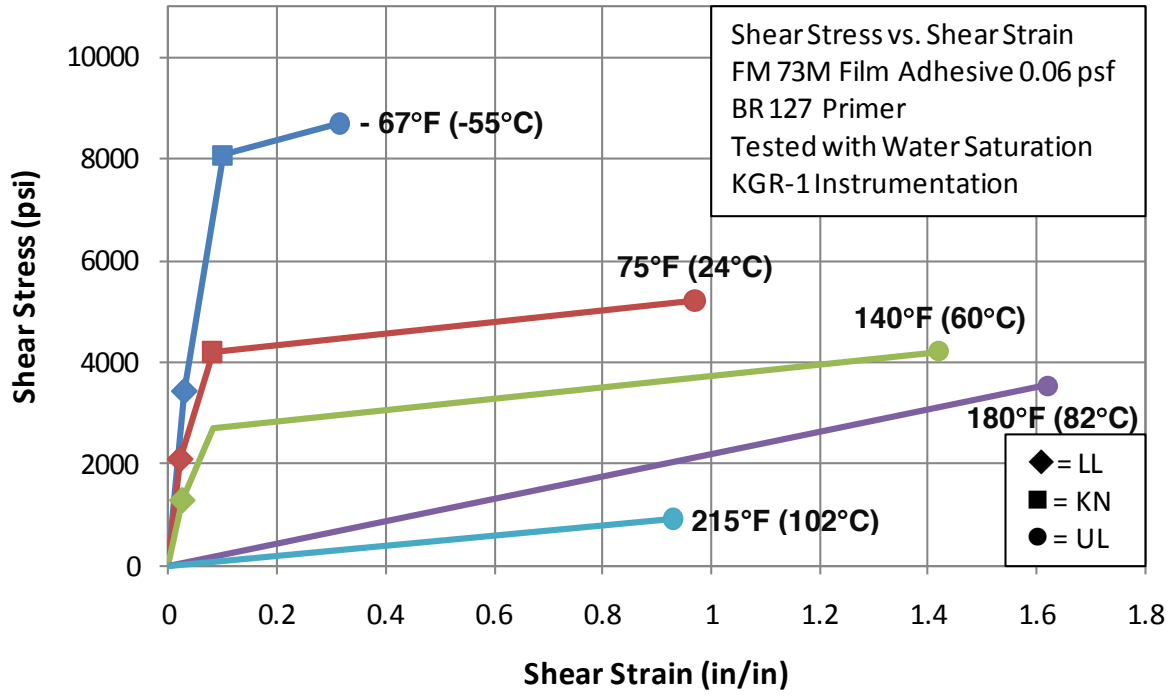

APPLICATION NOTES

Preparation of Aluminum

A clean, dry, grease-free surface is required for optimum performance. A recommended procedure for cleaning aluminum skins prior to priming or bonding is the FPL cleaning method:

1. Vapor degrease, alkaline clean, rinse and check for water break
2. Prepare a sodium dichromate/sulfuric acid solution as follows:
    a. Mix the following ingredients:

Sodium Dichromate	34 grams	FED-O-S-595A
Water	700 ml	Deionized water recommended
Sulfuric Acid	304 grams	FED-O-A-115, Class A, Grade 2

    b. Add additional water to make one liter

    This solution will dissolve 1.5 grams of 2024 clad aluminum per liter.

    NOTE: Chromic acid is highly corrosive. All contact with skin and tissues must be prevented. Wear impervious apron, boots and gloves as well as splash-proof goggles and face shield when preparing and/or using chromic acid. If airborne concentration of chromic acid exceeds the 8-hr TWA established by OSHA, respirators approved by NIOSH must be worn.

    Chromic acid solutions should be prepared and handled only in fume hoods or other adequately ventilated areas even when the TWA is not exceeded. Traces of chromyl chloride may occur in the vapors above heated chromic acid solutions prepared from chlorinated water.
3. Immerse aluminum part in sodium dichromate/sulfuric acid solution at 155 ± 5°F (68 ± 3°C) for 10 minutes (clad aluminum) or 5 minutes (bare aluminum)
4. Spray rinse with water at or below 75°F (24°C)
5. Immerse in cold water
6. Repeat spray rinse checking for water break
7. Dry in a vented oven below 150°F (65°C)

In addition to the FPL etch cleaning method for aluminum, the phosphoric acid anodizing (PAA) surface treatment[1] is now being used by a large number of aircraft manufacturers due to the improved surface bond durability provided by the PAA treatment.

Primer Application

Although not mandatory, BR 127 corrosion inhibiting primer is recommended for use with FM 73 film adhesive in bonding of aluminum details. BR 127 primer offers superior durability and resistance to hostile environments within the bond line and also may be used as a protective coating outside the bonded areas. Apply BR 127 as follows:

1. Allow BR 127 material to warm to room temperature prior to opening container
2. Thoroughly mix before application and agitate during application
3. Spary or brush coat to a dry primer thickness of 0.0001 inch (0.0025 mm) nominal with a 0.0002 inch (0.0050 mm) maximum thickness. For protective coating applications increase primer thickness to 0.0004 to 0.0010 inch (0.0102 to 0.025 mm).
4. Air dry 30 minutes minimum prior to using
5. Oven cure 30 minutes at 250 ± 10°F (120 ± 6°C)

[1] Boeing patent 4,085,012; April 18, 1978

Bonding Procedure

Primer assemblies which have been dried and wrapped with a protective covering such as Kraft paper may be stored at 75°F (24°C) for six months and longer without fear of degradation of the final bond.

Before bonding, detail parts and adhesive film must be properly assembled. Patterns of FM 73 film adhesive should be cut as required before removal of the protective covering which is easily stripped form the film at room temperature. Apply the film adhesive smoothly to the parts. For addition tack, warm to approximately 110 °F (43°C) with a heat gun or tack table.

After assembly of the details, apply pressure and cure using the standard cure cycle below:

1. Apply pressure at 40 ± 5 psi (0.28 ± 0.03 MPa)
2. Heat up to 250°F (120°C) in 30 minutes
3. Hold at 250 ± 5°F (120 ± 3°C) for 60 minutes

PRODUCT HANDLING AND SAFETY

Cytec Engineered Materials recommends wearing clean, impervious gloves when working with epoxy resin systems to reduce skin contact and to avoid contamination of the product.

Materials Safety Data Sheets (MSDS) and product labels are available upon request and can be obtained from any Cytec Engineered Materials Office.

DISPOSAL OF SCRAP MATERIAL

Disposal of scrap material should be in accordance with local, state, and federal regulations.

CONTACT INFORMATION

GLOBAL HEADQUARTERS
Tempe, Arizona
tel 480.730.2000
fax 480.730.2088

NORTH AMERICA

Olean, New York
tel 716.372.9650
fax 716.372.1594

Springfield, Massachusetts
tel 1.800.253.4078
fax 716.372.1594

Havre de Grace, Maryland
tel 410.939.1910
fax 410.939.8100

Winona, Minnesota
tel 507.454.3611
fax 507.452.8195

Anaheim, California
tel 714.630.9400
fax 714.666.4345

Orange, California
tel 714.639.2050
fax 714.532.4096

Greenville, Texas
tel 903.457.8500
fax 903.457.8598

Cytec Carbon Fibers LLC
Piedmont, South Carolina
tel 864.277.5720
fax 864.299.9373

D Aircraft Products, Inc.
Anaheim, California
tel 714.632.8444
fax 714.632.7164

EUROPE AND ASIA

Wrexham, United Kingdom
tel +44.1978.665200
fax +44.1978.665222

Östringen, Germany
tel +49.7253.934111
fax +49.7253.934102

Shanghai, China
tel +86.21.5746.8018
fax +86.21.5746.8038

CYTEC

TECHNICAL DATA SHEET AEROSPACE MATERIALS

FM® 300 Epoxy Film Adhesive

DESCRIPTION

FM® 300 is a modified epoxy film adhesive available with three different moisture-resistant polyester carriers. It is designed for bonding metal-to-metal and sandwich composite structures. To achieve ultimate environmental resistance in bonding aluminum details, use pre-cured BR® 127 primer with FM 300 film adhesive.

Extensively used as a surface finished ply on composites material outside layers, FM 300 film adhesive has unique properties which drastically reduce, and in some cases virtually eliminate, time-consuming sanding and filling operations.

FM 300 film adhesive has high elongation and toughness with high ultimate shear strength. This makes it particularly suitable for redistributing the high shear stress concentrations of graphite epoxy- to-metal bonds, and allows it to accommodate the low interlaminar shear strength of the composite. It is particularly good in fatigue resistance in these joints. In properly designed and processed joints, the tight-knit tricot carrier provides a degree of electrical isolation between metal and graphite composites to reduce galvanic corrosion.

FEATURES & BENEFITS

- Superior metal-to-metal peel strength, composite-to-composite bonding and composite-to-metal joints
- Extensively used as surfacing ply for composite materials
- Service temperature from -67°F to 300°F (-55°C to 150°C)
- Excellent moisture and corrosion resistance in high humidity environments with no significant reduction in mechanical properties
- Allows x-ray inspection of assemblies due to natural opacity of adhesive formulations
- Available in a wide range of film thicknesses tailored to specific applications
- Industry wide acceptance

SUGGESTED APPLICATIONS

- Metal-to-metal bonding
- Composite-to-composite bonding
- Composite-to-metal bonding
- Composite surfacing

 • AEAD-00002 • Rev. 02 • 9 October 2013

CHARACTERISTICS

Table 1 | Product Description for FM 300 Adhesive Films

Product Number	Weight, psf (gsm)[1]	Nominal Thickness, inches (mm)	Color	Carrier	Characteristics
FM 300 film adhesive	0.08 (390) 0.10 (490)	0.013 (0.32) 0.015 (0.38)	Blue Blue	Tight knit	Enhanced bondline thickness control. Good blend of structural and handling properties
FM 300K film adhesive	0.05 (244) 0.08 (390)	0.008 (0.20) 0.013 (0.32)	Green Green	Wide open knit	Highest overall performance
FM 300M film adhesive	0.03 (150) 0.08 (390)	0.005 (0.13) 0.013 (032)	Green Green	Random mat	Provides the best bondline and flow control. Reduces tendency to trap air during lay-up.
FM 300U film adhesive	0.03 (150) 0.055 (268)	0.005 (0.13) 0.008 (0.20)	Green Green	Unsupported film	Can be reticulated

[1] Weight tolerance equals nominal weight ± 0.005 psf (± 25 gsm)

Table 2 | Handling Properties of FM 300 Adhesive Films

Properties	Description
Volatiles	1.0% maximum
Outgassing properties (after complete cure)	0.92% TWL and 0.07% CVCM (NASA reference publication 1124, Rev. 8/87)
Recommended storage	Supported grades: store at or below 0°F (-18°C) Unsupported grades: store at 40°F (4.5°C)
Shelf life	Supported Grades: 12 months from date of shipment Unsupported Grades: 4 months from date of shipment
Shop life	10 days at 90°F (32°C) 30 days at 70°F (21°C)

Table 3 | Product Description: BR® 127 corrosion inhibiting primer

Properties	Description
Color	Yellow
Solids	10% ± 1% sprayable
Density	7.3 lbs/gal (875 g/liter)
Shop life	5 days at 90°F (32°C)
Shelf life	12 months from date of shipment at recommended storage
Recommended	Store at or below 0°F (-18°C)

PROPERTIES

Table 4 | Mechanical Properties[1]

Sample Description[2] Product Number	FM 300 0.08 psf (390 gsm)	FM 300K 0.05 psf (244 gsm)	FM 300K 0.08 psf (390 gsm)	FM 300M 0.03 psf (150 gsm)	FM300M 0.08 psf (390 gsm)
Tensile shear, psi (MPa)					
-67°F (-55°C)	5080 (35.0)	–	5460 (37.7)	–	4930 (34.0)
75°F (24°C)	5145 (35.5)	5340 (36.8)	5850 (40.3)	4325 (29.8)	5275 (36.4)
250°F (120°C)	3995 (27.6)	3575 (24.7)	4200 (28.9)	3360 (23.2)	4040 (27.9)
300°F (150°C)	2910 (20.0)	2965 (20.4)	3155 (21.8)	2310 (15.9)	2955 (20.4)
Floating roller peel, in-lb/in (kN/m)					
-67°F (-55°C)	28 (4.9)	–	28 (4.9)	–	29 (5.1)
75°F (24°C)	29 (5.1)	23 (40)	28 (4.9)	26 (4.6)	29 (5.1)
250°F (120°C)	–	–	–	–	–
300°F (150°C)	25 (4.4)	–	26 (4.6)	27 (4.7)	26 (4.6)
Honeycomb sandwich peel, in-lb/3 in (Nm/m)					
-67°F (-55°C)	–	25 (37)	40 (58)	–	–
75°F (24°C)	–	22 (32)	45 (66)	11 (16)	–
250°F (120°C)	–	–	–	–	–
300°F (150°C)	–	22 (32)	28 (41)	–	–
Flatwise tensile, psi (MPa)					
-67°F (-55°C)	1350 (9.3)	–	1075 (7.4)	–	1600 (11.0)
75°F (24°C)	1095 (7.6)	–	1030 (7.1)	435 (3.0)	1390 (9.6)
250°F (120°C)	–	–	–	–	–
300°F (150°C)	345 (2.4)	340 (2.3)	470 (3.2)	125 (0.86)	513 (3.5)

[1]FM 300, FM 300K and FM 300M film adhesives with BR 127 primer: Typical average results.
[2] Metal: Tensile shear 0.063 in. (1.63 mm) 2024-T3 clad, honeycomb skins 0.020 in. (0.51 mm) 2024-T3 clad, honeycomb 3/16 in. (4.76 mm) 0.002 (0.65 mm) NP5052, floating roller peel 0.025/0.063 2024-T3 clad

Table 5 | Humidity and Fluid Exposure[1]

Sample Description[2] Product Number	FM 300 0.08 psf (390 gsm)	FM 300K 0.08 psf (390 gsm)	FM 300M 0.08 psf (390 gsm)
Tensile shear, psi (MPa) after 30 days at 120°F (50°C), 95 – 100% RH[3]	5185 (35.8)	6225 (42.9)	5535 (38.2)
Tensile shear, psi (MPa) after 7 days immersion in:			
JP-4 fuel	5030 (34.7)	6240 (43.0)	5550 (38.3)
Anti-icing fluid	4915 (33.9)	6275 (43.3)	5250 (36.2)
Hydraulic oil	5100 (35.2)	6130 (42.3)	5350 (36.9)
Hydrocarbon fluid	5155 (35.6)	6095 (42.0)	5125 (35.3)
Tensile shear, psi (MPa) after 200 hours in Skydrol[4] hydraulic fluid at 150°F (66°C)	4935 (34.0)	6350 (43.8)	4860 (33.5)

[1] FM 300, FM 300K and FM 300M film adhesive with BR 127 primer: Typical average results
[2] Metal: Tensile shear 0.063 in. (1.63 mm) 2024-T clad
[3] Tested at 75°F (24°C)
[4] A product of Solutia, Inc.

Table 6 | Effect of Humidity Exposure on Film Prior to Bonding[5]

Property	Test Condition	Control (no exposure)	15 Day Exposure at 54% RH
Tensile shear, psi (MPa)	Tested at 75°F (24°C)	4800 (33.1)	4900 (33.8)
		4700 (32.4)	4800 (33.1)
		4650 (32.1)	5200 (35.9)
	Tested at 300°F (150°C)	3400 (23.5)	2600 (17.9)
		3300 (22.8)	2900 (20.0)
Floating roller peel, lbs/in (kN/m)	Tested at 75°F (24°C)	28 (4.9)	28 (4.9)
		29 (5.1)	29 (5.1)
Honeycomb sandwich peel, in-lb/3 in. (Nm/m)	Tested at 75°F (24°C)	75 (110)	75 (110)
		68 (100)	69 (100)

[5] Sample: FM 300K film adhesive, 0.08 psf (390 gsm) with BR 127 primer

Metal:
Tensile shear	0.063 in. (1.63 mm) 2024-T3 clad
Honeycomb skins	0.020 in (0.51 mm) 2024-T3 clad
Honeycomb	3/16 in. (4.76 mm) 0.002 (0.65 mm) NP 5052
Floating roller peel	0.025/0.063 2024-T3 clad

Cure cycle: 60 minutes to 350°F (175°C)
60 minutes at 350°F (175°C)
40 psi (0.28 MPa)

Table 7 | 300°F (150°C) Heat Aging Studies[1]

Hours exposure	Tensile shear psi (MPa) tested at 75°F (24°C)	Tensile shear psi (MPa) tested at 300°F (149°C)	Honeycomb sandwich peel in-lb/3 in (Nm/m) tested at 75°F (24°C)	Flatwise tensile, psi (MPa) tested at 75°F (24°C)
Control	6070 (41.8)	2980 (20.6)	64 (94)	1380 (9.5)
1440	4460 (30.8)	3720 (25.6)	35 (52)	–
2880	4700 (32.4)	3400 (23.5)	41 (60)	960 (6.6)
4320	4300 (29.7)	3430 (23.7)	26 (39)	1000 (6.9)
5040	3910 (27.0)	3530 (24.4)	23 (34)	990 (6.8)
5760	3210 (22.1)	3450 (23.8)	20 (30)	950 (6.6)
7200	3580 (24.7)	3450 (23.8)	20 (30)	–
7920	3270 (22.6)	2960 (20.4)	17 (25)	780 (5.4)

[1] Sample: FM 300K film adhesive, 0.08 psf (390 gsm) with BR 127 primer

Metal: Tensile shear 0.063 in. (1.63 mm) 2024-T3 clad
Honeycomb skins 0.020 in (0.51 mm) 2024-T3 clad
Honeycomb 3/16 in. (4.76 mm) 0.002 (0.65 mm) NP 5052

Cure cycle: 60 minutes to 350°F (175°C)
60 minutes at 350°F (175°C)
40 psi (0.28 MPa)

KGR Stress Strain Data

The heart of Cytec is new technology for structural adhesives is the KGR-1 extensometer. This instrument provides the basic, definitive property of a structural adhesive – its shear stiffness. KGR-1 records the entire stress strain curve for the adhesive in environments reproducible in the laboratory.

This technology benefits both the designer and the adhesive formulator. The designer and stress analyst use this technology to predict the service performance of the adhesive bond, including strength, creep and fatigue in environments reproducible in the laboratory.

Until Cytec developed the KGR-1, test methods to obtain shear stiffness were either inaccurate or too costly to allow sufficient data for statistical confidence. A measure of the difficulty in obtaining this stiffness is that movements of one quarter of a micron (0.00001 inches) must be detected with clarity and reliability. KGR-1 does this over a temperature range of -67°F (-55°C) to 500°F (260°C) in hostile environments reproducible in the laboratory.

The economy of operation of KGR-1 makes stiffness data affordable to the designer. This economy allows statistical confidence necessary for practical analysis. In addition to stiffness, KGR-1 provides the shear stress strain relationship over the entire non-linear range up to and including ultimate failure.

It is established that fatigue life and residual static strength are dependent on strain at ultimate stress. The larger the strain, the longer the fatigue life and the higher the residual static strength (the strength after the joint has seen the required fatigue loads). This data defines limits for creep and fatigue conditions. It is possible to perform proper stress analysis of bonded aircraft primary structure. Accurate predictions are now possible for the bond performance over the life of the aircraft.

Apart from its value to the designer, KGR-1 technology is invaluable to the formulator of structural adhesives. Stress strain properties beyond the linear range define the adhesive's performance in fatigue and toughness.

If you are interested in acquiring a KGR-1 exensometer for help in your own work, please contact a Cytec representative.

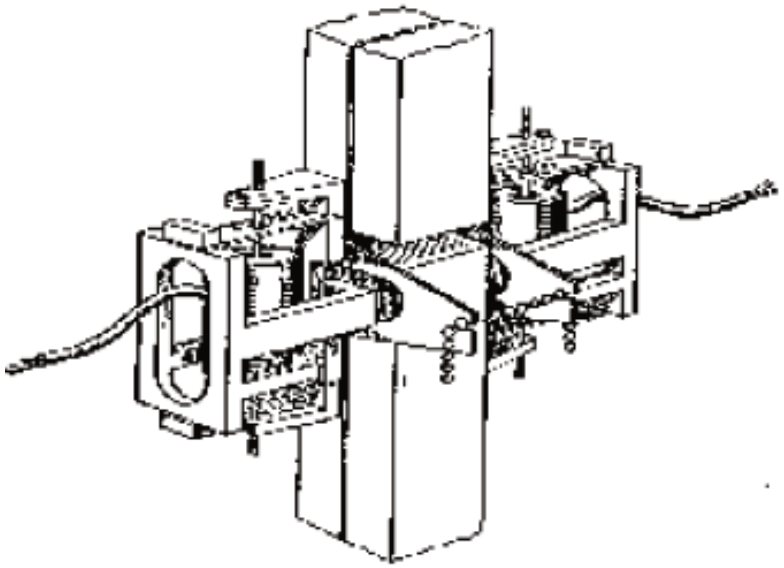

Table 6 | KGR-1 Stress Strain Data for FM 300K Adhesive Film, 0.06 psf (290 gsm) with BR® 127 Primer
[*f* = Shear Stress, psi (MPa), = Shear Strain, in/in, G = Shear Modulus, psi (Mpa)]

Test Temperature	Linear Limit (LL)			Knee (KN)		Ultimate Failure (UL)	
	f	Σ	G	*f*	Σ	*f*	Σ
75°F (24°C)	2060 (14.2)	0.0156	131,500 (907.5)	6100 (42.1)	0.0932	7210 (49.8)	0.5446
220°F (104°C)	916 (6.32)	0.0150	64,700 (446.2)	3000 (20.8)	0.0835	5190 (35.8)	1.2073
220°F (104°C)[1]	745 (5.14)	0.0273	27,500 (189.8)	1880 (13.0)	0.1047	3100 (21.4)	1.0744

[1] Postbond exposure to 100% RH at 140°F (60°C) until saturated

Figure 9 | Shear Stress vs. Shear Strain for FM 300K Film Adhesive in Various Environments KGR-1 Instrumentation

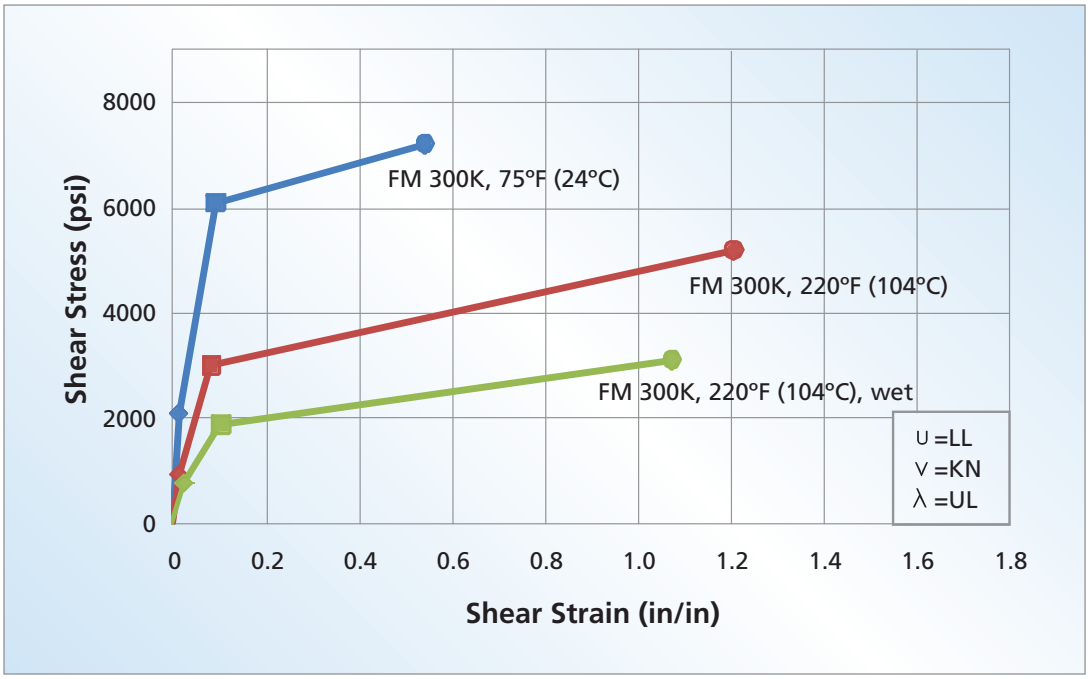

APPLICATION NOTES

Preparation of Aluminum

A clean, dry, grease-free surface is required for optimum performance. A recommended procedure for cleaning aluminum skins prior to priming or bonding is the FPL cleaning method:

1. Vapor degrease, alkaline clean, rinse and check for water break
2. Prepare a sodium dichromate/sulfuric acid solution as follows:
   a. Mix the following ingredients:

Sodium Dichromate	34 grams	FED-O-S-595A
Water	700 ml	Deionized water recommended
Sulfuric Acid	304 grams	FED-O-A-115, Class A, Grade 2

   b. Add additional water to make one liter

   This solution will dissolve 1.5 grams of 2024 clad aluminum per liter.

   NOTE: Chromic acid is highly corrosive. All contact with skin and tissues must be prevented. Wear impervious apron, boots and gloves as well as splash-proof goggles and face shield when preparing and/or using chromic acid. If airborne concentration of chromic acid exceeds the 8-hr TWA established by OSHA, respirators approved by NIOSH must be worn.

   Chromic acid solutions should be prepared and handled only in fume hoods or other adequately ventilated areas even when the TWA is not exceeded. Traces of chromyl chloride may occur in the vapors above heated chromic acid solutions prepared from chlorinated water.
3. Immerse aluminum part in sodium dichromate/sulfuric acid solution at 155 ± 5°F (68 ± 3°C) for 10 minutes (clad aluminum) or 5 minutes (bare aluminum)
4. Spray rinse with water at or below 75°F (24°C)
5. Immerse in cold water
6. Repeat spray rinse checking for water break
7. Dry in a vented oven below 150°F (65°C)

In addition to the FPL etch cleaning method for aluminum, the phosphoric acid anodizing (PAA) surface treatment1 is now being used by a large number of aircraft manufacturers due to the improved surface bond durability provided by the PAA treatment.

Primer Application

Although not mandatory, BR 127 corrosion inhibiting primer is recommended for use with FM 300 adhesive in the bonding of aluminum details. BR 127 primer offers superior durability and resistance to hostile environments within the bond line and also may be used as a protective coating outside the bonded areas. Apply BR 127 as follows:

1. Allow BR 127 material to warm to room temperature prior to opening container
2. Thoroughly mix before application and agitate during application
3. Spray or brush coat to a dry primer thickness of 0.0001 inch (0.0025 mm) nominal with a 0.0002 inch (0.0050 mm) maximum thickness
4. Air dry 30 minutes minimum prior to using
5. Oven dry 30 minutes at 250 ± 10°F (120 ± 6°C)

[1] Boeing patent 4,085,012; April 18, 1978

Bonding Procedure

Bond FM 300 film adhesive at pressures ranging from 15 – 100 psi (0.10 – 0.69 MPa) depending upon the application. For press, autoclave, pressure diaphragm or vacuum bag curing use the following cure cycle:

1. Heat up to 350°F (175°C) in 30 – 60 minutes
2. Hold at 350°F (175°C) for 60 minutes

Compatibility

The cure temperature, pressure and gel time of FM 300 film adhesive make it compatible for co-cure or simultaneous autoclave runs with FM® 61 and FM® 96 film adhesives as well as BR 127 primer.

PRODUCT HANDLING AND SAFETY

Cytec Industries recommends wearing clean, impervious gloves when working with epoxy resin systems to reduce skin contact and to avoid contamination of the product. Materials Safety Data Sheets (MSDS) and product labels are available upon request and can be obtained from any Cytec location supplying aerospace materials.

DISPOSAL OF SCRAP MATERIAL

Disposal of scrap material should be in accordance with local, state, and federal regulations.

CONTACT INFORMATION

GLOBAL HEADQUARTERS for AEROSPACE MATERIALS

Tempe, Arizona
tel 480.730.2000
fax 480.730.2088
email custinfo@cytec.com

NORTH AMERICA

Anaheim, California
tel 714.630.9400
fax 714.666.4345

Orange, California
tel 714.639.2050
fax 714.532.4096

Greenville, Texas
tel 903.457.8500
fax 903.457.8598

Winona, Minnesota
tel 507.454.3611
fax 507.452.8195

Havre de Grace, Maryland
tel 410.939.1910
fax 410.939.8100

D' Aircraft Anaheim, California
tel 714.632.8444
fax 714.632.7164

Cytec Carbon Fiber
Piedmont, South Carolina
tel 864.277.5720
fax 864.299.9373

EUROPE

Wrexham, United Kingdom
tel +44 1978.665200
fax +44 1978.665222

Östringen, Germany
tel +49 7253.934111
fax +49 7253.934102

ASIA

Shanghai, China
tel +86 21.5746.8018
fax +86 21.5746.8038

14002-D

Standard Modulus Unidirectional Prepreg

Product Description

Rock West Composites PROPreg™ is a heat activated carbon fiber + epoxy system recommended especially for fiber-reinforced composite parts. This prepreg exhibits excellent mechanical strength and stiffness properties.

Handling, Safety and Storage

- Gloves and safety glasses are recommended for user's personal protection.
- When removing from freezer keep sealed until fully thawed.

Material Specification (Composite)

Physical Properties	
Fiber	T700 SC-12K
Resin	250F Epoxy
Shelf Life (°C/°F)	6+ months (@ ≤-18°C / 0°F) 1 month (@ 20°C / 68°F)
Gel Time @ 135°C / 270°F	3 – 6 minutes
Tg Glass Transition (°C / °F)	130 ± 10 °C / 266 ± 18 °F

Typical Composite Mechanical Properties (0° orientation) @ 23 °C		
Tensile Strength (MPa)	2250	ASTM D 3039
Tensile Modulus (GPa)	127	
Comp. Strength (MPa)	1247	ASTM D 3410
Comp. Modulus (GPa)	123	
Flexural Strength (MPa)	1500	ASTM D 790
Flexural Modulus (GPa)	98	

Processing

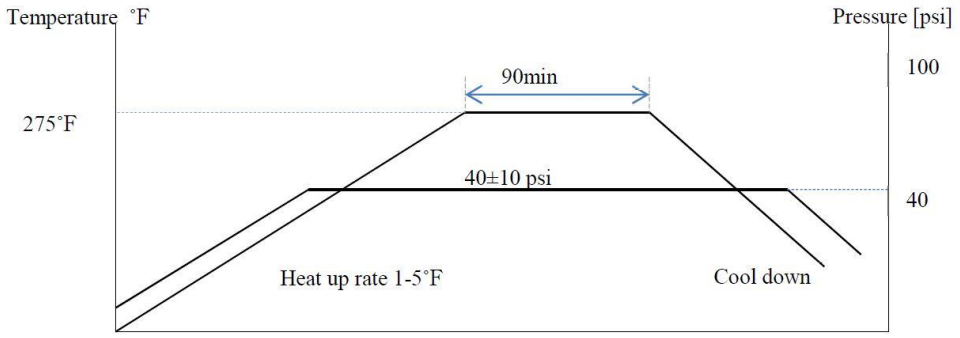

- Pressure required for adequate consolidation
- Heat up (ramp) rate is listed as an acceptable range, in degrees F per minute
- Laminates cure for 90 min. @ 275 °F or longer at lower temperatures

Manufacturing: 3392 West 8600 South, West Jordan, UT 84088 | Corporate: 1602 Precision Park Lane, San Diego, CA 92173
Ph: 801.566.3402 | Fx: 855.301.9874 | www.rockwestcomposites.com

TECHNICAL DATASHEET
No. CFA005

TORAYCA®

T700S DATA SHEET

Highest strength, standard modulus fiber available with excellent processing characteristics for filament winding and prepreg. This never twisted fiber is used in high tensile applications like pressure vessels, recreational, and industrial.

FIBER PROPERTIES

		English	Metric	Test Method
Tensile Strength		711 ksi	4,900 MPa	TY-030B-01
Tensile Modulus		33.4 Msi	230 GPa	TY-030B-01
Strain		2.1 %	2.1 %	TY-030B-01
Density		0.065 lbs/in^3	1.80 g/cm^3	TY-030B-02
Filament Diameter		2.8E-04 in.	7 μm	
Yield	6K	3,724 ft/lbs	400 g/1000m	TY-030B-03
	12K	1,862 ft/lbs	800 g/1000m	TY-030B-03
	24K	903 ft/lbs	1,650 g/1000m	TY-030B-03
Sizing Type & Amount	50C	1.0 %		TY-030B-05
	60E	0.3 %		TY-030B-05
	F0E	0.7 %		TY-030B-05
	Twist	Never twisted		

FUNCTIONAL PROPERTIES

CTE	-0.38	$\alpha \cdot 10^{-6}$/°C
Specific Heat	0.18	Cal/g·°C
Thermal Conductivity	0.0224	Cal/cm·s·°C
Electric Resistivity	1.6 x 10^{-3}	Ω·cm
Chemical Composition: Carbon	93	%
Na + K	<50	ppm

COMPOSITE PROPERTIES *

Tensile Strength	370 ksi	2,550 MPa	ASTM D-3039
Tensile Modulus	20.0 Msi	135 GPa	ASTM D-3039
Tensile Strain	1.7 %	1.7 %	ASTM D-3039
Compressive Strength	215 ksi	1,470 MPa	ASTM D-695
Flexural Strength	245 ksi	1,670 MPa	ASTM D-790
Flexural Modulus	17.5 Msi	120 GPa	ASTM D-790
ILSS	13 ksi	9 kgf/mm^2	ASTM D-2344
90° Tensile Strength	10.0 ksi	69 MPa	ASTM D-3039

* Toray 250°F Epoxy Resin. Normalized to 60% fiber volume.

T700S

COMPOSITE PROPERTIES**

Tensile Strength	355 ksi	2,450 MPa	ASTM D-3039
Tensile Modulus	18.0 Msi	125 GPa	ASTM D-3039
Tensile Strain	1.7 %	1.7 %	ASTM D-3039
Compressive Strength	230 ksi	1,570 MPa	ASTM D-695
Compressive Modulus	--- Msi	--- GPa	ASTM D-695
In-Plane Shear Strength	14 ksi	98 MPa	ASTM D-3518
ILSS	15.5 ksi	11 kgf/mm^2	ASTM D-2344
90˚ Tensile Strength	10.0 ksi	70 MPa	ASTM D-3039

** Toray Semi-Toughened 350˚F Epoxy Resin. Normalized to 60% fiber volume.

See Section 4 for Safety & Handling information. The above properties do not constitute any warranty or guarantee of values. These values are for material selection purposes only. For applications requiring guaranteed values, contact our sales and technical team to establish a material specification document.

PACKAGING

The table below summarizes the tow sizes, twists, sizing types, and packaging available for standard material. Other bobbin sizes may be available on a limited basis.

Tow Sizes	Twist[1]	Sizing	Bobbin Net Weight (kg)	Bobbin Type[2]	Bobbin Size (mm) a	b	c	d	e	Spools per Case	Case Net Weight (kg)
6K	C	50C	2.0	III	76.5	82.5	280	140	252	12	24
12K	C	50C	6.0	III	76.5	82.5	280	200	252	4	24
	C	60E	6.0	III	76.5	82.5	280	200	252	4	24
	C	F0E	6.0	III	76.5	82.5	280	200	252	4	24
24K	C	50C	6.0	III	76.5	82.5	280	200	252	4	24
	C	60E	6.0	III	76.5	82.5	280	200	252	4	24
	C	F0E	6.0	III	76.5	82.5	280	200	252	4	24

1 **Twist** A: Twisted yarn B: Untwisted yarn made from a twisted yarn through an untwisting process C: Never twisted yarn

2 **Bobbin Type** See Diagram below

TYPE I

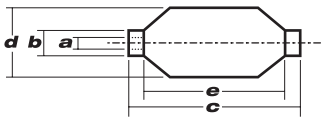

TYPE II

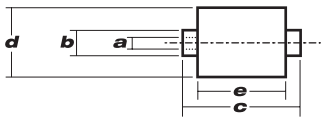

TYPE III

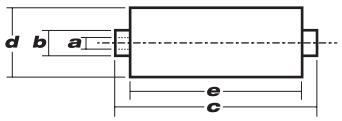

TORAY CARBON FIBERS AMERICA, INC.
6 Hutton Centre Drive, Suite #1270, Santa Ana, CA 92707 TEL: (714) 431-2320 FAX: (714) 424-0750
Sales@Toraycfa.com Technical@Toraycfa.com www.torayusa.com